AG-336

5. TRANSONIC WIND TUNNEL WALL INTERFERENCE

Authors N. Malmuth,
R. Crites
J. Everhart,
P. Newman
W. Sickles

PAGE

5. TRANSONIC WIND TUNNEL WALL INTERFERENCE

5.1 BACKGROUND

5.1.1 SCOPE AND OVERVIEW

Transonic wind tunnel corrections pose unique and difficult challenges. Because of their technical importance, they have been the subject of active research since World War II. The subject is vast; and adequate treatment demands a separate treatise such as an update of Goethert [71]. Although much progress has been made, significant effort is still needed to cope with current needs and issues, since large gaps remain in our knowledge. Because significant developments have occurred since the last AGARD review of this topic [67], an updated assessment is appropriate. Although not an exhaustive survey, this chapter is intended to provide a current glimpse of some activities in transonic wall interference. It contains different perspectives from Arnold Engineering Development Center (AEDC), McDonnell Douglas, NASA Langley and Rockwell Science Center. It makes no attempt to discuss the important area of experimental and instrumentation methods exemplified by the continuing challenges of making accurate static pressure measurements near ventilated walls, and non-invasive optical diagnostics for three-dimensional transonic wind tunnel flow mapping and visualisation. Rather, it emphasises the related topics of wall simulation and correction prediction procedures. These are especially difficult because of the nonlinearity of the flow as well as shock wave interactions with the walls and their consequences for extrapolation from ground tests to flight.

As compared to low and moderate supersonic speeds, the corrections can be large. Except for weak supercriticality (WS), which is defined by a high subsonic flow containing only small supersonic pockets, compressible corrections based on the imaging, and superposition methodology such as panel methods used extensively for low Mach number wind tunnel flows are not applicable since the flow is highly non-linear with shocks. In the wind tunnel, WS implies that the far upstream and downstream regions are subsonic, without non-linear mixed flow effects. WS frequently occurs over commercial transport aircraft at cruise conditions. Because of such practicality, some of this chapter relates to this situation. In the wind tunnel, WS is also associated with supersonic bubbles whose height is small compared to the wall height. When these two dimensions are comparable, and the freestream is slightly subsonic, the flow has been classified by Hornung and Stanewsky [85] as Group 1. Group 2 flows are also associated with subsonic freestreams but with free field sonic bubbles penetrating the walls. Sonic Mach number and choked flow are special subcases of Group 2 flows. Slightly supersonic freestreams are classified as Group 3. We will be concerned with all three groups in this chapter. Adaptive walls in which the wind tunnel walls or near-wall regions are configured to replicate free field conditions will be mentioned only in passing, as these are discussed in Chapter 10.

5.1.2 PREVIOUS LITERATURE AND CONFERENCES

Since Garner, *et al.* [67] as well as Pindzola and Lo [151], a number of conferences and summary papers dealing with wind tunnel wall interference have been published. Although much of this work was not exclusively for the transonic flow regime (see the subsonic material discussed in the previous chapters herein), many of the ideas and procedures are applicable to this speed range (albeit, frequently, with the restriction of weak supercriticality and subsonic far fields).

Several conference proceedings devoted to wall interference are:

a) Wall Interference in Wind Tunnels; AGARD [3]

b) Wind Tunnel Wall Interference Assessment/Correction—1983; Newman and Barnwell, editors [139]

c) Adaptive Wall Wind Tunnels and Wall Interference Correction Methods; Hornung and Stanewsky, editors [85]

d) International Conference on Adaptive Wall Wind Tunnel Research and Wall Interference Correction; He, editor [83]

e) Wall Interference, Support Interference, and Flow Field Measurements; AGARD [5]

In addition, since 1970, a number of other AGARD Symposia and AIAA Meetings related to wind tunnel and testing techniques, have included sessions devoted to wall interference. Noteworthy summary papers in addition to those appearing in the previously cited conference proceedings are:

a) Two-Dimensional Transonic Testing Methods; Elsenaar, editor [49]

b) Two-Dimensional Wind Tunnel Wall Interference; Mokry, *et al.* [133],

c) Wind Tunnel Wall Interference; Newman, *et al.* [138],

d) Advances at AEDC in Treating Transonic Wind Tunnel Wall Interference; Kraft, *et al.* [109],

e) Calculation of Transonic Wall Interference; Donegan, *et al.* [47],

f) Emerging Technology for Transonic Wind-Tunnel Wall Interference Assessment and Corrections; Newman, *et al.* [142],

g) Wall Interference Assessment and Corrections; Newman, *et al.* [143].

Lynch, *et al.* [117] and Ashill [12], which appear in AGARD [5], review and summarise recent wall interference correction status and needs. Adaptive wind tunnel wall technology and applications have been reviewed recently in AGARD [4]. Also, a bibliography of wall interference work in the 1980's by Tuttle and Cole [178] cites many papers.

5.1.3 WALL INTERFERENCE/REYNOLDS SIMULATION TRADE-OFF IN MODEL SIZING

Currently, the issue of US wind tunnel modernisation is being addressed. A major thrust is attainment of near-flight Reynolds numbers. If large models are used, wall and sting interference are limiting factors in obtaining a tunnel flow even qualitatively resembling that of flight. In particular, testing at transonic speeds can produce steep wave fronts that reflect back on the model. Ventilated walls, porous and slotted, were developed to cancel blockage and allow testing through the transonic range, while porous walls, specifically, have been developed with the aim of cancelling these reflections. In spite of the

advances made in this technology as well as computational simulations, much still needs to be done to understand the trade-offs in sizing wind tunnel models and test sections to minimise wall and sting effects while maximising model Reynolds numbers. Key factors in this balance are shock-boundary layer interactions, and coupling of separation with laminar-turbulent transition. These as well as other highly Reynolds number-dependent phenomena affect whether the wind tunnel and the free flight flow resemble each other.

An extreme example of trade-offs between wall interference and required physical flow simulation was posed by the special requirements of the NASA supercritical, laminar flow control (LFC), swept-wing experiment (Harris, *et al.* [82]) conducted in the 8-Ft Transonic Pressure Tunnel (8-Ft TPT) at the Langley Research Center. Specifically, a proper simulation of an unbounded supercritical-flow condition about an infinite-span yawed wing of large chord at low noise and turbulence levels was desired. A transonic test condition was needed in order to establish the compatibility of an active LFC wing-suction system with the current high-performance, supercritical-airfoil technology. The LFC experiment had to be done in a wind tunnel that had levels of stream turbulence and acoustic noise approaching those of flight conditions so that the suction required to maintain laminar flow on the model was realistic. Conventional slotted or porous-walled transonic tunnels were inadequate in this regard; however, installation of screens and honeycomb, as well as closing the slots and choking the flow at the downstream end of the test section significantly reduced pressure fluctuations in the test section. Since transport aircraft envisioned for LFC applications have moderately swept wings of high aspect ratio where crossflow instability is the dominant transition mechanism, this instability must be investigated at appropriate flight crossflow Reynolds numbers. This requirement, together with the physical-size limitations set by slot-duct construction in the test panel and the required limitations on roughness-height Reynolds number for laminar flow, resulted in a large-chord swept-wing panel. In the 8-ft TPT, both the resulting ratio of tunnel height to model chord and the wing-panel aspect ratio are somewhat less than unity.

The liner designed by Newman, *et al.* [141] and constructed for the LFC experiment is characterised by its contoured shape of nonporous materials which produces a specified flow at the fixed transonic design or test condition. To produce a transonic wind-tunnel flow that simulates free-air flow about an infinite-span yawed wing, all bounding test-section walls had to be contoured. This contouring extended well into the existing tunnel contraction and diffuser in order to establish the flow and minimise loss of tunnel performance. The sensitivity of high-speed channel flows to the effective cross-sectional area-ratio distribution required viscous boundary-layer displacement corrections be made. This example illustrates the complex trade-offs that are needed in a useful wind tunnel simulation that can attempt to replicate flight conditions.

5.1.4 CORRECTABILITY

If the essential physics of the free field flow can be closely approximated by the wind tunnel, and if the fluid-dynamic phenomena on and near both the aerodynamic model and the tunnel walls are properly captured and described by the mathematical formulation, the test data are defined to be **correctable.** Determining the correctability envelope remains elusive due to our limited knowledge (particularly in the transonic regime) of separation, turbulence, transition, shock wave phenomena and non-linear flow physics. Kemp [104] introduced the concept of a correctable-interference transonic wind tunnel combining a capability for wall-interference assessment with a limited capability for wall control. In that paper, he demonstrated the feasibility of using experimentally measured data directly as boundary values for the assessment in lieu of more generally formulated but less accurate wall boundary conditions. He

anticipated that such principles, used in non-linear flow codes, would lead to an accurate assessment of the wall interference for transonic tunnels.

Quoting from Kemp [104], "This capability alone [accurate assessment], however, will not produce the desired result of eliminating wall interference as an error source in transonic wind-tunnel testing. The concept of the self-correcting wind tunnel (Goodyer [73]; Sears [162]; and, Ferri and Baronti [59]) which would exercise iteratively some form of controllable walls and the associated control logic to satisfy an interference-free criterion has been proposed by others. The difficulties envisioned in implementing and operating the self-correcting wind tunnel are significant. An alternate approach to the minimisation of testing errors due to wall interference, designated as the correctable-interference transonic wind tunnel, is offered here."

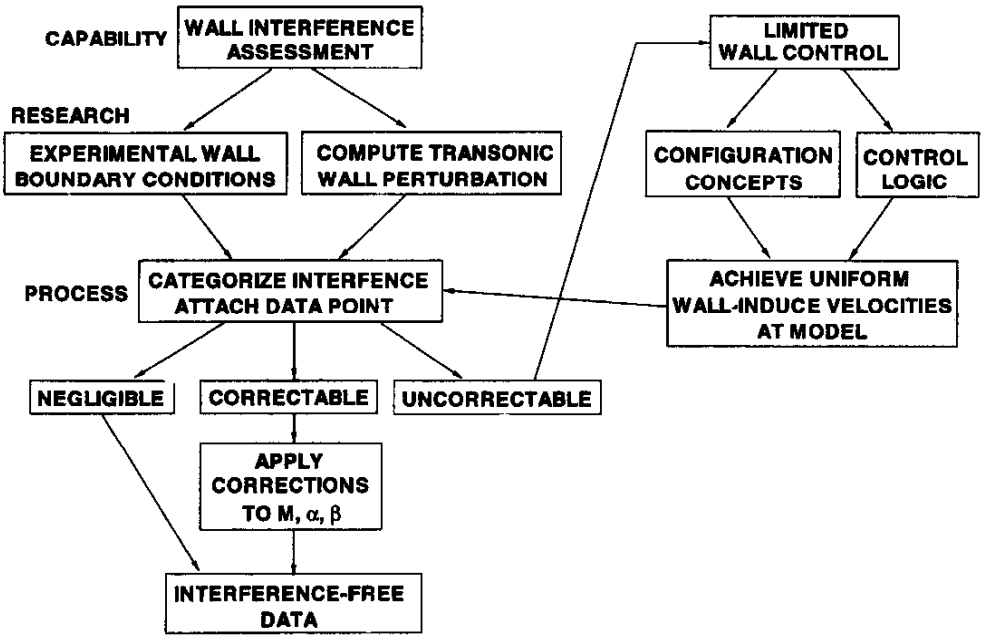

Figure 5.1 : The correctable interference transonic wind tunnel concept

"The correctable-interference transonic wind tunnel would combine the capability for assessment of wall interference with a limited capability for wall control. Four primary areas in which research is needed to achieve these capabilities are noted on Figure 5.1. The interference assessment capability would be used to categorise the interference existing at each test condition as negligible, correctable, or uncorrectable using criteria which could be adjusted according to the data accuracy required for the test. Wall control would be used only for those conditions assessed as uncorrectable and only to the extent necessary to achieve a correctable condition, thus the wall-control requirements are less restrictive than those for a self-correcting tunnel and possibly could be achieved with a simpler wall mechanisation. The assessment and control capabilities would be combined to search out a test section configuration which maximises the range of test conditions falling in the negligible or correctable interference categories. This configuration would then become the standard fixed geometry test section used for the bulk of the wind-tunnel tests, thereby providing a high productivity rate. The results discussed in the preceding sections imply that the interference assessment and correction capability can be achieved using the data normally measured on a wind-tunnel model, supplemented by the survey over a control surface near the walls of

only a single flow parameter rather than the two independent parameters required for the self-correcting tunnel."

Beyond the foregoing, correctability, which is a major issue for transonic testing will be not be discussed extensively here, except for Section 5.3.2.3.

This chapter will give some perspectives on transonic wind tunnel wall correction methodology. Modern computational fluid dynamics (CFD) methods will be reviewed, including augmentation of the interference prediction techniques with experimental measurements. An update of treatment of wall boundary conditions will be provided. These two topics will be addressed from the viewpoints of Arnold Engineering Development Center (AEDC), McDonnell Douglas and NASA Langley. It should be noted that wall boundary conditions remain the central issue in modelling transonic wind tunnel flows. To complement the CFD discussion, an overview of combined asymptotic and numerical (CAN, **C**ombined **A**symptotic and **N**umerical) procedures will be provided. Finally, prospects for the future will be briefly indicated.

5.2 WALL BOUNDARY CONDITIONS FOR TRANSONIC FLOWS

To predict wall interference at transonic speeds, some sort of non-linear boundary value problem involving the gasdynamic equations of motion needs to be solved. For this problem to be properly posed, appropriate boundary conditions are crucial. Obtaining these conditions for the variety of ventilated walls used to mitigate shock reflections in transonic testing is challenging, and in some cases overwhelming, since the small-scale fluid-mechanical interactions can be quite complex, involving the effect of injection and suction in wall boundary layers leading to complex flow patterns. These are exemplified by return jets and vortical structures in perforated, slotted, and baffled slotted wind tunnels. The specification of boundary conditions is further complicated by the possibility of turbulence and coupling of flow and tunnel-wall boundary vibrations.

Obviously, a detailed solution of these small-scale flows may be impractical and not warranted in obtaining rapid assessments of interference by the test engineer. This view is clarified by formulating the wall interference problem as a multi-scale asymptotic problem in which one scale is the local flow near the wall ventilations, with a length comparable to wall openings; another is the main flow for a length scale comparable to the wall height, or characteristic model dimension. This approach is exemplified by matched asymptotic procedures used by Berndt [24] and others. In these models, only the far field boundary conditions of the ventilated wall boundary layer flow are important for the interference problem. Empirical methods and other techniques such as those developed by Mokry, *et al.* [133] which require pressure measurements near the walls have been proposed instead of these conditions. The latter are associated with the previously mentioned Wall Interference Assessment and Correction (WIAC) approaches. For large blockage situations associated with achieving high unit Reynolds near flight conditions, the nonlinearities and complexities of the wall and model viscous flows become important. Current integral and empirical methods of handling these cases will be subsequently covered.

The discussion that follows gives an overview of some procedures that are currently in use to formulate wall boundary conditions. Solid wall tunnels are discussed first, followed by the traditional porous and slotted wall geometries, and ending with the more recently developed baffled slot geometry. Related work on slotted wall design to minimise transonic interference and choking is also discussed.

5.2.1 NOMENCLATURE FOR SECTION 5.2

A	Area, also slotted-wall boundary condition coefficient (see equations 5-9 and 5-16)
B, B'	Slotted-wall boundary condition viscous coefficients
C_D	Discharge coefficient
C_L	Lift coefficient
C_M	Pitching moment coefficient
C_p	Local pressure coefficient
C_{ps}	Slot pressure coefficient
C_{pw}	Wall pressure coefficient
D	Measured (known) terms in boundary condition evaluation
D_F	Unknown (least-squares-fit) terms in boundary condition evaluation

d	Porous wall hole diameter or slot spacing
H	Tunnel height
h	Tunnel semi-height
K	Slotted-wall streamline curvature coefficient
k	Nondimensional slotted-wall streamline curvature coefficient, $= K\frac{d}{h}$
k_1, k_2, k_3	Interference factors
L	Wall hole length
m	mass flow rate
P	Local static pressure
q_∞	Freestream dynamic pressure
R	Classical wall porosity factor
T	Total temperature
t	Depth (thickness) of slotted wall
U	Inviscid edge velocity
V_n	Equivalent inviscid normal velocity
V_w	Wall crossflow velocity
u, v, w	Perturbation velocity components
α	Angle of attack
ΔP_w	Pressure drop across the wall
δ^*	Local boundary layer displacement thickness
ε	Orifice coefficient
η	Wall porosity
θ_s	Flow angle in slot
θ_w	Flow angle at wall
λ	Wall mass flux
ν	Prandtl-Meyer angle
ρ	Density
τ	Wall openness ratio, percent
ϕ_x, ϕ_y	Potential gradients
χ	Hole inclination angle

Subscripts:

ff	Far field
n	Normal to tunnel wall
te	Tunnel empty
w	At the wall
∞	At infinity or in the free stream

Abbreviations:

AEDC	Arnold Engineering Development Center
LaRC	Langley Research Center
MDA	McDonnell-Douglas Aerospace
NASA	National Aeronautics and Space Administration
NTF	National Transonic Facility
NWTC	National Wind Tunnel Complex
PSWT	Poly Sonic Wind Tunnel
TWT	Trisonic Wind Tunnel
WIAC	Wall Interference Assessment and Correction
WS	Weak supercriticality

5.2.2 SOLID WALLS

Transonic testing in solid wall wind tunnel facilities presents significant challenges to the engineer wishing to acquire quality aerodynamic data. In particular, as the test Mach number exceeds 0.87-0.90 for three-dimensional flows, and even much lower speeds for two-dimensional airfoils (depending on the thickness and lift), the effects of solid blockage due to an improperly sized model and its support system may severely limit or even prevent testing. For models sized in the 0.5-percent range, experience has shown that drag divergence may be significantly different than that obtained for a 0.25-percent blockage model. Furthermore, the wall-induced interference may be of such magnitude that the data are uncorrectable (i.e., no free air condition exists to which the data may be corrected).

In transonic flow with solid walls, wall viscous effects **must** be considered. At high transonic Mach number, interactions with the tunnel wall may be unstable due to shock wave impingement on the wall boundary layer. This interaction may cause the wall boundary layer to cyclically thicken and thin, and/or separate and reattach, yielding unsteady interference corrections to the supposedly steady aerodynamic data. Even when the shock does not impinge directly on the wall, the sensitivity of high Mach number flows to effective tunnel cross-sectional area changes requires that the wall-normal velocity be determined from the rate of change of the wall boundary layer displacement thickness. Typically, this normal-velocity boundary condition is zero for inviscid, flat solid walls and is approximated as such for low speed, incompressible flows. Wall viscous blockage due to the stagnation point near the model leading edge responds to the local model pressure field, appearing first as a thickening and then as a thinning of the wall boundary layer as the flow traverses the region. This phenomena effectively creates a nozzle which can reverse the normal effect of the pressure gradient on flat or mildly diverged walls. In other words, the corrections are opposite in sign to those normally obtained.

Several approximate treatments of the interaction of the model pressure field with the boundary layers on the solid sidewalls in an airfoil tunnel have been developed and used to obtain wall interference correction contributions. Basically, the effective-inviscid shape of the sidewall is no longer a flat reflection plane; the large pressure gradients due to the model are imposed directly upon the sidewall boundary layers resulting in appreciable nonplanar, effective-inviscid distortions and adversely impacting the desired 2-D symmetry. At low subsonic Mach numbers and for wide tunnels, this distortion is limited to a small region at the sidewalls. However, as the Mach number increases, this distortion can destroy the 2-D symmetry. At

places where the flow becomes mildly supersonic, generally a bubble between the forward sonic locus and the terminating shockwave, the flow characteristics are nearly perpendicular to the streamlines, permitting propagation of pressure disturbances directly across the tunnel from the sidewalls.

In a series of papers, Barnwell [18], Barnwell and Sewall [19], and Sewall [166] showed that a similarity rule can be derived and used, in lieu of a boundary condition, to approximate this sidewall influence. In this rule, a Mach number shift, which depends on the nominal test Mach number and tunnel-empty sidewall boundary-layer parameters at the model location, can be identified as a Mach number correction. This correction is generally of opposite sign to that normally expected in a solid wall tunnel. It was subsequently shown by Ashill [11] and Murthy [137] that this sidewall boundary-layer correction to the Mach number also depends on the model aspect (or tunnel width to model chord) ratio. These approximations are based on subsonic flow ideas and have been incorporated in a number of airfoil tunnel correction codes, even for mixed (transonic) flow. However, at high subsonic flow on modern blunt airfoils, the approximations may become invalid when the forward sonic point is very near the airfoil leading edge (see, for example, Gumbert, *et al.* [81]).

The interaction of the model pressure field with the boundary layers on solid walls in 3-D has been similarly approximated by Adcock and Barnwell [2] where it was found that the Mach number correction is relatively less than in 2-D, but still appears to be of opposite sign than that expected for solid walls. That is, the tunnel appears to be more open around the model than what is indicated by the conventional solid (closed) wall correction. The phenomena is also very important in semi-span model testing at high subsonic and transonic Mach numbers; however, it appears that these sidewall boundary-layer approximations have not been used. Instead, one attempts a more rigorous CFD solution for the interaction as will be discussed in section 5.3.1.5.

Ashill's method applied to a three-dimensional, high-transonic Mach number experiment (Ashill *et al.* [14]) necessarily included the wall-normal velocity computed from the tunnel wall boundary layer to extend the method to a freestream Mach number of about 0.9. This application represents the extreme upper limit for linear methods applied to weakly supercritical (Group 1) flows; while the transonic Laminar Flow Control Experiment (Harris, *et al.* [82]) with a completely three-dimensional aerodynamically- and viscous-contoured tunnel liner (Newman, *et al.* [141]) represents a case for highly supercritical (Group 2) flows.

Because transonic open jet tunnels are unsteady and have large power requirements; because solid wall tunnels are very sensitive to area change at high Mach number; and, because the flow in both open jet and solid wall tunnels yield physically inappropriate flow solutions which have corrections of opposite sign, the aerodynamicist must resort to wind tunnels with either ventilated walls or those which have an adaptive capability. A discussion of adaptive wall boundary conditions and technologies is presented in detail in Chapter 10. The remainder of Section 5.2 will discuss boundary conditions applicable to porous wall, slotted wall, and baffled-slotted wall wind tunnels.

5.2.3 Porous Walls

5.2.3.1 McDonnell-Douglas Porous Wall Boundary Condition

Numerical simulation of wind tunnel flow fields in a ventilated transonic test section requires proper modelling of the walls. This is particularly true for transonic wind tunnel wall interference correction. Several current concepts for predicting or correcting ventilated test section data for wall interference

involve the numerical simulation of an aircraft model in the wind tunnel, and in free-flight (Crites [41]; Rueger and Crites [160]; and, Sickles and Erickson [168]).

As pointed out in the literature (Kraft [107]; and, Rueger and Crites [160]) precise agreement between computed model pressure distribution (or forces) and measured values is not necessary in order to obtain accurate corrections. The corrections are based on the difference between two solutions, with the simulation of the aircraft model common to both. Significant error in the simulation of the model will be minimised.

The same is not true for simulation of the tunnel wall. The effect of the wall is precisely the object of the exercise. Errors in modelling its interaction with the main flow are reflected as errors in the correction. The degree of fidelity required in modelling the ventilated wall depends on the type of wall, and how strongly the aircraft model flow field interacts with it. There is evidence that for a relatively large tunnel with a relatively small model, the classical linear wall boundary condition

$$R\phi_x + \phi_y = 0$$

is adequate (Kraft [107]; Phillips and Waggoner [149]; and, Steinle [174]). In such cases all that is necessary is the determination of R at the wall pressure ratio characteristic of normal operation (Matyk and Kobayashi [127]).

Smaller transonic tunnels (such as the McDonnell Douglas Aerospace 4-foot x 4-foot PSWT) use relatively large models to reduce model infidelity and improve Reynolds number simulation. As a result the model flow field interacts more strongly with the wall. The linearised wall flow boundary conditions fail to provide useful interference corrections. It seems likely that this is also true for larger tunnels when testing very large models.

5.2.3.1.1 EXPERIMENTAL SET-UP

The wall flow boundary condition was determined from experimental data taken on a set of ventilated plates simulating various transonic walls. This effort was conducted in the 1x1-ft. transonic test section of the MDA Trisonic Wind Tunnel (TWT). (Note: Similar experiments were conducted by Freestone and Henington [61].) Figure 5.2 illustrates the basic set-up. A can (isolated plenum) within the transonic plenum is attached such that various test plates (ventilated wall samples) can be mounted flush with the transonic wall. The flow into or out of the can is controlled and measured by sonic flowmeters. A dozen taps are located over the face of the test plate to record the static pressure distribution. Just upstream of the test plate, several rows of perforated holes in the tunnel wall were connected to a manifold and used to apply suction or blowing to alter the approaching boundary layer.

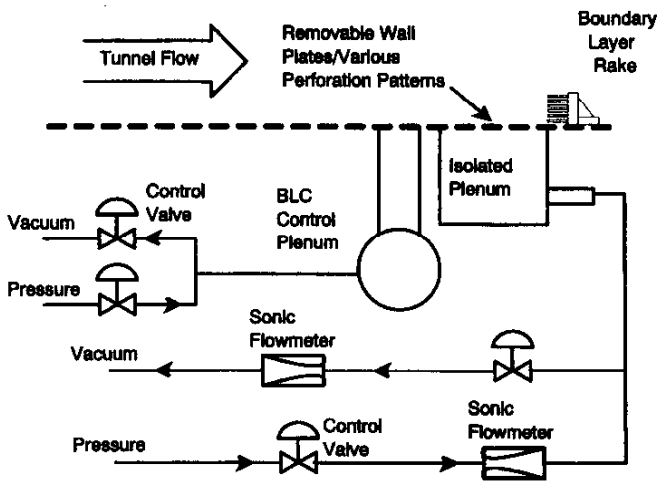

Figure 5.2 : Wall Cross-Flow Test Set-Up

Figure 5.3 defines the geometry of the five test plates evaluated. The first of these is the same 22.5% perforated wall used in the 1-ft. tunnel. The second represents the wall of a 4x4-ft. blow down tunnel scaled according to boundary layer displacement thickness typical in the two tunnels. Plates 3 and 4 are also 22.5% porosity, but hole diameter and plate thickness differ. Plates 1 through 4 are typical of the design previously investigated by Chew [36]. Plate 5 is a 6% porous, 60-degree inclined hole design typical of the transonic walls investigated by Jacocks [88].

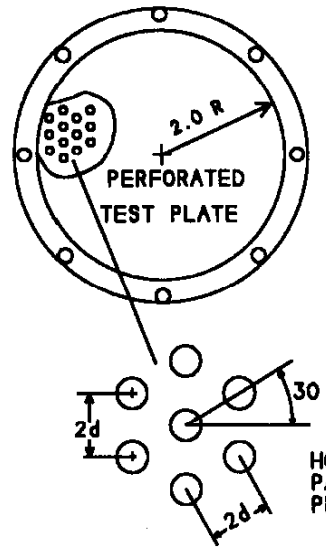

PLATE	d	L	η	θ
1	.125	.125	.225	0
2	.150	.300	.225	0
3	.062	.125	.225	0
4	.062	.300	.225	0
5	.125	.250	.060	60

NOTES: L IS HOLE LENGTH WHICH IS PLATE THICKNESS, EXCEPT FOR PLATE NO. 5.

PLATE 5 HAS 60 DEG. INCLINED HOLES.

Figure 5.3 : Wall Cross-Flow Test Plates

5.2.3.1.2 EXPERIMENTAL PROCEDURE

The test was designed to measure wall crossflow as a function of wall pressure. Variables were Mach number, Reynolds number, boundary layer thickness, hole diameter, wall thickness, and hole inclination angle. Admittedly, some of these variables were not exercised very extensively. For instance, there were only two hole inclination angles tested, and the inclined hole data were for only one hole diameter and wall thickness.

There were two parts to the test. The first involved determining the boundary layer characteristics of the flow at the upstream edge of the test plate. This was done by mounting a boundary layer rake (of total pressure tubes) at the leading edge of the test plate and exercising total pressure and Mach number to cover the test range. Some measurements were taken with typical levels of blowing from the test plate to see if the effects would propagate forward and invalidate the rake data. During this portion of the test, crossflow data were not taken due to interference from the boundary layer rake. During the second portion of the test the boundary layer rake was moved downstream and used to measure boundary layer characteristics of the flow at the downstream edge of the test plate. Wall crossflow data were acquired during this portion of the test.

A full discussion of this effort, including the development of a mathematical model of the wall crossflow process was reported in the literature (Crites and Rueger [42]). Only highlights of this effort are included here.

5.2.3.1.3 AIR-OFF RESULTS

Wall crossflow was measured for blowing and suction with no primary tunnel flow. The results for the various plates were correlated according to the relation

$$\frac{m\sqrt{T}}{C_D PA\eta} = K\sqrt{\frac{\Delta P}{P}}$$

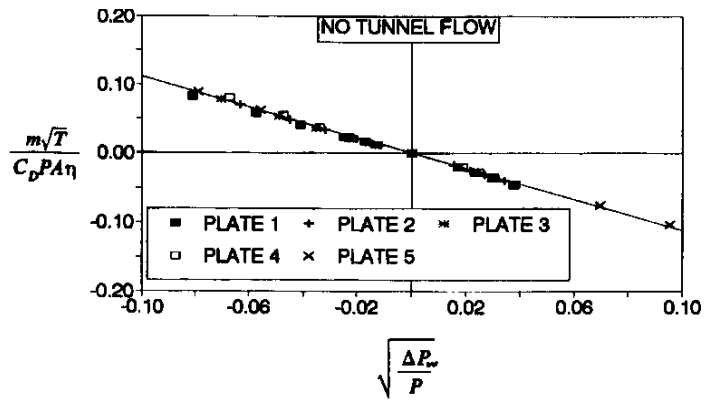

Figure 5.4 : Cross-Flow Characteristic (No Tunnel Flow)

The theoretical value of K is -1.098 for the chosen sign conventions. The value providing the best fit to the data for all five plates is -1.112. The results are shown in Figure 5.4. The discharge coefficient, C_D, values for each plate were experimentally determined and range from about 0.7 to 0.8.

5.2.3.1.4 AIR-ON RESULTS

For air on, it is common to normalise the crossflow by the freestream condition. The normalised crossflow velocity is defined as

$$V_w = \frac{(\rho v)_w}{(\rho U)_\infty}$$

and the wall pressure coefficient is given by

$$C_{pw} = \frac{\Delta P_w}{q_\infty}$$

When comparing different wall configurations, it becomes obvious that C_{pw} is not adequate to correlate the crossflow characteristics. Figure 5.5 shows the crossflow characteristics of all five test plates at Mach 0.6. Although the characteristics are well defined, there is not a high degree of correlation.

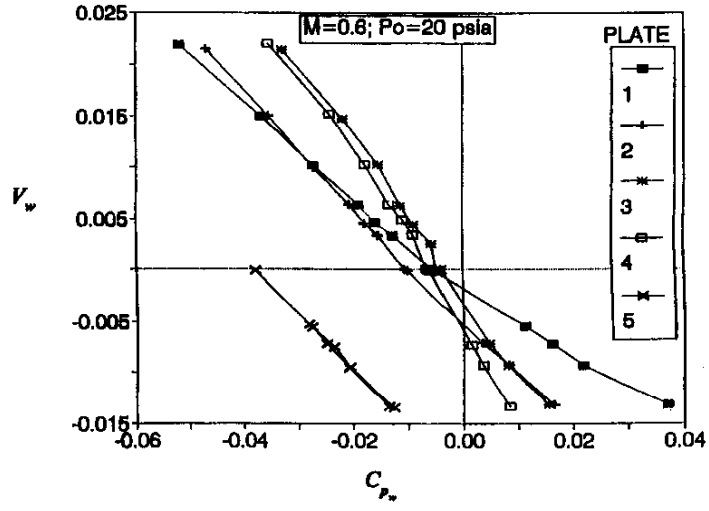

Figure 5.5 : Cross-Flow with Tunnel Flow

Based on physical reasoning, a new independent variable was defined. Specifically

$$C_{p'} = C_{pw}\sqrt{\frac{\delta^*}{d}}$$

Further investigation revealed that the physical process in the individual holes is different for outflow (suction) than inflow (blowing). In suction, the flow

pulled into the holes carries considerable x-momentum. This leads to an impact pressure on the downstream side of the holes that is considerably above local static pressure. This forces some flow through the holes, but also creates a circumferential flow that results in a fountain near the upstream edge of the holes — ejecting air back into the freestream. In the absence of a pressure drop across the wall, viscous entrainment of the air in the holes causes an offset in the crossflow characteristic. That is, $V_w < 0$ when $\Delta P_W = 0$.

In blowing, plenum air with very little momentum is ejected into the freestream. Since the velocity in the plenum is very small, no x-directed momentum is carried into the hole, and the crossflow characteristic is changed. In addition, it is necessary to account for the differences in relative edge sharpness due to the hole size and fabrication method. This was done by including the discharge coefficient, C_D, obtained for the no-tunnel flow condition.

Other factors considered were, the effects of hole inclination, and the offset in V_W at $C_{PW} = 0$. The final result was a correlation which collapses the data for all five perforated plate geometries. For $V_w>0$, this correlation is

$$\frac{V_w}{\eta C_D \cos^2(\theta)} = a_1 \Delta C_p + b_1 \sqrt{\Delta C_p}$$

with $a_1 = -1.557$, $b_1 = -0.2242$. For $V_W<0$, the correlation is

$$\frac{V_w}{\eta C_D \sqrt{\frac{L}{d}} \cos^2(\theta)} = a_2 \Delta C_p + b_2 \sqrt{\Delta C_p}$$

with $a_2 = -2.047$, $b_2 = -0.0304$, and

$$\Delta C_p = C_{p'} - C_{p'}|_{V_w=0}.$$

Note that for blowing, $V_w > 0$, the quadratic dependence on pressure is much greater than for suction, $V_w < 0$.

Figure 5.6 shows data from all five perforated wall designs for Mach 0.6. The correlation given successfully collapses the entire data set.

V_w, the wall crossflow, is not the correct boundary condition for an inviscid flow solver. The displacement effect of the boundary layer must be included. The equivalent normal velocity (flow angle) at the wall surface, V_n, is needed. Conservation of mass for an elemental control volume at the wall surface requires that

$$V_n = V_w + \frac{1}{(\rho U_\infty)} \frac{d(\rho U \delta^*)}{dx}$$

where density variations are ignored because, typically, they are small, except for strong shocks at the wall.

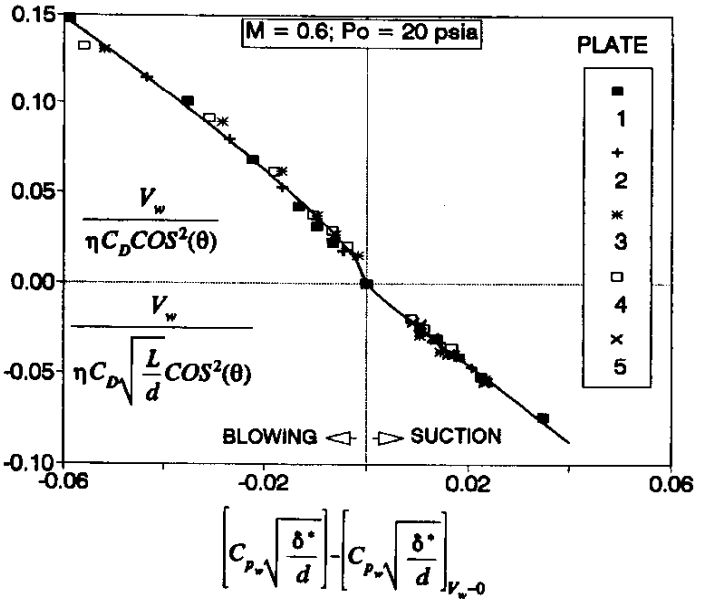

Figure 5.6 : Cross-Flow Characteristic Correlation

The well known incompressible relation,

$$C_p = -2\phi_x$$

can be used with good accuracy for typical transonic wall region flows to eliminate U in favour of C_P. The result is

$$V_n = V_w + \frac{d\delta^*}{dx} - \frac{\delta^*}{2}\frac{dC_p}{dx}$$

V_W is known from the measured mass flow through the wall. The gradients in δ^* and C_P are computed from measured boundary layer and wall pressure data.

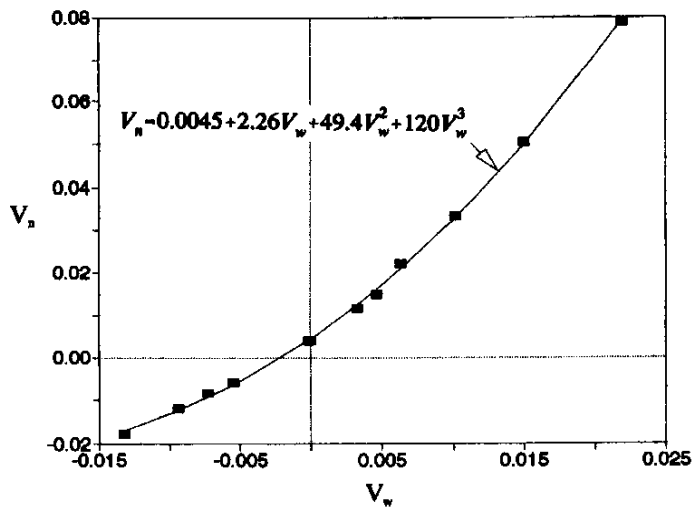

Figure 5.7 : Effective Normal Velocity versus Cross-Flow

The result allows the calculation of V_n corresponding to the crossflow, V_W, mean pressure coefficient, C_{pw}, and mean boundary layer thickness, $(\delta^* + \delta_1^*)/2$. As shown in Figure 5.7, V_n correlates directly with V_w. Specifically,

$$V_n = a_0 + a_1 V_w + a_2 V_w^2 + a_3 V_w^3 .$$

This direct dependence of V_n on V_w has been noted by others (Agrell [6]; and, Barnwell [20]). The relationship seems very robust. In fact the same dependence can be deduced from published data (Baronti, *et al.* [22]) for laminar boundary layers with transpiration at the wall.

Note that

$$\frac{d\delta^*}{dx} = V_n - V_w + \frac{\delta^*}{2}\frac{dC_p}{dx} ,$$

completes a set of equations that can be solved numerically for the unknown values V_w, δ^*, and $V_n(x)$.

Solution presumes that values of measured, or interpolated wall pressures are available on two-dimensional strips running the length of the test section. The number of strips depends on the CFD grid, or panel distribution simulating the wall. In addition, starting values of displacement thickness at the test section inlet, δ_0^*, must be known. With these starting conditions any of a number of numerical techniques can be used to march the solution downstream. A conventional Runge-Kutta integration scheme is used to obtain solutions.

Figure 5.8 shows typical results for the ceiling centreline for a recent wind tunnel test. Note that the desired boundary condition, V_n, is different than the crossflow V_w.

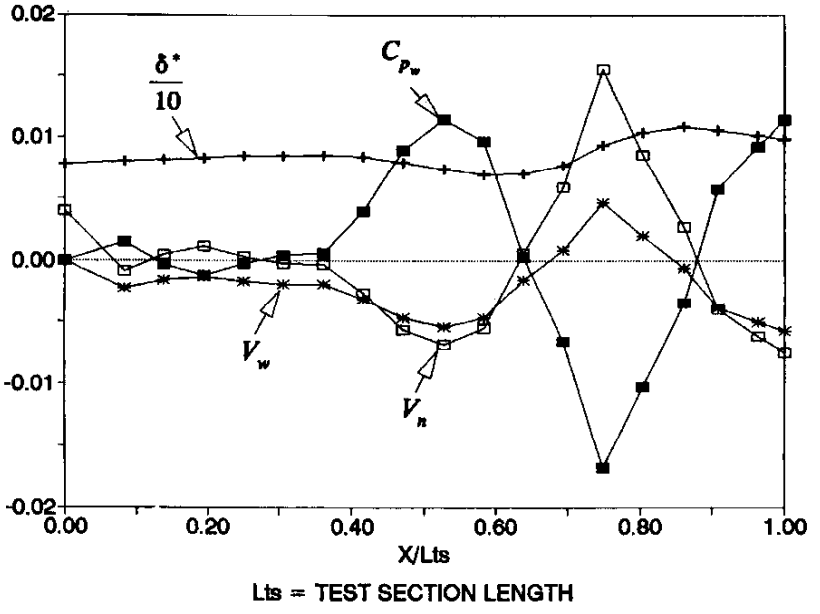

Figure 5.8 : Typical wall boundary solution computed on centreline

5.2.3.2 AEDC PERFORATED-WALL BOUNDARY CONDITION

Perforated walls have been shown to be effective in minimising wall interference and have allowed testing through the transonic regime. On the other hand, they have introduced the enormous challenge of characterising the wall behaviour and correcting the test article data for the remaining wall interference. Requirements for larger test articles and higher quality data make the challenge more difficult and more critical. To precisely compute the wall interference effects using modern CFD techniques, an accurate model of the wall behaviour is essential. In addition, the wall model must provide stable and robust results when incorporated as a boundary condition in a numerical algorithm. The challenge of developing an accurate wall model is particularly difficult at transonic conditions where the wall behaviour is dependent on a complex relationship of local flow conditions. Classical definitions of the wall behaviour for perforated walls (Garner, *et al.* [67], Pindzola and Lo [151]) have been shown to be inadequate at transonic speeds for the aforementioned requirements.

Classical perforated wall boundary conditions assume a fixed global and homogeneous description of the wall characteristic, which is defined as the ratio of the pressure coefficient difference across the wall to the flow angle at the wall. Because the hole diameter of the perforations is small compared to the tunnel dimensions, the local effect of the discrete holes diminishes rapidly, and homogeneity is a reasonable assumption. However, the measurements made by Jacocks [88] of the local flow properties in the vicinity of perforated walls indicate that a fixed global specification of the wall characteristics is not adequate and that local specification is necessary. This is particularly important at transonic conditions and for large test articles where the wall gradients are large and the local flow properties change drastically. The data in Jacocks [88] show that the boundary-layer displacement thickness is one of the most important parameters to consider when quantifying the wall characteristic. Because of the large gradients at the wall generated by the test article, there is significant spatial variation in the boundary layer displacement

thickness within a perforated wall test section. Therefore, the challenge reduces to defining a wall characteristic in terms of the pertinent local variables.

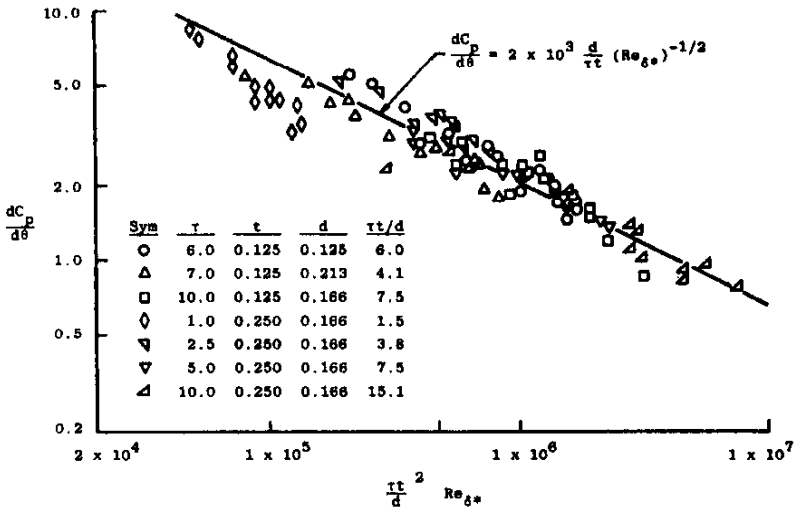

Figure 5.9 : AEDC perforated-wall displacement thickness correlation

For the AEDC perforated walls, having perforation holes inclined 60° from wall-normal direction, Jacocks [88] has found an empirical crossflow characteristic illustrated in Figure 5.9. The homogeneous pressure coefficient at the wall, expressed as a function of the local flow angle has the approximate slope

$$\frac{dC_p}{d\theta} = 2000 \frac{d}{\tau t} \mathrm{Re}_{\delta^*}^{-1/2} \quad (5\text{-}1)$$

where t is the wall thickness, d is the hole diameter, τ is the wall open area ratio in percent, C_P is the pressure coefficient difference across the wall and Re_δ is the unit Reynolds number based on δ^*, the boundary-layer displacement thickness. It should be mentioned that Reynolds number was not an independent variable in the experiments discussed in Jacocks [88]. Therefore, the correlation may not be universal. However, the correlation is descriptive of the observed behaviour for AEDC perforated walls as Reynolds number is changed, *i.e.*, as Reynolds number increases, the perforated wall behaves as if it were more open (Jacocks [88]).

In order to incorporate this empirical correlation into the solution of the tunnel flow field, the boundary-layer displacement thickness on the wall must be calculated. To compute the boundary-layer displacement thickness on the perforated wall in an inviscid flow-field calculation, an approximate technique has been devised using insight gained from previous computations with a more exact method (Whitfield [182]). The continuity equation in integral form may be written as

$$\frac{1}{\rho u} \frac{d}{dx} (\rho u \delta^*) + \theta - \lambda = 0 \quad (5\text{-}2)$$

where λ is the wall mass flux defined such that outflow from the test section is considered positive, ρ is the density and u is the component of the velocity in the freestream direction. In principle, to solve (5-2), a streamwise momentum equation is needed. However, previous computations of permeable wall turbulent boundary layers in Jacocks [88] and Erickson and Homicz [52] indicate that the flow angle and wall mass flux are nonlinearly related and can be expressed as

$$\theta - \lambda = 0.125\theta \left[4 - \theta \left(55 + 250\theta\right)\right] - 0.002 \quad (5\text{-}3)$$

The correlation of (5-3) can then be used to integrate (5-2) and determine the distribution of δ^*. Initial upstream conditions for the boundary-layer calculations are provided by a correlation of data from three transonic wind tunnels at AEDC. The correlation, shown in Figure 5.10, relates the displacement thickness at the test section entrance to Reynolds number and tunnel size as

$$Re\delta^* = 0.11 Re_H^{4/5} \qquad (5\text{-}4)$$

where H is the tunnel height.

This wall model has been successfully incorporated as a boundary condition into several flow solvers. The boundary condition has been shown to be both stable and robust. It should be emphasised that the far-field tunnel flow field is solved inviscidly using Euler equations while the test-article near field can be solved using either Euler or Navier-Stokes equations depending on the importance of near-field viscous effects. This boundary condition has been successfully applied at AEDC for steady subcritical and supercritical flows at subsonic freestream Mach numbers (Donegan, *et al.* [47], and Sickles and Erickson [167], [168]) and for low supersonic freestream Mach numbers (Martin [126]).

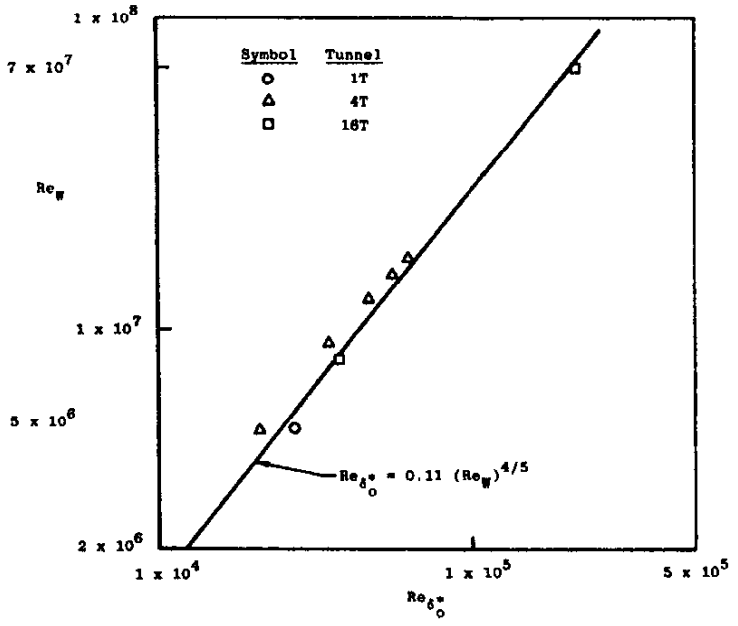

Figure 5.10 : Test section entrance characteristic correlation data

The wall model is incorporated in a time marching algorithm as follows. Using the distributions of ρu and θ at the walls, which are supplied by the inviscid numerical solution, the boundary-layer displacement thickness δ^* is calculated, the local wall characteristic is determined from (5-1), and the wall pressure P_W is computed as

$$P_w = P_\infty + q_\infty \theta \frac{dC_p}{d\theta} \qquad (5\text{-}5)$$

where q is the dynamic pressure, C_p is the pressure coefficient and ∞ subscripts refer to freestream conditions. The wall pressure is then incorporated into a CFD flow solver as a boundary condition by specifying the internal energy e at the walls to be

$$e = \frac{P_w}{(\gamma - 1)} + \frac{1}{2}\rho(u^2 + v^2 + w^2) \qquad (5\text{-}6)$$

where v and w are velocity components perpendicular to u, and γ is the specific heat ratio.

The wall boundary condition is updated at each iteration in the numerical solution based on the most recent calculation of the flow parameters.

The conclusions drawn from the work of Jacocks are confirmed by the results of Crites and Rueger [42]. They, through separate experiments, developed a similar wall model. Figure 5.11 shows a comparison between the boundary-layer amplification factors λ from (5-3) for the two correlations. The agreement is excellent within correlation range ($-0.02 < \theta < 0.02$ radians) but differ at larger flow angles. For large models, the flow angles may extend beyond the correlation range and additional effort and data must be obtained to extend the correlation with confidence.

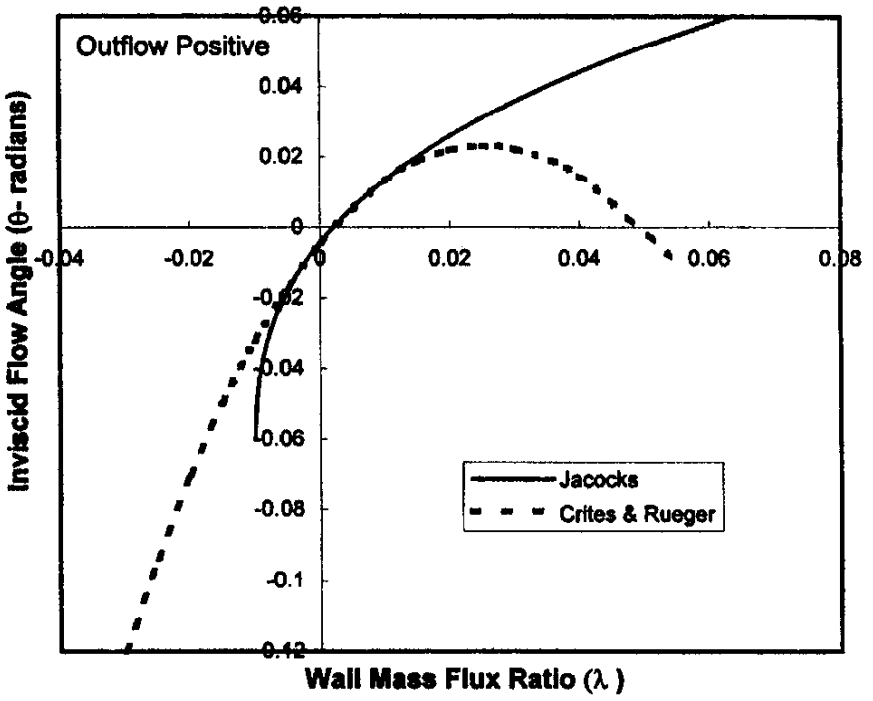

Figure 5.11 : Inviscid flow angle versus wall mass flux ratio

5.2.3.3 Freestone Porous Wall Studies

In solid wall tunnels, measured boundary flow variables are relatively easy to obtain, with longitudinal velocities determined from pressure measurements and normal velocities prescribed as zero. A higher-order specification of the normal velocity may be obtained, if required, by computing the effect of the wall boundary layer. However, significant challenges arise when making boundary measurements along ventilated, transonic walls because the wall pressure there is, typically, not a good, average (or homogeneous) representation of the rapidly varying flow near and through the wall, and devices such as rails or pipes must be used to obtain pressures which are unaffected by the localised effects of the wall geometry (see Chapter 4). Additionally, the normal velocity measured in open regions near the wall is highly dependent on the details of the wall-ventilation geometry and the wall viscous effects, and it must somehow be related to the far field average of the close-wall neighbourhood. In spite of these and other difficulties, the success of the two variable, boundary-measurement method of Ashill and Weeks [13]; (see, also, Chapter 4 in AG-336) for interference correction in solid wall wind tunnels prompted Freestone, Gascoigne, and Lock [63] to investigate its transonic extension to a tunnel with a single 6-percent-open wall with uniformly-distributed, 60-degree inclined perforations. A NACA 0012 airfoil at zero lift was used as the disturbance model. Static pressure measured along lines on the walls were assumed *sufficiently* close to the far field average to yield accurate values of the streamwise velocity—no further accuracy assessment was given. Correlation experiments (Freestone and Henington [61]) were conducted to characterise the normal velocity variation with wall pressure drop (wall pressure minus plenum pressure) and boundary layer displacement thickness. Consistency checks between the measured and calculated values of boundary-layer displacement thickness revealed significant discrepancies for the blown boundary layer which occurs for tunnel inflow conditions. For these regions,

predictions underestimated the measured growth rate by a factor of two to three, requiring an empirical velocity correction for these effects. The corrected boundary data were then used as input to Ashill's method to obtain Mach number and upwash distributions on the tunnel centreline which, then, were used to correct the airfoil test data. Comparisons between the tunnel data and free-air computations and comparisons with that acquired in a large tunnel were generally good, implying that the application of the correction technique in ventilated tunnels is feasible.

5.2.4 SLOTTED WALLS

The reader is referred to Chapter 3.2 and Figure 3.3 for a general discussion of the slotted wall and its geometry. For slotted walls, the associated geometric length scales are the slot width, a, the slot spacing, d, and the tunnel semi-height, $h=H/2$. Historically, an infinite number of longitudinal slots are assumed when developing the wall geometry model, while inviscid flow is assumed for the fluid-dynamic model. This leads to the relatively simple forms of the boundary condition given by equation (3.9), and classical solutions have been developed accordingly (for example, Davis and Moore [46]). The inability of the classical boundary condition to properly account for wall effects at transonic Mach numbers, under high-lift test conditions, and for large wind tunnel models has been particularly evident since the advent of computational fluid dynamics where significant discrepancies were revealed between computation and experiment. As with porous wall boundary conditions, the impact of wall viscous effects have been recognised as significant and an area where much research needs to be conducted. The importance of the boundary-layer displacement thickness, δ^*, as a viscous length scale, has become increasingly apparent, and other scales may exist for the low-energy flow re-entering the test section downstream of the model. This section summarises recent slotted-wall boundary condition research beyond the classical approach presented in Chapter 3, particularly, as applied to wind tunnel testing at transonic Mach numbers.

5.2.4.1 FREESTONE SLOTTED WALL STUDIES

Freestone successfully applied Ashill's method (see Chapter 4) to porous wall tunnels (see section 5.2.3.3) and, then, investigated its application to tunnels with slotted walls. In ventilated-wall tunnels, the experimentalist has the difficult task of measuring the two flow variables directly, such as u and v (via pressure and flow direction, respectively), or measuring a single flow variable and obtaining the other using a theoretical representation of the boundary condition—both methods were evaluated by Freestone, Mohan, and Lock. Their initial, verification study (Mohan, *et. al.* [132]) was in a low-speed, two-dimensional tunnel where they chose the latter approach. Longitudinal velocities at the boundary were determined from the wall pressures measured on the slat centreline, and normal velocities were determined from the pressure drop across the tunnel wall using the wall boundary condition developed by (Berndt [24], see section 5.2.4.2). They extended the validation in Freestone *et al.* [64] to two-dimensional flow about an airfoil in the Mach number region covering 0.5 to 0.85. The tunnel was equipped with four 20-percent-open slots each in the top and bottom walls. As in the earlier study, they obtained values of normal mass flux through the slot from Berndt's theory; however, they also evaluated the use of measured normal slot mass flux obtained using flow angle probes. Two significant conclusions were that accurate tunnel-centreline interference distributions may only require normal slot velocity measurements to within 10-percent of their maximum, and that slot velocity distributions may adequately be determine with only a limited number of measurements in each slot. Further two-dimensional work

presented by Freestone and Mohan [62] indicates that, in some situations, wall-interference corrections determined by averaging slot flow measurements can be significantly different from those determined using the Berndt theory. These differences are the result of an incomplete understanding and modelling of the wall viscous effects in regions of low-energy inflow from the plenum; they are not unlike those effects noted at a perforated wall where inflow, also, amplifies the boundary-layer growth rate. Wall velocity magnification factors of 4 to 5 in the inflow regions were required to produce agreement between predicted and observed model pressure distributions. Finally, Mohan and Freestone [131] extended the Ashill method to three-dimensional, low-speed flow in a slotted-wall tunnel about a 25-degree swept, sidewall-mounted wing. The tunnel was equipped with four, 15-percent-open slots each on the top and bottom walls. Slot flow measurements were obtained with a pitch/yaw probe traversed along each slot centreline, while pressure measurements were obtained on the slat centres. Comparing their results with data on the same model acquired with solid walls (also corrected by Ashill's method) allowed them to report correction accuracies of the order 0.05° in upwash and 0.002 in blockage. However, these levels of accuracy were achieved in experiments where low-energy inflow was avoided.

5.2.4.2 Berndt Boundary Condition and Implementation

Berndt and Sörensen [26] derived the two-dimensional, homogeneous-wall boundary condition

$$C_{pw} - C_{ps} = 2\frac{\rho U}{\rho_\infty U_\infty} dK \frac{\partial \theta_s}{\partial x} + \frac{\rho}{\rho_\infty}\theta_s^2 \qquad (5\text{-}7)$$

by integrating the pressure along a two-dimensional spanwise path from the centre of the slat to and through the slot and into the plenum. The analysis neglected shear stress contributions and estimated the value of the slotted-wall performance coefficient K from an inviscid analysis similar to that of the classical Davis and Moore theory [46] but with allowances for the effect of slot depth (wall thickness). The resulting equation essentially combines the functional forms of Davis and Moore with that of Wood [185] who described the wall pressure-drop condition using only a quadratic crossflow term. Transonic validation experiments were conducted at M=0.903 with a circular arc airfoil and oil flow visualisations, flow angles, and pressure measurements were obtained in the slot region. A comparison between theory and experiment using data obtained from Berndt and Sörensen [26] is presented in Figure 5.12 where D and D_F are given by

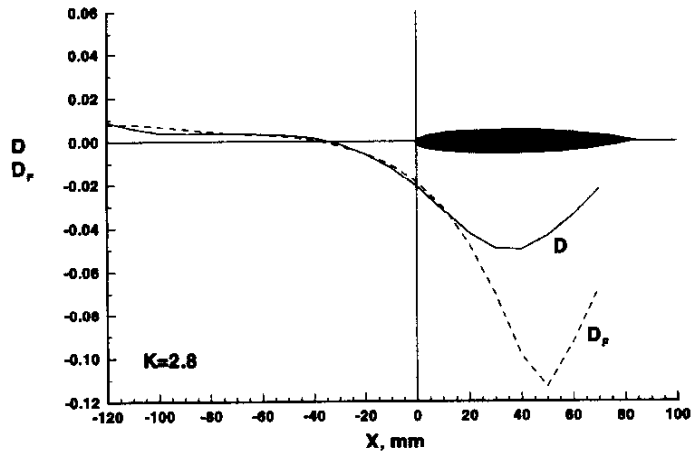

Figure 5.12 : Comparison of Berndt's theoretical two-dimensional, slotted-wall boundary condition with his experimental results for M=0,903. D is the measured wall pressure drop (see equation (5-8a)) and D_F is the theoretical fit of the wall pressure drop (see Equation (5-8b)).

$$D_F = 2\frac{\rho U}{\rho_\infty U_\infty} dK \frac{\partial \theta_s}{\partial x} \qquad (5\text{-}8a)$$

and

$$D = C_{pw} - C_{ps} - \frac{\rho}{\rho_\infty}\theta_s^2 \qquad (5\text{-}8b)$$

The theoretically-determined value of K used in the comparison is 2.8. The airfoil model extends from tunnel station 0 mm to station 90 mm. For outflow through the slots to the plenum

chamber, reasonable agreement between the theory and experiment was achieved upstream of the maximum model-thickness position; however, downstream of this position where the flow returned to the tunnel through the slots and where the effects of viscosity are large, only a few measurements with large uncertainties were obtained and the agreement is poor.

Based on the success of the upstream comparisons and the insight developed from the experimental data, Berndt [24] extended his inviscid theory to three-dimensional walls with a few, narrow slots. The extension used matched asymptotic expansion theory combined with slender-body crossflow theory to develop inner (or near field) and outer representations of the slotted-wall flow field. The resulting family of boundary conditions are local in the sense that variations in slot geometry and plenum pressure are captured in the inner flow representation. The original formulation was developed for axisymmetric flows which are homogeneous in the sense that the slot outer representations are averaged to yield a much simplified wall boundary condition. This simplified boundary condition yields nearly the same result in the vicinity of the model as would be obtained with a full, detailed representation of the wall.

In 1979 Karlsson and Sedin implemented Berndt's boundary condition in a transonic small disturbance code for constant width slots, and then extended this in 1980 to slots with varying width. Their goals were 1) to use the boundary condition to examine the slotted wall interference on axisymmetric models in axisymmetric tunnels at high Mach numbers (M=0.96-0.98) and 2) to design minimum interference slot geometries using an inverse design method. For these flow conditions, the slot geometry and the magnitude of the interference was very sensitive to body geometry and Mach number. Added slot mass flux due to the growth of the wall boundary layers was approximated assuming a turbulent flat plate boundary layer on the slats and these effects were found particularly important and large on the downstream, inflow region, as was observed in the two-dimensional studies. In the downstream region the predicted slot openness was significantly increased over the inviscid, geometric value. The computations were further extended in 1982 by Sedin and Karlsson [164] to asymmetric flow conditions for slender, lifting, delta wings in wind tunnels with constant width slots. The computations showed that negligible pressure interference was difficult to obtain when models were sized to achieve acceptable model Reynolds numbers. Predictions of linear theory were verified in that lift and drag interference were separately minimised for different slotted wall geometries, and that lift interference was reduced when the top-wall slots were opened to larger values than those on the bottom wall. More detailed, but still simple, approximations of the slot viscous effects were included by Sedin and Karlsson [165] via the use of two slot reduction coefficients for the stream-wise slot velocity and the narrowing of the slot width. Rational selection of the coefficient values was based on experimental data and very promising comparisons between computations and measured wall pressure data were presented for freestream Mach numbers of 0.90, 0.95, and 0.98 for 2.23% blockage, axisymmetric models tested in octagonal tunnels, for both shallow (19 mm) and deep (52 mm) slot configurations. As a measure of efficiency, the deep slots were able to maintain a larger pressure difference across the wall than the

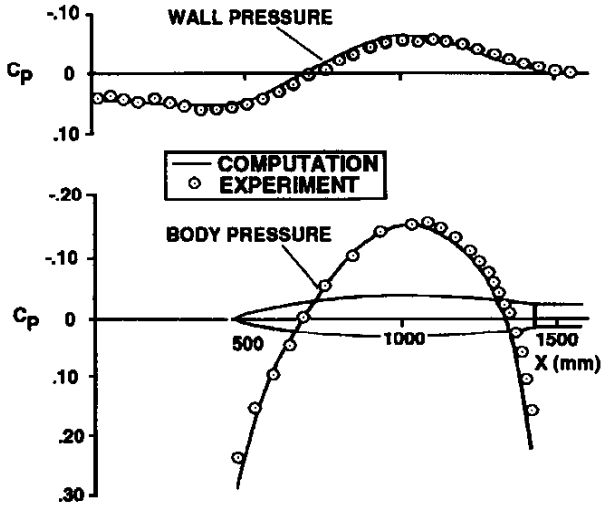

Figure 5.13 : Comparisons of Berndt's three-dimensional slotted-wall boundary condition including viscous slot flow losses with experiment for M=0.9. Deep slot configuration.

shallow slots. Comparison results between the experiment and the computationally determined pressures on the walls and model are presented in Figure 5.13.

Berndt's boundary condition was extended to nonaxisymmetric tunnel geometries by Sedin, *et al.* [163]. Significantly, it loses the property of homogeneity but remains much simpler than solutions which model the details of the slot geometry. Agrell, *et al.* [7] applied the boundary condition to large blockage (1.5%), lifting models in rectangular wind tunnels where they were able to demonstrate the design of slotted walls allowing closely matched aerodynamic test results with freestream conditions. Agrell [6] further applied this code to predict wall interference in measurements obtained on two different models tested in two similar transonic tunnels (one large and one small) at Mach numbers of 0.90 and 0.95 at 0^{O} and 10^{O} incidence. Five different slotted wall geometries were considered for the smaller facility, including one geometry which matched that of the larger facility. Although good results were generally obtained, significant differences were, again, present between computed and measured results which can be directly traced to the inability of the Berndt boundary condition to properly model inflow to the test section where viscous effects become prominent. The solution uncertainty which exists for tunnel inflow conditions where viscous effects are strong is a particular weakness for all forms of the slotted-wall boundary condition. Here, few data exist for either modelling the physics or for validation.

5.2.4.3 LaRC Boundary-Condition Measurements and Correlations

5.2.4.3.1 Overview

The requirement by industry and the research community for high-Reynolds-number transonic aerodynamic data and the maturation of cryogenic-testing technology spurred the development of the National Transonic Facility at the NASA Langley Research Center in the United States (Foster and Adcock [60]). Additional convergent technologies, such as high-accuracy instrumentation with high-data rates, offered the possibility of improved test results with significantly reduced measurement uncertainty. Included in these technologies were the development of mathematical algorithms and computer hardware capabilities suitable for solving complex transonic flow equations for simulations in both free air and in wind tunnels. With these new capabilities wind tunnels could be designed for improved performance, specifically in the region extending from the nozzle to the diffuser, and the test section could be tailored for reduced interference due to the slotted walls (Barnwell [20]; Ramaswamy and Cornette [154]; Newman, *et al.* [143]). However, comparisons of transonic test results with computational wind tunnel solutions revealed significant discrepancies which were traceable to the modelling of the slotted-wall boundary condition. These discrepancies appeared in both the form of the boundary condition and in the value of its associated coefficients. As an example, a modified form of the Ideal slotted-wall boundary condition

$$C_{pw} - C_{ps} = A + 2dK\frac{\partial \theta_w}{\partial x} = A - dK\frac{\partial C_{pw}}{\partial y} \tag{5-9}$$

relating the pressure drop across the wall to the streamline curvature ignores all slot viscous effects and assumes small, negligible flow angles at the wall, conditions which are, generally, incompatible with reality. The *A* coefficient is a necessary, first-order addition to the Ideal slot condition which accounts for the large outflow through the slotted wall due to the growth of the tunnel-empty boundary layer and other effects of tunnel geometry. Tunnel wall boundary layer effects may have a pronounced effect on the wall flow characteristics, particularly for flow returning to the test section from the plenum. In this region, the tunnel wall boundary layers may separate or form a bubble of quiescent air over the slot (Berndt and

Sörensen [26]). Magnification factors of two to four times the local velocity have been used (Freestone and Mohan [62]) to account for this effect on computed interference velocities. The geometry-dependent slotted-wall performance coefficient, *K*, is the value of the potential evaluated in the slot, and must be obtained from appropriate theory (Davis and Moore [46]; Chen and Mears [35]; Berndt and Sörensen [26]; Barnwell [20]) or experiment (Chen and Mears [35]; Baronti, *et al.* [22]; Berndt and Sörensen [26]; Everhart and Barnwell [54]).

The classical values of *K* are typically obtained by assuming a two-dimensional, inviscid cross flow over a wall with a spanwise-infinite number of identical, infinitely-long longitudinal slots. The Davis and Moore theoretical model [46] for this cross flow assumes a zero-thickness slat, while the Chen and Mears theory [35], as corrected by Barnwell [20], attempts to model the slat thickness. Chen and Mears predictions for *K* are a factor of two larger than those of Davis and Moore. Experiments to determine the value of *K* are difficult to conduct, time consuming, and, typically, have been single point experiments with no variation in wall geometry or test conditions, resulting in an inconsistent evaluation database. Early experimental values of *K* (Chen and Mears [35]); Berndt and Sörensen [26]; Baronti, *et al.* [22]; Binion [28]) are a factor of two to four times larger than the theoretical models, and are parametrically inconsistent in that they were obtained at different test conditions and with various combinations of wall geometries. A comparison of the *K* values obtained by these methods (Barnwell [21]) is summarised in Figure 5.14.

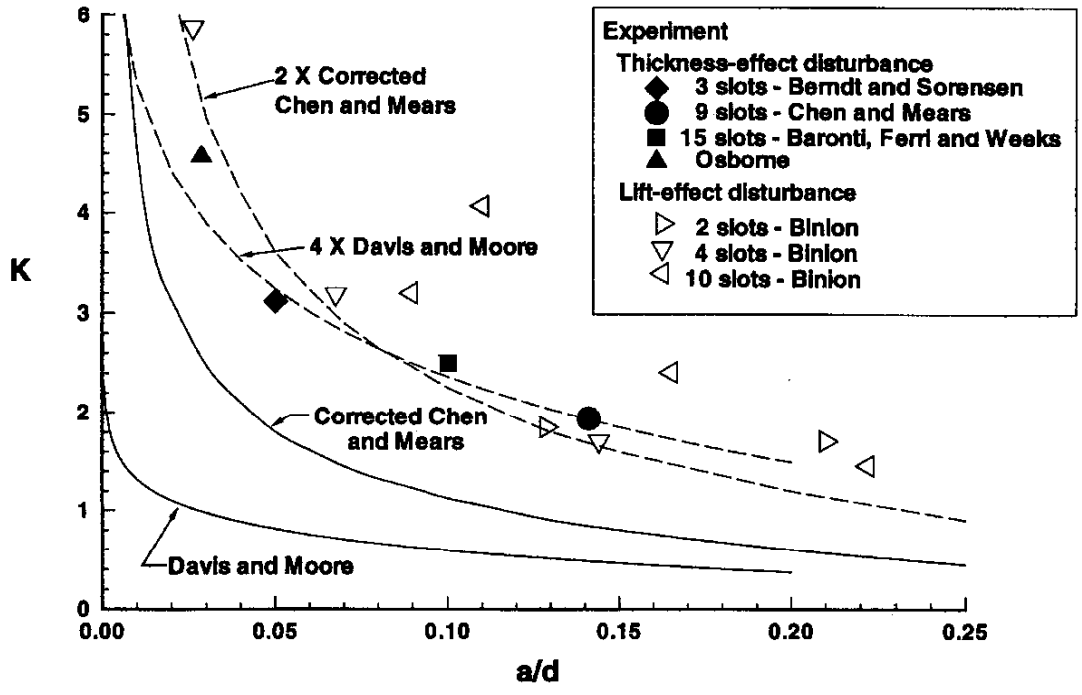

Figure 5.14 : Barnwell correlation for parameter K for slotted-wall boundary condition

5.2.4.3.2 NASA LANGLEY SLOTTED-WALL EXPERIMENTS

An experimental slotted-wall database was developed by Everhart and Barnwell [54], Everhart [53], [58] and Everhart and Bobbitt [55] to resolve some of the coefficient inconsistencies in the slotted-wall boundary condition. The experiments were conducted in the NASA Langley Research Center 6- By 19-Inch Transonic Tunnel (Ladson [112]) using a symmetrical, 6-inch chord NACA 0012 as the reference airfoil model. In these studies, a consistent, two-dimensional database, including (1) pressures measured along three parallel rows of orifices on the tunnel sidewall above and near the slots, (2) limited slot flow angles, and (3) airfoil pressure distributions and lift and moment coefficients was obtained for a parametrically-varied set of slotted-wall geometries and test conditions. The constant-width slot geometries had 1, 2, and 4 slots with openness ratios varying from 3.75 percent to 15 percent. Airfoil model pitch was varied over a range of -4° to 4°, while freestream Mach number was varied from 0.2 to 0.90. Additional, limited, slot flow-angle survey studies were also reported by Everhart, *et al.* [57] and Everhart and Goradia [56] for data acquired in the NASA Langley Diffuser Flow Apparatus (Gentry, *et al.* [70]).

5.2.4.3.3 CORRELATION OF COEFFICIENTS FOR IDEAL SLOTTED-WALL BOUNDARY CONDITION

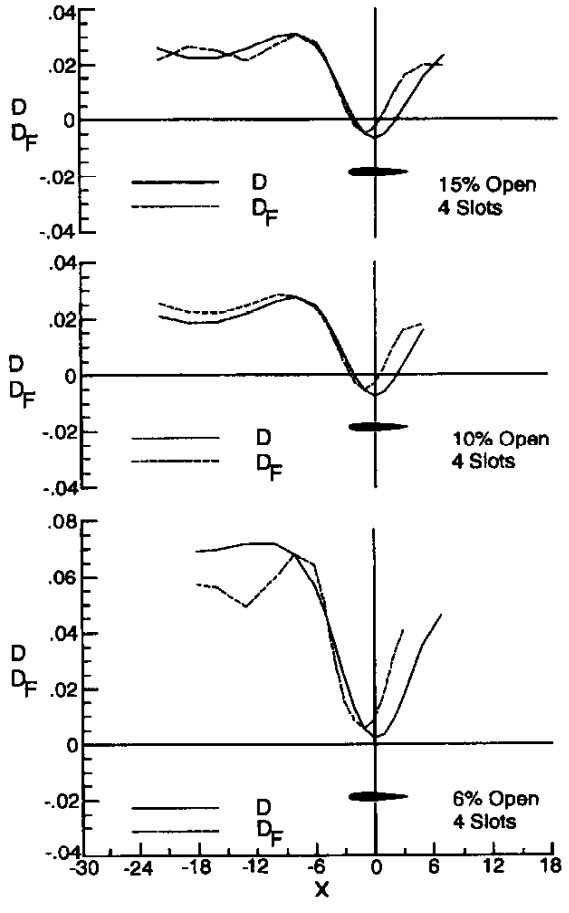

Figure 5.15 : Comparison of ideal form of slotted-wall boundary condition with experiment using 6- by 19 inch Transonic Tunnel data. M=0.7, α=0°.

The Langley slotted-wall database was used to obtain consistent estimates of the *A* and *K* coefficients in the Ideal slotted-wall boundary condition (5-9). Using a two-point evaluation method the *K* coefficient is determined by scaling the streamline-curvature gradient upstream of the maximum thickness point of the airfoil to match the wall-pressure-drop distribution. The *A* coefficient is facility dependent and defined to match the upstream pressure-drop distribution where the streamline curvature is negligible. Comparisons of the measured and computed pressure-drop distributions versus longitudinal tunnel station for several wall openness ratios at Mach 0.70 are shown in Figure 5.15 where the measured (or left) side of equation 5-9 is denoted by *D* and the computed (or right) side of equation 5-9 is denoted by D_F. The pressure-distribution match is generally reasonable upstream of maximum model thickness (minimum pressure). As with the Berndt boundary condition (see Section 5.2.4.2) considerable differences exist downstream of this position where inflow to the test section occurs. Furthermore, the curves are skewed and in no observed case did the computed minimum pressure align with the measured minimum pressure. The *K* coefficients determined for the Ideal boundary condition for all wall geometries are shown in Figure 5.16 for a freestream Mach

number of 0.7. The dashed-line fairings show very consistent variations with both openness ratio and number of slots. The agreement of the one-slot and two-slot results with theory is fortuitous in that these two theories were derived assuming an infinite number of slots of uniform openness. The three-slot results (filled circle) computed using the Berndt and Sörensen [26] data correlate well with the Langley results in that it lies between the two- and four-slot results. The experimental results for 9 slots (filled square, Chen and Mears [35]) and for 15 slots (filled triangle, Baronti, *et al.* [22]) have the right magnitude relative to the Langley four-slot results. Even though the infinite-slot theoretical trends are similar to the experimental results, quantitatively they give *K* values which are much smaller than those for the four-slot configuration when, in fact, they should be larger. On this basis, it would seem that the homogeneous-wall condition is rapidly approached for walls with four or more slots and that a valid, limited use of the Ideal boundary condition can be made for some conditions, as long as an experimentally-determined value of *K* is used.

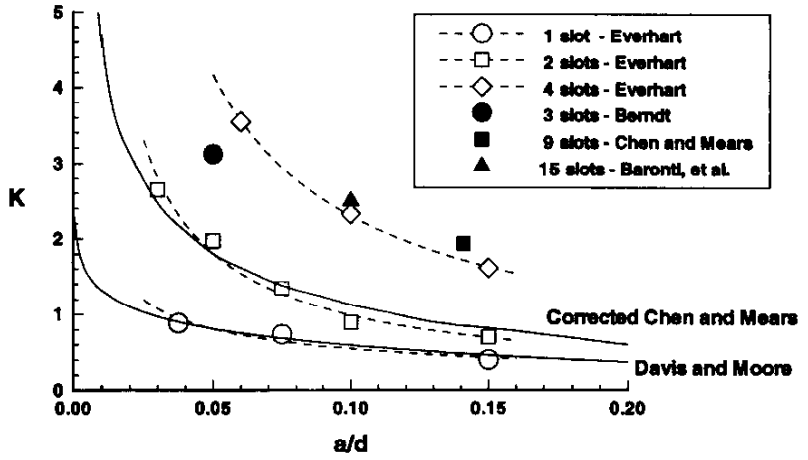

Figure 5.16 : Variation of K with openness ratio for the ideal form of the slotted-wall boundary condition. M=0.7, $\alpha=0^{o}$

5.2.4.3.4 LINEARISATION OF THE SLOTTED-WALL BOUNDARY CONDITION

An experimental and analytical examination of the Langley databases resulted in the boundary condition

$$C_{pw} - C_{ps} = 2dK\frac{\partial \theta_w}{\partial x} + B\theta_s + \theta_s^2 = -dK\frac{\partial C_{pw}}{\partial y} + B\theta_s + \theta_s^2 \qquad (5\text{-}10)$$

which relates the pressure drop across the wall to the streamline curvature near the wall, and to a linear and quadratic variation of the flow angle in the slot. Based on available information, the flow angle in the slot, θ_s, should be taken at the *vena contracta*, where it maximises. The value of C_{pw} is that achieved in the tunnel in the far field of the slot where the flow is unaffected by the local geometry of the slot. The pressure coefficient C_{ps} is the pressure imposed on the slot by the plenum. Equation (5-10) will reduce to

$$C_{pw} - C_{ps} = B\theta_s + \theta_s^2 \qquad (5\text{-}11)$$

for an empty tunnel with no streamline curvature near the wall. For large outflow through the slots, usually caused by the build-up of the tunnel wall boundary layer or by converged walls, the quadratic term dominates and the equation (5-11) will further reduce to

$$C_{pw} - C_{ps} = \theta_s^2 \qquad (5\text{-}12)$$

Limited slot flow measurements obtained by Gardenier and Chew (Goethert [71]), Berndt and Sörensen [26], and Everhart [58] validate equations (5-11) and (5-12). The coefficient *B* is dependent on the details of the slot geometry and the boundary layer growth, and, to date, specific experiments to generate variational correlations have not been conducted.

Equation (5-10) can be linearised as follows. First, subtract equation (5-11) from (5-10), to obtain

$$(C_{pw} - C_{pw,te}) - (C_{ps} - C_{ps,te}) = -dK\frac{\partial C_{pw}}{\partial y} + B(\theta_s - \theta_{s,te}) + (\theta_s^{\,2} - \theta_{s,te}^{\,2}) \tag{5-13}$$

Letting

$$\Delta\theta = \theta_s - \theta_{s,te} \tag{5-14}$$

be the increment between the flow angle in the slot with the model installed and the undisturbed flow angle in the slot in the empty tunnel will yield

$$\theta_s^{\,2} - \theta_{s,te}^{\,2} = 2(\Delta\theta)\theta_{s,te} + (\Delta\theta)^2 \approx 2(\theta_s - \theta_{s,te})\theta_{s,te} = A + B'\theta_s \tag{5-15}$$

if $\Delta\theta$ is small. Implicit in (5-15) is the assumption that $\theta_{s,te}$ is approximately constant in the vicinity of the model (Everhart [58]). Substitution of (5-14) and (5-15) into (5-13) yields

$$(C_{pw} - C_{pw,te}) - (C_{ps} - C_{ps,te}) = A - dK\frac{\partial C_{pw}}{\partial y} + B\theta_s \tag{5-16}$$

where B is a reformulated viscous coefficient. Far upstream, the model-induced streamline curvature is very small and, for large outflow, the B coefficient is negligible. The A coefficient can then be thought of as a measure of the difference between the empty-tunnel plenum pressure and that measured with the model installed at the same freestream Mach number.

Values of the slotted-wall boundary condition coefficients *A*, *K*, and *B* were determined in Everhart [58] from experimental data using the method of least squares. Representative correlations are presented in Section 5.2.4.3.7.

5.2.4.3.5 Effect of Airfoil Model on Plenum Pressure

Many transonic wind tunnels use the plenum pressure as the tunnel reference pressure for calibration and Mach number control. An unstable reference condition exists if the plenum pressure is sensitive to the presence of the model and its test environment. Under these conditions the facility is not operating at the required test conditions, and the resulting aerodynamic data must be corrected accordingly. However, in general, the magnitude of the correction is an unknown because the model effect is unknown. Everhart and Bobbitt [55] quantified this effect for a NACA 0012 airfoil model tested in the NASA Langley 6- By 19-Inch Transonic Tunnel at zero lift by examining the far-field pressure drop coefficient, $\Delta C_{p,ff}$. This coefficient is defined as the plenum pressure coefficient subtracted from the freestream pressure coefficient measured upstream of the slot origin in a location which is undisturbed when the model is present. (This upstream pressure is used to calibrate and operate the wind tunnel.) Pressure drop coefficient results plotted versus wall openness ratio obtained with and without the model installed for a freestream Mach number of 0.7 are presented in Figure 5.17. For matched freestream Mach numbers, the airfoil presence causes the plenum pressure to drop globally relative to the corresponding tunnel-empty case. This effect is present for all slot geometries tested; however, the difference decreases with increasing openness ratio. For openness values greater than 10 percent, the difference in the measurements is small, an indication that the tunnel is approaching open-jet conditions in which the freestream static pressure is equal to that of the surrounding plenum. The fact that the plenum pressure is lower than the average pressure in the tunnel is a result of a jet pumping effect exerted on the plenum by the tunnel. These observations are consistent with other transonic data published by Berndt and Sörensen [26] and, also, at low speed with high model-induced blockage results obtained by Kuenstner,

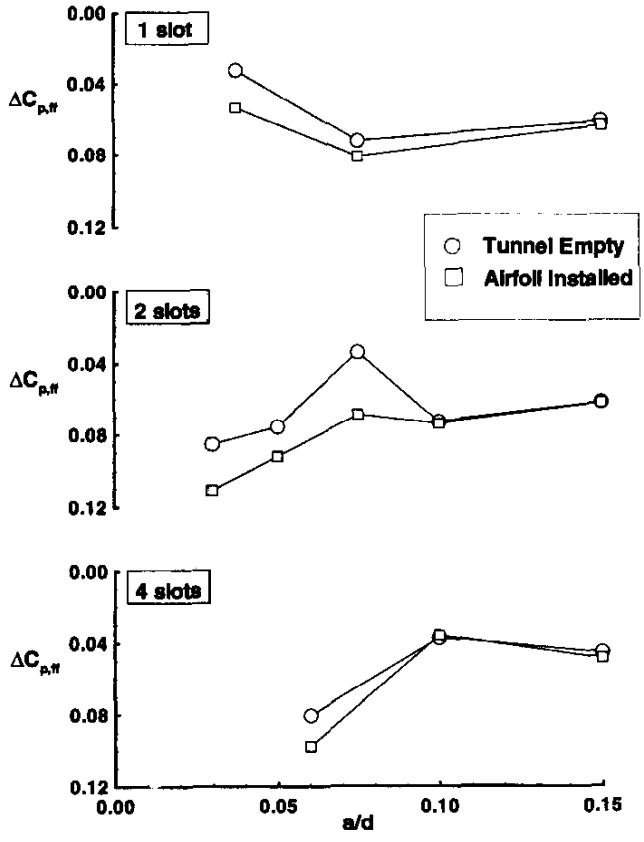

Figure 5.17 : Effect of two-dimensional model on slotted-wall wind tunnel plenum pressure. M=0.7, α=0^{O}

et al. [111] in an open-jet automotive wind tunnel. These results warrant caution when calibrating ventilated wind tunnels, and, particularly, for models tested at high speed or under high loading conditions where the plenum pressure is used as the reference condition.

5.2.4.3.6 Correlation of Boundary Pressure Measurements with Theory

Experimental and mathematical procedures for obtaining best-fit correlations of the unknown coefficients given by equation (5-16), the linearised version of (5-10), are presented in Everhart [58]. The goodness of the agreement is demonstrated in Figure 5.18 by plotting the measured (or left) side of (5-16) defined as

$$D = (C_{pw} - C_{pw,te}) - (C_{ps} - C_{ps,te}) \tag{5-17a}$$

and the fitted (or right) side of (5-16) defined as

$$D_F = A - dK\frac{\partial C_{pw}}{\partial y} + B\theta_s \tag{5-17b}$$

versus longitudinal distance along the slotted wall. The comparisons obtained at Mach 0.70 are for three different four-slot wall configurations for openness ratios of 15-, 10-, and 6-percent. Airfoil incidence is zero degrees. The slots begin at station -23 inch, open linearly to station -19 inch, and extend with constant width to station 19.5 inch. The sharp slope discontinuity in the D_F curve at station 3 inch is the

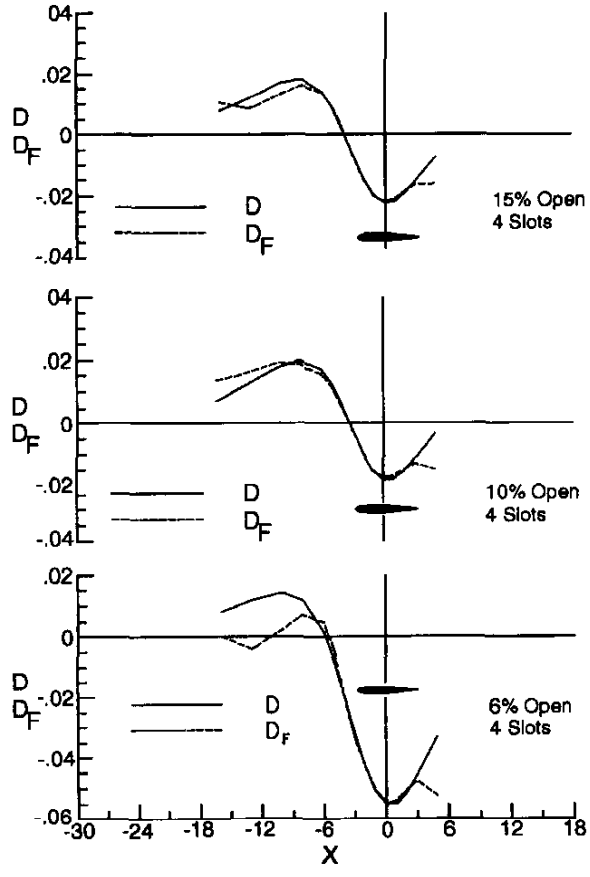

Figure 5.18 : Comparison of Everhart's slotted-wall boundary condition with experiment using 6- by 19-inch Transonic Tunnel data. M=0.7, α=0°.

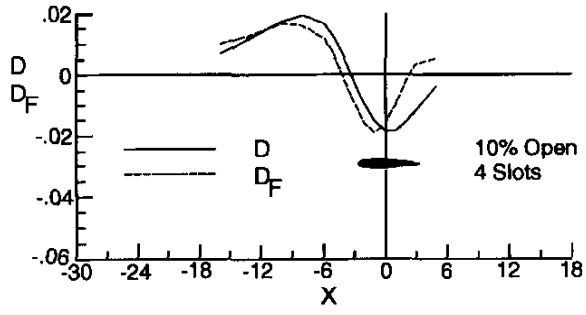

Figure 5.19 : Effect of excluding the linear flow angle contribution from Everhart's form of slotted wall boundary condition. M=0.7, α=0°

result of flow-angle probe support contamination. These same data are used again in Figure 5.19 to, again, demonstrate the effect of excluding the linear contribution of the flow angle. This, in effect, reduces the equation to the Ideal form of the boundary condition given by equation (5-9). In all cases, a mismatch or skewing of the curves exists which can only be removed if the linear contribution to flow angle is retained as previously shown in Figure 5.18.

5.2.4.3.7 Variation of Boundary-Condition Coefficients

Figure 5.20 shows the variation of the *K* coefficient with openness ratio for a freestream Mach number of 0.7 and zero angle-of-attack. The dashed lines are fairings which indicate trends of those walls with the same number of slots. Sufficient information exists to obtain a *K* value from the Berndt and Sörensen [26] data which is shown as the filled symbol. The addition of the $B\theta_s$ term absorbs part of the contribution to wall-pressure drop originally assumed in total by the streamline-curvature term and, as a result, reduces the *K* coefficient values compared to the "ideal" values (see Figure 5.16) determined from equation (5-9). The variation with the number of slots is consistent in that increased values of *K* are obtained with larger numbers of slots. However, the results for three and four slots are very nearly the same which indicates, as expected, that the assumption of a homogeneous boundary condition is more closely modelled by the walls with the larger number of slots.

The corresponding *B* coefficients are also shown in Figure 5.20. The variations of the one- and two-slot results are very similar; however, the results change slope for the walls with four slots. This behaviour is not too surprising since one of the greatest uncertainties is the behaviour of the boundary layer over the slotted wall and how it interacts with the flow through the slot. The larger the number of slots the smaller the ratio of slot width to wall boundary layer displacement thickness, yielding a more uniform variation of

the wall flow-field properties. It is clear, based on these results that a linear flow-angle contribution is required in the boundary condition equation to properly model the pressure drop through a longitudinally-slotted wind-tunnel wall. The actual numerical value of the coefficient must be determined for the given slotted-wall configuration.

The *A* coefficients presented in Figure 5.20 reveal scatter which appears to be related to uncertainty in the flow angle. If *A* is assumed to result exclusively from the decrease in the plenum pressure coefficient due to the presence of the model, then, for this Mach number, an *A* value of 0.02 will yield a Mach number increment of 0.008.

Additional variations with Mach number and model lift may be found in Everhart [53], [58]. In general, the following statements can be made for these test conditions.

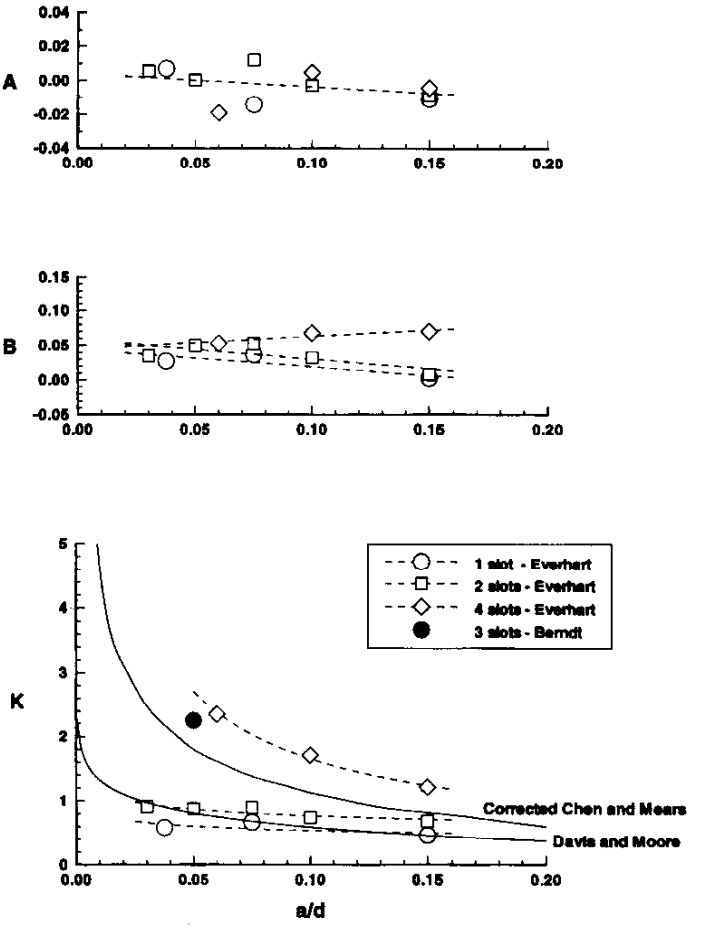

Figure 5.20 : Variation of coefficients with openness ratio for Everhart's form of slotted-wall boundary condition. M=0.7, $\alpha=0^{o}$.

(1) At fixed lift, a regular, monotonic increase in the values of *A*, *K*, and *B* occurred with increasing Mach number; however, it is possible that this effect is the result of viscous narrowing of the slot.

(2) At fixed Mach number, only slight (if any) coefficient variation occurred with changes in lift coefficient.

Because the 6- by 19-inch Transonic Tunnel is an atmospheric wind tunnel, variations in the ratio of wall boundary-layer thickness to slot width are only those which would occur as a result of changing unit Reynolds number by a factor of about 2. Additionally, this variation cannot be made independent of changes in Mach number. As a result, the parametrically-varying effects of slot Reynolds were not independently examined.

5.2.4.3.8 COMPARISON OF COEFFICIENTS WITH BERNDT'S SLOT-DEPTH HYPOTHESIS

Berndt [24] developed a second-order approximation for the *K* coefficient which isolated an effect due to slot depth (see, also, Goethert [71]). His result is expressed as

$$K = -\frac{1}{\pi}\ln\left[\sin\left(\frac{\pi a}{2d}\right)\right] + 0.462 + \frac{t}{a} = K_{DM} + 0.462 + \frac{t}{a} \tag{5-18}$$

where K_{DM} is the theoretical Davis and Moore [46] form of the slotted-wall *K* coefficient for a zero-thickness wall. In 1982 Berndt [25] further proposed highlighting the thickness parameter *t/a* by writing

$$\Delta K = K - K_{DM} = 0.462 + \frac{t}{a} \tag{5-19}$$

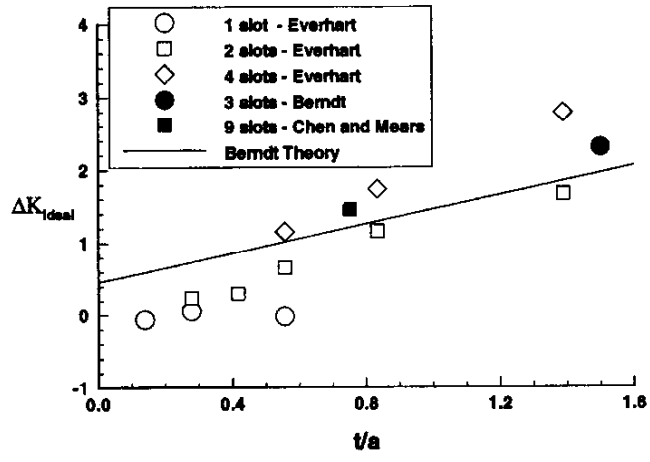

Figure 5.21 : Influence of slot depth on Ideal form of slotted-wall boundary condition efficient K. M=0.7, α=0°.

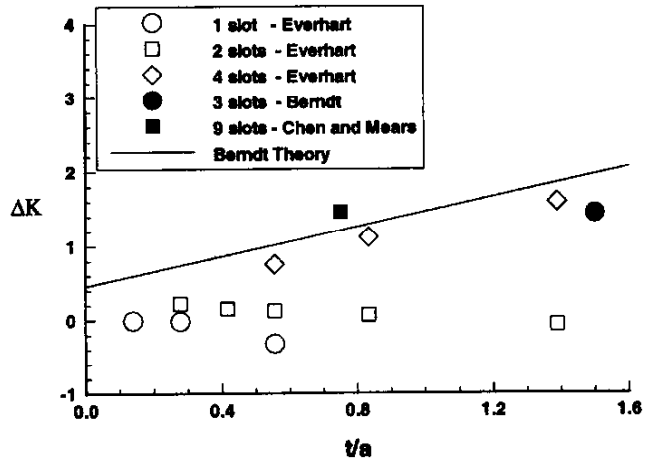

Figure 5.22 : Influence of slot depth on Everhart form of slotted-wall boundary condition coefficient K. M=0.7, α=0°.

Applying this expression to the Ideal boundary-condition values of Figure 5.16 yields the results presented in Figure 5.21. It appears that ΔK values do correlate with slat thickness; however, this trend has a different slope and intercept than that of the theoretical prediction.

Comparable results for the Everhart boundary condition given on Figure 5.20 are shown in Figure 5.22. Based on previous discussions, the one- and two-slot results should not match the theoretical prediction, which is indeed the case as exhibited by their flat distribution with slot depth. The Everhart four-slot, Berndt three-slot, and Chen and Mears nine-slot values closely approximate the Berndt hypothesis of (5-19). These results support the earlier observation that they are close to representing a homogeneous slotted wall (see section 3.2) and lend further credence to the Berndt slot-depth hypothesis as represented by equation (5-19).

5.2.4.3.9 IMPLEMENTING EVERHART'S BOUNDARY CONDITION EQUATION (5-10)

Presently, no known utilisation of equation (5-10) exists in any computational formulation. However, because of its nonlinearity, implementation of equation (5-10) will require iterative numerical procedures similar to the slotted wall boundary condition of Berndt (section 5.2.4.2) and porous wall boundary conditions of MDA (sections 5.2.3.1 and 5.3.1) or the AEDC (sections 5.2.3.2 and 5.3.2).

5.2.4.4 TRANSONIC SLOT DESIGN

5.2.4.4.1 DESIGN METHOD FOR TWO-DIMENSIONAL SLOTTED WALLS

Barnwell [21] developed improved procedures for designing slotted walls for two-dimensional transonic wind tunnels which were then applied to the NASA Langley 6- by 28-Inch Transonic Tunnel and to the 8-inch by 24-inch slotted test section of the 0.3-Meter Transonic Cryogenic Tunnel. The procedure emphasises the maintenance of small disturbances at the wall and small crossflow velocities in the slot which, accordingly, allows the use of the small-disturbance form of the slotted-wall boundary condition given by

$$C_{pw} = 2K\frac{d}{h}\frac{\partial\theta_w}{\partial(x/h)} = 2k\frac{\partial\theta_w}{\partial(x/h)} \quad \text{where} \quad k = K\frac{d}{h}$$

and, where C_{pw} is the ambient pressure coefficient near the tunnel wall, θ_w is the flow angle near the tunnel wall, d is the slot spacing, h is the tunnel semi-height, K is the slotted-wall performance coefficient, and k is the slotted-wall boundary-condition coefficient.

An examination of Pindzola and Lo [151] for ideal slotted-wall tunnels shows that model blockage vanishes at the value k=1.18, that wake blockage at the model is zero, that the gradient in the wake blockage vanishes at zero model blockage, that downwash is nearly constant in the vicinity of the model for zero blockage (it can only be eliminated in a closed tunnel), and, that the streamline curvature vanishes at k=1.58. Therefore, in the classical sense it is obvious that that no single, fixed-wall geometry can eliminate all interference effects, and that compromises in wall geometry must be made. According to linear theory, it can also be shown that the blockage increment at the model position induced by a wake survey rake is negative, and, since blockage interference is positive for closed walls and negative for open walls, it is possible to reduce blockage interference at the model position by controlling the wall openness at the rake position.

With these facts in mind and because computational predictions using classical boundary conditions are significantly different from experiment, Barnwell next examined the variation of K with slotted-wall openness ratio, a/d. A summary of his analysis is presented in Figure 5.14. Theoretical, homogeneous-boundary representations of the slotted wall developed by Davis and Moore [46] for an infinitely thin slotted wall and by Chen and Mears [35], corrected by Barnwell [20], for a wall with finite thickness have functionally different variations for small a/d and yield differences in K which vary by a least a factor of two. Direct experimental measurements of K by Chen and Mears [35], Baronti, *et al.* [22], Berndt and Sörensen [26], and K values inferred from experimental measurements by Osborne [146] and Binion [28] were found to be in disagreement with both theories. An experimental correlation band given by 4 times the Davis and Moore theory and 2 times the corrected Chen and Moore theory bounds the thickness-effect only data. (Experimental values determined later by Everhart [53], [58] also lie within this correlation band (see Figure (5.16)).

The minimum blockage value of K may now be determined for a tunnel of height $2h$ with a specified number of slots (giving the slot spacing, d). The required openness ratio is determined from the correlation which allows the slot width to be specified. For the Langley 6- by 28-Inch Transonic Tunnel, this procedure yields one 6-percent open slot, two 2-percent open slots, or four very narrow slots. Because of the potential for large (possibly sonic) crossflow velocities with a 2-percent-open (or less) wall, a single-slot configuration with a 5-percent open area was selected. Theoretically, this wall geometry creates a slightly positive blockage to cancel the negative blockage imposed by the wake rake and it

reduces the streamline curvature correction. A similar evaluation was made for the 8-inch-wide by 24-inch-high slotted test section of the Langley 0.3-Meter Transonic Cryogenic Tunnel, resulting in a minimum blockage geometry with two 5-percent-open slots each on the top and bottom walls.

5.2.4.4.2 NTF SLOT DESIGN

Slotted-wall design criteria for the National Transonic Facility noted by Newman, *et al.* [143] were

1) zero lift interference with four walls slotted, and
2) smooth Mach number distributions at supersonic test conditions.

The first design criterion was met by extending the two-dimensional procedures described in Section 5.2.4.4.1. The second criterion was satisfied by using the method of Ramaswamy and Cornette [154] to provide a suitable supersonic slot entry region (see Section 5.2.4.4.3). Slightly closing the walls at the model station accounted for the negative blockage effect of the model support. Sidewall slots, though included in the original design, were not installed; however, provisions exist for the installation of 2 such slots in each sidewall. The resulting model region of the NTF test section has 5-percent open transonic walls with six uniformly-spaced slots each on the top and bottom walls, and solid sidewalls.

5.2.4.4.3 SUPERSONIC SLOT DESIGN—METHOD OF RAMASWAMY AND CORNETTE

Methods to design supersonic slotted walls and evaluate supersonic flow in a slotted wall wind tunnel were developed by Ramaswamy and Cornette [154]. Fundamentally, the method of characteristics is combined with a wall boundary condition which relates the local value of the Prandtl-Meyer angle, υ_w, to the local flow angle, θ_w. In analysis mode $(\upsilon - \theta)_w$ is prescribed along characteristics striking the wall. The angle υ_w is determined using the Mach number computed from local wall pressures. By assuming homogenous flow near the wall, large crossflow through the slot, and no streamline curvature, the angle θ_w is obtained from

$$\theta_w = \varepsilon \frac{a}{d} \sqrt{C_{pw}}$$

The slot orifice coefficient, ε, is used to account for the *vena contracta* effect of the crossflow jet and the wall boundary layer effects. Wind tunnel calibration data obtained in the Langley 8-Foot Transonic Pressure Tunnel (Harris, *et al.* [82]) and in the Langley Diffuser Flow Apparatus (Gentry, *et al.* [70]) were used to validate the method, and extremely good correlations between theory and experiment were obtained using slot orifice coefficients in the range of 0.8 to 0.9. In the design method, smooth longitudinal distributions of test section centreline Mach number and $(\upsilon + \theta)_w$ along characteristics leaving the wall are prescribed. Since θ is zero on the tunnel centreline, the value of $\upsilon_w = \upsilon_{cl}$ is determined and, hence, θ_w. The wall pressure drop is obtained from the wall Mach number which, upon specification of an appropriate orifice coefficient, allows the required wall openness ratio, *a/d,* to be determined. To avoid overexpansion and for smooth supersonic flow to exist in the test region, the required distribution of slot openness ratio was found to increase to a maximum and then decrease to zero. However, because the wind tunnel must also operate at transonic speeds, the slot openness is only allowed to decrease to that value required to minimise wall effects at transonic speeds.

5.2.5 BAFFLED SLOTTED WALLS

5.2.5.1 Background

Baffled slotted wind tunnel walls were originally developed for the NASA Ames Research Center 11-Ft. Transonic Tunnel where a full-scale 1981 demonstration of the concept validated its feasibility. Additionally, this geometry was proposed for the recently cancelled NWTC Subsonic and Transonic Wind Tunnels initiative (Sickles and Steinle [170]). Baffled slotted walls are created by filling longitudinal slots with nominally spanwise-oriented baffles. The baffles remove the dependency on streamline curvature, a characteristic of the flow through the more traditional slots, and create strips of porosity described by Darcy's Law for pressure drop through a porous medium. Baffled slotted walls combine several important attributes of porous walls and slotted walls. First, early acoustic studies by Daugherty and Steinle [44], Jacocks [88], and Daugherty, *et. al.* [45] verified that properly-designed baffles were quieter than the uniformly-distributed discrete holes in porous walls. These and other unpublished studies have led to recently-developed methods of reducing ventilated-wall noise to levels comparable with that of a solid wall tunnel (Steinle [175]). Next, good optical accessibility is a must for modern, nonintrusive measurement methods and slots allow significantly improved access compared to porous walls. Finally, supersonic wave attenuation by a porous wall is superior to that offered by a slotted wall. Sickles and Steinle computationally demonstrated good attenuation properties which rapidly approach homogeneity and match porous wall characteristics for eight or more baffled slots (Steinle [175]).

Flow field survey data which characterise the flow over a baffled slotted wall with a segmented plenum chamber were obtained by Wu, *et al.* [187] and by Bhat [27]. These data were obtained for flows into and out of the plenum (i.e. under suction and blowing conditions) and reveal the complex flow character associated with ventilated walls. For flow into the plenum, large streamwise counter-rotating vortices co-exist in the test section along each side of the baffled slot. These vortices were removed with increasing pressure drop (decreasing plenum pressure) across the wall. Conversely, the strength of the vortices was increased with decreasing pressure drop (increasing plenum pressure). For outflow conditions, the test-section-side behaviour of the wall flow field should be similar to that over the slotted wall. Therefore, these data offer insight into the flow behaviour over the more traditional transonic slotted wall geometry. Though not specifically addressed in their reports, the data of Wu, *et al.* [187] and Bhat [27] allow one imagine how flow into the tunnel through both slotted and porous walls could conceivably energise these vortices to the point of ultimately separating them and the tunnel-wall boundary layer from the tunnel wall surface. Obviously, significant viscous-interaction research remains before ventilated tunnel-wall boundary conditions are fully understood.

5.2.5.2 BOUNDARY CONDITION FOR AMES 11-FT TRANSONIC TUNNEL

Unpublished semispan data acquired while testing a large RAE model 864 were used to determine the boundary condition of the baffled slotted walls of the Ames 11-Ft. Transonic Tunnel (Steinle [175]). The basic tunnel geometry has 5.6-percent-open baffled slots on all four walls. For this test, the tunnel floor was sealed and used as the semispan reflection plane while the other three walls were tested in three configurations with (1) completely open slots, (2) completely closed walls, and (3) with the top tunnel wall closed and tunnel sidewall slots open. The model was spanwise instrumented with six longitudinal rows of pressure orifices, and data were acquired over a range of model pitch and freestream Mach number. For the closed-wall tunnel, configuration (2), the spanwise distribution of the angle-of-attack correction was computed by simulating the wing with 10 horseshoe vortices and by using the method of images for

compressible flow. For tunnel configuration (3) (top wall closed), the spanwise angle of attack correction for the baffled slotted wall was determined using the method of Kraft and Lo [108] for a family of resistive values, R, and streamline-curvature coefficients, K, for a freestream Mach number of 0.7. The envelope of these R-K pairs which gave the best overall comparison with the closed-wall results was extrapolated to that corresponding to a uniformly-distributed porous wall. Because the Kraft and Lo theory is for a uniformly-distributed porous wall, dividing the extrapolated resistive value by the baffled-slotted-wall openness ratio will accumulate all resistivity into discrete slots, yielding a resistivity value of approximately 19 for the 11-Ft Tunnel. Results obtained in the Ames 2- by 2-Ft Tunnel by Matyk and Yasunori [127] unsurprisingly gave a significantly different resistivity value due to non-amplification by a much thinner tunnel-wall boundary layer; however, as expected, their results showed a general independence with Mach number due to the low-speed flow through the baffled slot. Calculations of the spanwise variation in lift interference for these data in the 11-Foot tunnel and other case studies are shown in Steinle and Pejack [176]. Additional wall-interference calculations which characterise the baffled-slotted wall are presented by Crites and Steinle [43].

5.3 COMPUTATIONAL APPROACHES

In this section a brief overview of computational or CFD approaches used to simulate transonic wind-tunnel test-section flows is given by means of a few sample numerical implementations and results. This is not intended to be a thorough review of CFD methods or simulations of wind-tunnel flows, all of which have become possible since the publication of AGARDograph 109 [67]. The methods discussed in this section use a wide range of mathematical boundary conditions from the classical-like, where the boundary condition is known and prescribed *a priori*, to the non-linear, where the boundary condition simulating the tunnel-wall flow must be iteratively solved as a part of the entire solution process. Modern boundary measurement methods incorporating near-wall flow data as a boundary condition are also presented. These boundary conditions are used in WIAC techniques which are becoming increasingly attractive as measurement accuracy improves and instrumentation costs per channel rapidly decrease (for example, multi-channel electronically-scanned pressure transducers or pressure-sensitive paint techniques), and as computational power soars and moves to the desktop.

5.3.1 TUNNEL SIMULATIONS

The division of the subsections herein is based upon the flow equation approximation used in the wind-tunnel simulations.

5.3.1.1 LINEAR THEORY

A number of linear theory flow codes have been modified to include homogeneous classical-like wind-tunnel wall boundary conditions on the outer or far-field boundary. Keller and Wright [94] is a sample implementation which includes a variety of such wall conditions. There, they developed a numerical method to examine incompressible boundary-induced interference in rectangular wind tunnels with slotted or perforated walls which Keller [93] later modified and extended to include slot viscous effects. The walls were modelled with source panels on which a general boundary condition of the form

$$c_1\varphi + c_2\frac{\partial\varphi}{\partial x} + c_3\frac{\partial\varphi}{\partial n} + c_4\frac{\partial^2\varphi}{\partial x\partial n} = 0$$

was applied. The coefficients were specified according to the type of tunnel wall and boundary condition being evaluated as specified in the following table:

TYPE OF BOUNDARY CONDITION	c_1	c_2	c_3	c_4
Closed wall	0	0	1	0
Open jet	0	1	0	0
Perforated wall	0	1	$\frac{1}{R}$	0
Ideal slotted wall: integrated form	1	0	K	0
Ideal slotted wall: differentiated form	0	1	$\frac{\partial K}{\partial x}$	K
Slotted wall with viscosity in slots	0	1	$\frac{\partial K}{\partial x}+\frac{1}{R}$	K

Besides presenting a simple method for evaluating interference, the method computationally revealed the very significant effect of viscosity on the wall-induced interference. For a square tunnel with four 6-percent open slots each in the top and bottom walls, the lift interference factor, δ_0, was found to vary from 0.078 to -0.012 as R varied from 0.333 to 3, respectively. Pearcey, *et al.* [148] showed typical values of R of the order of 1.

Other linear theory codes have been modified or developed to model various discrete aspects of wind-tunnel geometry, including the walls. For example, Lee [114] simulated the testing environment of practical 3-D, subsonic, rectangular cross-section wind tunnels using a higher-order panel method. A homogeneous slotted wall boundary condition was used to represent the effects of slot openness in a finite length test section which included corner fillets. In addition, the test model size, shape, location and mounting system were also simulated, thus, providing both a diagnostic tool for interpreting experimental data as well as a design tool for the test environment. As another example, Kemp [103], [96], [97], developed STIPAN, a high-order panel code which simulates a slotted wind tunnel test section with discrete, finite-length wall slots subject to plenum chamber constraints and terminated by a re-entry region to smooth the flow transition to the solid wall diffuser. Both non-linear effects of the dynamic pressure of the slot outflow jet and of the low energy of the slot inflow are considered; the test model and sting support are also represented. These simulation features were selected to be those appropriate for the subsequent intended use of this simulation in a wall interference assessment and correction (WIAC) procedure, PANCOR, using a modified wall model making use of sparsely located wall pressure measurements (Kemp [98],[95]). Figures 5.23 and 5.24, taken from this latter reference, illustrates the STIPAN/PANCOR slotted-wall model. Simulation results demonstrated that accounting for the discrete slots is important in interpreting wall pressures measured between the slots, and that accounting for non-linear slot flow effects produces significant changes in tunnel-induced velocity distributions; in particular, a longitudinal component of tunnel-induced velocity due to model lift is produced. A characteristic mode of tunnel flow interaction with constraints imposed by the plenum chamber and diffuser entrance is apparent in the results.

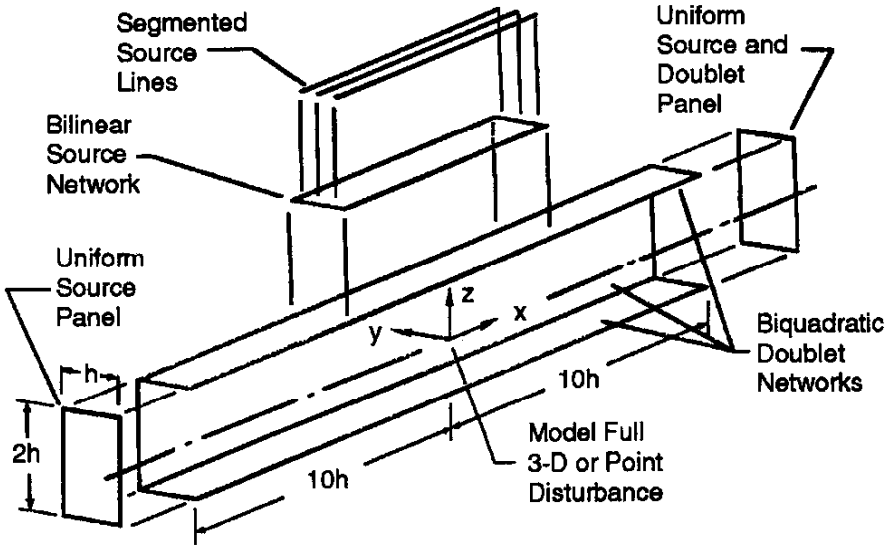

Figure 5.23 : STIPAN/PANCOR slotted wall model
Singularities used on tunnel flow domain

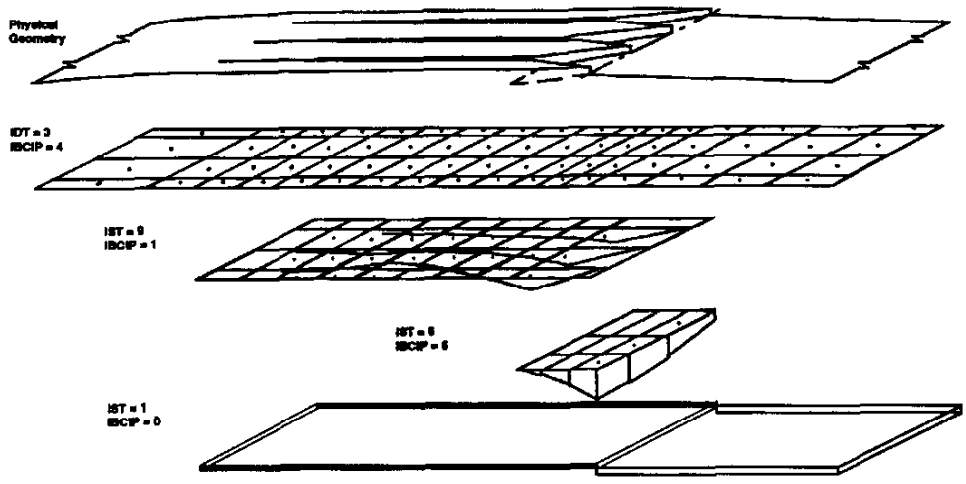

Figure 5.24 : STIPAN/PANCOR slotted wall model.
Panel network superposition used to represent a slotted tunnel wall

5.3.1.2 Transonic Small Disturbance Equation (TSDE) Methods

The non-linear TSDE considered here is generally of the form

$$(1-M^2)\phi_{xx}+\phi_{yy}+\phi_{zz}=0$$

where M is the local Mach number and ϕ is the small disturbance perturbation velocity potential. Various approximations are made to calculate M, but all contain at least one non-linear term of the form $A\phi_x\phi_{xx}$. Axisymmetric, slender lifting body, and 2-D versions of the TSDE all retain this term while appropriately dropping others. However, more non-linear terms and those involving cross-derivatives must be added to adequately approximate swept shock waves on swept wings.

The advent of practical transonic computational fluid dynamic calculations around 1970 (Murman and Cole [136]) allowed one to perform numerical experiments related to tunnel-wall effects. General conclusions were: (1) somewhere in the transonic regime linear superposition does break down (Murman [135]) and (2) wall characteristics can be very non-linear at transonic conditions (Kacprzynski [90]) and dependent upon the model pressure field through its influence on the wall boundary layers, especially those on the mounting walls in 2-D airfoil and semi-span wing tests, as mentioned in section 5.2.2. The latter two references were early discussions of 2-D (airfoil) TSDE applications utilising ventilated wall boundary conditions; Murman, *et al.* [134] discusses the TSFOIL code resulting from Murman's earlier work.

Early TSDE results for circular tunnel geometries were presented for axisymmetric bodies by Bailey [15] and for slender lifting wing-body combinations by Barnwell [17]. Simulations have also been used in conjunction with deriving/assessing approximate ventilated wall boundary conditions. A series of papers by Karlsson and Sedin [91], [92], [164], [165], discussed in section 5.2.4.2, used an axisymmetric TSDE in assessing various slotted tunnel wall boundary condition approximations.

Extension to TSDE simulation of a 3-D wing in a rectangular cross-section wind tunnel with rather arbitrary boundary conditions was presented by Newman and Klunker [140]. The boundary condition used to model the tunnel walls was the integrated form of the generalised linear homogeneous condition as given by Keller [93] and discussed in section 5.3.1.1. However, an inhomogeneous term must be

added to account for integration constants; it also accounts for physical effects such as non-zero C_p in the plenum or contoured walls. This condition is:

$$A\phi_n + B\phi_x + C\phi + D = 0$$

Conventional linear wall conditions are obtained as

Open jet	A=C=D=0	B≠0
Straight solid	B=C=D=0	A≠0
Contoured solid	B=C=0	-D/A = wall slope
Porous	C=D=0	B/A = porosity or restriction parameter
Slotted	B=D=0	C/A = slot geometry parameter

Also note that the addition of a term $E\phi_{xx}$ would allow one to model the Adcock and Barnwell [2] approximation of viscous effects on solid tunnel walls as discussed in Section 5.2.2.

As pointed out by Newman and Klunker [140], "Several points should be made concerning the tunnel-wall boundary condition. First, it is considered to be an average relationship between various local inviscid flow properties which applies near the wall rather than on it. Second, in an iterative finite-difference calculation there is a great deal of flexibility regarding the form of the boundary condition itself since (a) it need not even have a functional form (i.e., could be measured flow properties) much less be linear; (b) the parameters in it can vary with local tunnel geometry or local flow conditions; and (c) it is restricted, however, in that the relaxation calculation must be stable. Third, the porosity and slot geometry parameters must be determined experimentally." However, "these parameters are dependent on local flow conditions near the tunnel wall which for transonic flows are influenced not only by the tunnel operating conditions but also by the test configuration." Nevertheless, they concluded that "the results for tunnel-wall modelling demonstrate that various conventional tunnel-wall boundary conditions can be incorporated in numerical computations. Such modelling should be useful in assessing interference effects and as an aid in the design of wind tunnels." These 3-D TSDE calculations for a wing in a simulated NTF tunnel indicated a need for some sidewall relief. The two slots incorporated in each sidewall design provide this relief and are compatible with the mechanical and optical requirements on the NTF test section.

Indeed, later uses of the 3-D TSDE in approximate boundary condition and ventilated wall design assessment, as well as for wall interference prediction have been reported by others. For example, Sedin, *et al.* [163] and Agrell, *et al.* [6], [7] used it for slotted wall studies as discussed in Section 5.2.4.2. Phillips and Waggoner [149], [150] implemented the classical boundary condition formulations in a nonconservative, transonic small disturbance code (Boppe [30]). The boundary conditions (including solid walls, open jets, porous and slotted walls, and solid and slotted walls with viscous effects) were applied independently on the different tunnel walls to obtain a pre-test estimate of wall interference effects on the aerodynamic test data. Comparisons between predictions and measured reference data (Lockman and Seegmiller [116]) revealed discrepancies in wing shock locations of about 5 percent. These discrepancies were attributable to the numerical differences in nonconservative versus conservative finite difference formulations and other not-modelled details of the shock-wave/boundary-layer interaction. Al-Saadi [8], [9], [10] computed the transonic flow over two different transport configurations tested in the National Transonic Facility using a nonconservative, transonic small disturbance code in which several, usually-neglected, higher-order terms were retained to improve shock-wave and wing-sweep simulations (Boppe [30]). Tunnel-wall boundaries were modelled using the Berndt discrete-slot boundary condition

and comparisons with measured wall pressures were used to assess the quality of the simulation. Though good comparisons were generated for some cases, uncertainties in the wall pressure measurements and in the viscous boundary-condition modelling require a more detailed analysis to be performed when appropriate data become available, particularly at the higher Reynolds numbers where good data are non-existent.

5.3.1.3 FULL-POTENTIAL EQUATION (FPE) METHODS

For steady, inviscid, irrotational flow ($\nabla \times V = 0$), a velocity potential ϕ can be defined ($V = \nabla\phi$) which satisfies the non-linear FPE, written here in Cartesian co-ordinates as

$$\left(a^2 - \phi_x\phi_x\right)\phi_{xx} + \left(a^2 - \phi_y\phi_y\right)\phi_{yy} + \left(a^2 - \phi_z\phi_z\right)\phi_{zz} - 2\left(\phi_x\phi_y\phi_{xy} + \phi_y\phi_z\phi_{yz} + \phi_z\phi_x\phi_{xz}\right) = 0$$

where a is the speed of sound which depends on the velocity components ϕ_x, ϕ_y, and ϕ_z. However, unlike the TSDE, this FPE equation (or its equivalent for a stream function) is generally solved in a "body-oriented" or mapped co-ordinate system in order to obtain sufficient resolution and near orthogonality in high gradient and curvature regions of the flow. Thus, a non-trivial issue for simulation of tunnel flows using a structured grid is to find an appropriate simultaneous mapping for both test model and tunnel walls. This should be no problem, however, for an unstructured grid approach.

The classic transonic relaxation solutions obtained by Emmons [50] were for an airfoil (the NACA 0012) in a solid wall wind tunnel and in free-air. It is interesting to note that he stated then:

"Theoretical predictions of the effect of wind-tunnel walls for incompressible fluids have been successful with the required accuracy. For increasing Mach numbers, however, the corrections increase very rapidly and have a very profound effect on the flow as shock waves appear. Thus, the best experimental method in aerodynamics is seriously handicapped by the lack of knowledge of what wind-tunnel-wall corrections should be made to wind-tunnel test results."

He concluded:

"Although the relaxation method appears to be adequate to solve the very involved differential equations and boundary conditions describing the flow of a compressible fluid, the calculations are too involved to permit the investigation of a very wide range of interesting cases without the use of high-speed calculating machines."

His calculations were done by hand; it would be another twenty-five years before such high-speed calculations would even be demonstrated!

In 1975, transonic flow solutions obtained by relaxation of the FPE for both 2-D and axisymmetric models inside wind tunnel walls appeared. Kacprzynski [90] presented results for an airfoil in a porous wind tunnel with non-linear wall behaviour. He mapped the region exterior to the airfoil, including the walls, into the interior of a circle and found the solution method to be extremely efficient numerically. However, he concluded that the inclusion of viscous effects would require costly updating of the mapping function. Another analysis of this problem is given by Catherall [32] for flow past airfoils in solid, porous or slotted wind tunnels. South and Keller [172] considered transonic flow past axisymmetric bodies in a wind tunnel where the region between the body and tunnel wall is mapped onto a rectangular plane. A general linearised homogeneous wall boundary condition, essentially that given and discussed in Section 5.3.1.2, was enforced to model solid, open-jet, and idealised porous and slotted walls. They addressed the computational mapping, numerical implementation of boundary conditions, stability, and convergence

issues for the FPE in such applications. Results were also presented for nonlifting 2-D tunnel flow simulations.

In the early 1980's FPE applications related to simulating wind tunnel flows for 2-D, axisymmetric, and 3-D configurations continued to address the required co-ordinate mappings. Doria and South [48] developed a nearly orthogonal mesh by a sequence of Schwarz-Christoffel transformations and shearings appropriate to 2-D lifting airfoils and axisymmetric bodies in a wind tunnel. The finite-volume relaxation process was investigated using several different iterative schemes; solution convergence of nearly choked channels was found to be slower than that for other transonic flows. Mercer, *et al.* [128] and Mercer and Murman [129] developed a fully-conservative, finite-volume FPE computer program to simulate transonic flow past a swept wing in a wind tunnel with specified normal flow at the walls. They obtained an approximately orthogonal mesh conforming to both the wing and the tunnel walls. This code was intended to simulate the wind tunnel in preliminary studies of 3-D adaptive wall concepts; some 2-D airfoil example calculations, used in the code verification, were given and a 3-D sample result was demonstrated.

5.3.1.4 Euler Equation Methods

The Euler equations express the conservation of mass, momentum and energy for inviscid rotational flow and are written in 3-D Cartesian co-ordinates (x_i), with corresponding velocity components (u_i), as

$$\frac{\partial w}{\partial t} + \sum_i \frac{\partial f_i(w)}{\partial x_i} = 0$$

The vectors w and f_i are functions of the velocities (u_i), pressure (p), density (ρ), total energy (E), and total enthalpy (H) given by

$$w = \begin{bmatrix} \rho \\ \rho u_1 \\ \rho u_2 \\ \rho u_3 \\ \rho E \end{bmatrix} \quad \text{and} \quad f_i = \begin{bmatrix} \rho u_i \\ \rho u_1 u_i + p\delta_{1i} \\ \rho u_2 u_i + p\delta_{2i} \\ \rho u_3 u_i + p\delta_{3i} \\ \rho H u_i \end{bmatrix}$$

where $p = (\gamma - 1)\rho\left[E - \frac{1}{2}\sum_i u_i^2\right]$, $\rho H = \rho E + p$, and $\delta_{ij} = 1$ for $i=j$, 0 otherwise.

The early numerical solutions of these equations were also generally done in body-fitted co-ordinates; i.e., on mapped structured grids, similar to those used for FPE solutions, or on embedded grids (Benek, *et al.* [23]) and first for 2-D airfoils. An interesting example by Gaffney, *et al.* [66], who solved the Euler equations on Cartesian co-ordinates for a multielement airfoil, pointed out the more serious problem associated with inviscid CFD solutions for realistic configurations tested in wind tunnels at supercritical Mach numbers. They conclude that their

"calculations...illustrate the importance of taking into consideration wall interference effects when comparing the predictions of theory with experiment. With the exceptions of regions where viscous-inviscid" interactions "are strong," (i.e., regions at trailing edge of main airfoil and leading edge of flap) "calculations based on the Euler equations, when coupled with wall corrections, based on shifts in Mach number" (i.e., the Sewall [166] sidewall boundary-layer contribution discussed in 5.2.2) "and angle of

attack" (i.e., data of Stanewsky and Thibert [173]) "yield remarkable agreement with experiment. However, without proper considerations of viscous-inviscid interactions, simple shifts of angle of attack and Mach number will not bring the predictions of free air calculations in line with those of wind tunnel measurements."

Many uses of 3-D Euler equation CFD solvers in supercritical or transonic wind tunnel applications have been made in the last decade; however, either the configuration or test results tend to be proprietary or sensitive, so that information has not been openly reported. Applications are also mentioned in sections 5.3.2, 5.3.3, and 5.3.4 so little more than a few generalities will be mentioned here. For complex configurations, the body-fitted grids used are block-structured, embedded, or unstructured. These equations are frequently coupled with an approximate boundary layer solver to account for some of the viscous interactions. Tunnel wall boundary conditions, if used, are generally still modelled, due to the flow complexities at the ventilated walls that are required for transonic testing. However, the inability of the Euler equations to properly capture important viscous-inviscid interactions tends to limit their use.

5.3.1.5 NAVIER STOKES EQUATION METHODS

The specific form of the terms in a compressible, turbulent Navier-Stokes equation set depends upon the velocity decomposition and averaging, as well as the turbulence modelling that is used (see, for example, Vandromme and Haminh [179] or Wilcox [184]). In the transonic and high-speed flows of interest here, typically those for aerospace configurations as tested in wind tunnels, both compressible and pressure-gradient effects are important for the shock-wave/boundary-layer interactions which occur. Usually, a thin-layer approximation of the Reynolds' Averaged Navier-Stokes (RANS) equations, written in body-oriented co-ordinates, is employed in the numerical codes. Turbulence modelling utilised over the last decade or so has been primarily algebraic or for one- or two-equation models. Since it is not our purpose to discuss the elaborate equations nor details here, the reader is referred to the cited literature for such information.

Some times, the verification or validation studies for RANS algorithms and turbulence models is attempted by comparing and/or correlating code predictions with measured data on simple configurations where the wind tunnel walls must be considered. The early 3-D study reported by Kordulla [106] is an example; it illustrates the magnitude of the complexities, both experimental and computational, involved in a seemingly simple case. There, results from six different RANS codes, all using the Baldwin-Lomax algebraic turbulence model, were compared with transonic (supercritical) data on a swept semi-span wing mounted on a splitter plate in a solid wall wind tunnel. The tunnel wall interference effects were noted in the pressure distributions, streamline patterns, and integrated forces. However, there were also noticeable effects due to variations in transition location, juncture region modelling, inviscid-viscous wall boundary conditions, and computational gridding. This was for a solid tunnel wall case; the detailed resolution required for a direct simulation of the viscous flow at the ventilated walls normally used in transonic testing is not now feasible. Therefore, one must resort to approximate wall boundary conditions or descriptions as discussed in section 5.2. Use of two perforated wall boundary conditions with Navier-Stokes codes for tunnel flow simulation is indicated in 5.3.2 and 5.3.3.

Simulation of the shock-wave/boundary-layer interactions at the sidewalls in airfoil tunnels and on the mounting wall in semispan wing tests using RANS codes has been done. For example, airfoil tunnel simulations using 3-D codes with viscous sidewall boundary conditions were reported by Obayashi and Kuwahara [145], Swanson, *et al.* [177], and Radespiel [153]. Their results show the loss of 2-D symmetry due to the sidewall boundary layer separation upon its interaction with the shock on the model.

Simulation of the mounting wall viscous layer in a semispan wing test was reported, for example, by Vatsa and Wedan [180]. It is seen that the mounting wall boundary layer interacts with the shock on the model and separates, thus altering the shock strength and position, the streamline pattern, and the separation over an appreciable part of the model span. Milholen and Chokani [130] used a RANS code to calculate the interaction between a wind tunnel sidewall boundary layer and the transonic flow at flight Reynolds number about a thin, low-aspect-ratio wing mounted on that wall. The sidewall boundary layer was seen to have a strong influence on the flow about the wing; the computed wing pressures were in excellent agreement with the data, showing vast improvement over previous free-air computations.

As with the Euler equation CFD codes, applications of the RANS codes are being made to design wind tunnel tests and aid in the interpretation of test results (again, see 5.3.3). As the computational power (speed, memory, and communication bandwidth) of the computer hardware available at the engineer's desk and tunnel continues to increase, so too will the computational fidelity of his computer software. Of the computational gains made in CFD, about half can be attributed to hardware improvements, with the other half coming from algorithm improvements. When Garner, *et al.* [67] was published, CFD did not exist.

5.3.2 MDA Wall Interference Computations

5.3.2.1 Background

Although McDonnell Douglas Aerospace (MDA), currently part of the Boeing Company, tests its advanced fighter configurations in wind tunnel facilities around the world, they own and operate a small 4-foot *x* 4-foot tunnel. This tunnel is very busy with advanced design, missile, and diagnostic tests. The MDA approach to correcting transonic wind tunnel data for wall interference has been strongly influenced by the need to provide viable wall corrections for this small facility — often with oversized models designed to test in a larger tunnel. Furthermore, the need to provide timely corrections for "production" mode testing has resulted in a pragmatic (if not always rigorous) approach that has been demonstrated to provide good quality corrections quickly and economically for many different advanced fighter configurations. A typical "large" model for which validated corrections have been provided would be a 6% F-18 in the 4x4 foot test section.

Two types of corrections can be provided, depending on model size and allowable uncertainty in results. The most economical is an empirical approach obtained from an experimental wall interference database developed by testing a set of four geometrically similar models of different scale in several different size wind tunnels. The more rigorous (and more expensive) method uses numerical simulation of the model in the wind tunnel and in free flight -- taking the difference between the two solutions as an incremental correction for the wind tunnel data. ***The key to the success of this approach is the fidelity of the tunnel wall boundary conditions.***

These two approaches will be briefly described. The development of the wall boundary condition was previously described in section 5.2.3.1. A more complete discussion may be found in the literature.

5.3.2.2 EMPIRICAL CORRECTIONS

As previously noted, the empirical approach was developed from an experimental wall interference database. A set of four models was used to generate this database. In determining the basic design of the "boundary interference" models, the need for simplicity and accuracy in fabrication was balanced against the desire to have a realistic flight configuration. In the end, a simple cylindrical body with a delta wing was used. An ellipsoidal nose was faired into the body at the wing apex location, and a boat tail was added to reduce drag. A NACA 0006 wing section was used, with thickness scaled according to local chord.

A total of four geometrically similar models where constructed, two for use in each facility. Model #2 was sized to have the same relative blockage in the 4x4 foot Poly Sonic Wind Tunnel facility (PSWT) as a typical flight configuration model. Relative blockage is defined here as the maximum cross-sectional area of the model at zero degrees angle of attack, divided by the cross-sectional area of the wind tunnel test section. Model #1 has a relative blockage twice as great as model #2. The smaller two models were designed to significantly exceed standard rules of thumb for model sizing, when tested in the 1x1 foot Transonic Wind Tunnel facility (TWT). Figure 5.25 shows dimensions for the configuration based on reference chord length and the value of reference chord length for each of the four models.

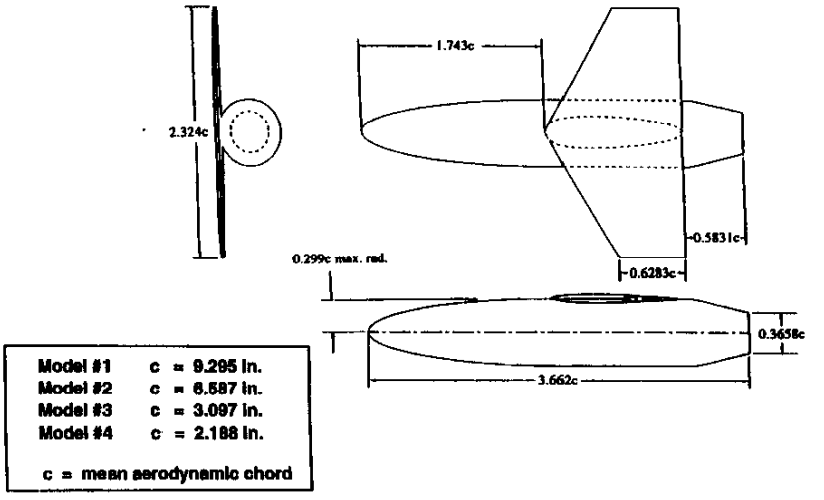

Figure 5.25 : Interference Model Set Dimensions

The models were designed for use with an internal six component strain gage balance. The larger two models (models #1 and #2) use a 1.5 inch diameter balance, while models #3 and #4 use a 0.75 inch diameter balance. Each balance had a separate sting support. Boundary layer transition strips were placed on the nose and both wing surfaces at approximately the 5% chord. Four base pressure taps were provided on the largest two models, on the other models the base area was negligible. As a cost saving measure, no additional pressure instrumentation was provided on any of the four models.

Models #1 and #2 were tested in the PSWT. Models #3 and #4 were tested in both the TWT and PSWT. In addition, data were obtained for model #1 in the Ames 11 ft. Transonic Tunnel. Figure 5.26 shows a summary of the 4 models

$$\text{Blockage} = \frac{\text{Model Reference Area}}{\text{Tunnel Cross-Section}}$$

	Model #1	Model #2	Model #3	Model #4
NASA Ames (11ft. x 11 ft.)	.01108	-	-	-
MDA PSWT (4 ft. x 4 ft.)	.08381	.04191	.009306	.004651
MDA TWT (1 ft. x 1 ft.)	-	-	.1489	.07442

Figure 5.26 : Interference Model Tests

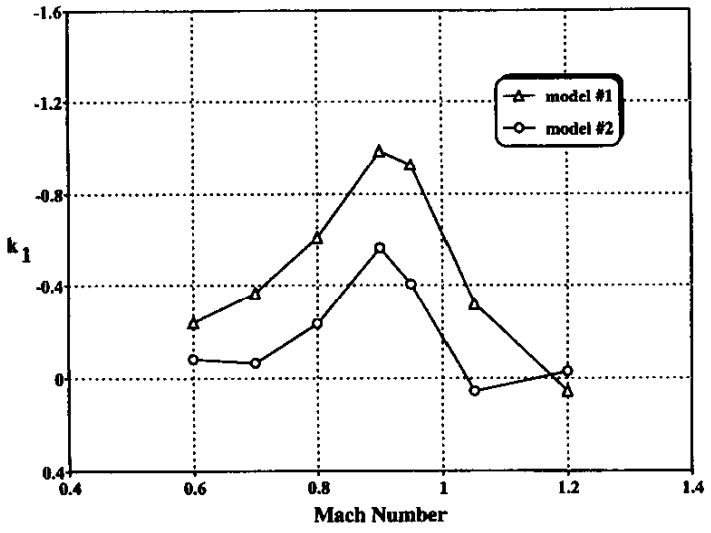

Figure 5-27 : Angle of Attack Interference factor in PSWT

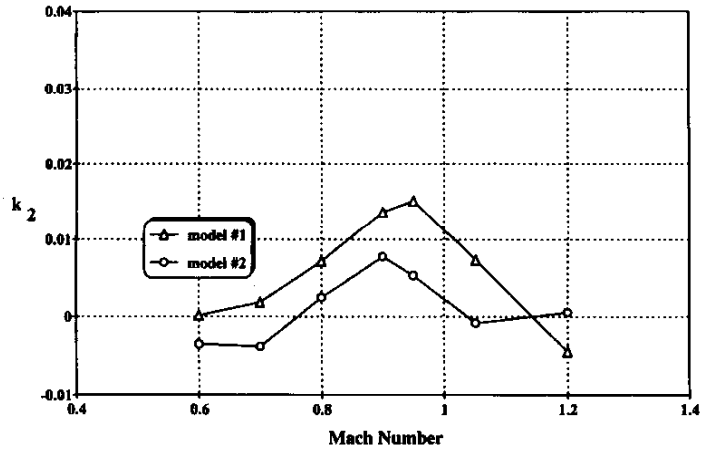

Figure 5.28 : Induced Drag Interference Factor in PSWT

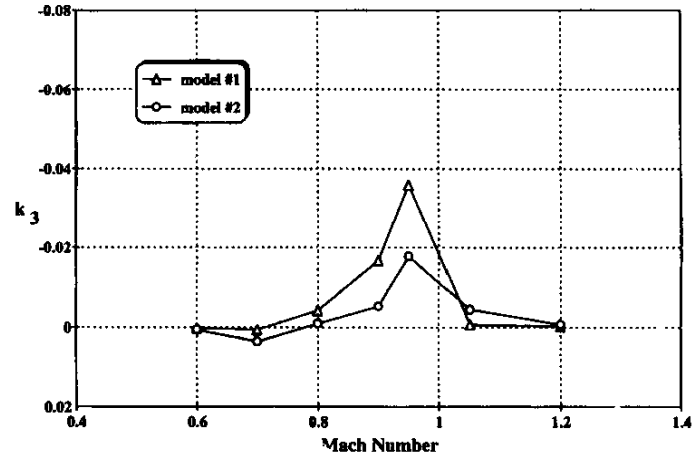

Figure 5.29 : Pitching Moment Interference Factor in PWST

with relative blockages in each facility where they were tested. An overview of experimental results and discussion of treatment of the data to remove Reynolds number effects is given in Rueger and Crites [160].

After examination of the extensive database created by testing these models over a period of two years, it was determined that a relatively simple form was suitable for expressing first order interference induced increments. From Rueger, *et al.* [161]

$$\Delta\alpha = k_1 C_L$$

$$\Delta C_D = k_2 C_L^2 + \frac{\Delta\alpha}{57.3} C_L$$

$$\Delta C_M = k_3 C_L$$

The constants k_1, k_2, k_3 are termed interference factors and are determined by curve fitting interference increments from the database. It should be noted that these expressions are not unique. Other forms may be equally valid.

Figures 5.27, 5.28, and 5.29 show typical variation in wall interference for the two largest models in the set for the 4-foot PSWT tunnel. Note that the interference effect increases sharply (as expected) in the vicinity of Mach 1, and then decreases toward zero as Mach 1.2 is approached.

First order corrections are obtained quickly and simply by scaling the experimental interference by appropriate factors such as reference area, tail length, etc. This gives good first order corrections. Where greater accuracy is required, the interference factors are computed at a couple of points and then curve fit, using the method defined below.

5.3.2.3 Two Points of View

In transonic wind tunnels with relatively small models, a linear wall boundary condition is usually assumed. The wall interference question is: What angle-of-attack and Mach number would be required for the same model in free-flight to develop the same lift measured in the wind tunnel? Corrections are sought for Mach number and angle-of-attack. This approach is a descendant of the method of images (Pope [152]) used to obtain wall interference corrections for low speed solid wall, or open jet, test sections. Extension of this approach to ventilated transonic test sections in Pindzola and Lo [151] and Rizk and Murman [159] naturally retained the initial point of view; i.e., wall interference is seen as an error in Mach number and angle-of-attack. As previously mentioned in Section 5.1.1, a sufficient condition for this approach is WS. However, some of the concepts can be formalised within the framework of asymptotic expansions for Group 1 and possibly Group 2 and 3 flows. The application to Group 1 flows is given in Section 5.4.

In tunnels with relatively large models, the classical approach often fails for two reasons. First, the model is closer to the wall, interactions are stronger, and significant interference gradients develop about the model. In this case there is no single value of Mach number and angle-of-attack that is equivalent to the free-flight condition for the measured forces. The condition is said to be "uncorrectable". Second, the linear wall boundary condition usually used in this type of analysis breaks down and does not apply.

In tunnels with small models, the model-impressed pressure signature is weak at the wall. Also, the boundary layer thickness tends to establish a relatively constant distribution over the walls. In this case, the assumption that crossflow is governed by local wall pressure may be warranted. However, in smaller tunnels the wall signature becomes significant, and, as shown by Jacocks [88], the local crossflow through the wall depends on local pressure and on local boundary layer displacement thickness. Local displacement thickness is strongly dependent on the upstream distribution of pressure and crossflow (transpiration). Therefore, crossflow is really a complex non-linear phenomenon depending not just on the local pressure (classical assumption), but also on the local boundary layer, and therefore on upstream pressure and crossflow distributions. In smaller tunnels (or large tunnels with very large models) the true non-linear nature of the crossflow and boundary layer displacement effect must be considered.

An alternate point of view discards the paradigm that wall interference should be viewed as error in test Mach number and pitch angle. Instead of considering the lift developed on the model as invariant, the test conditions of Mach number and model incidence angle are taken as constant. The question asked is: If the walls (and model support) are removed while maintaining constant Mach number and angle-of-attack, how will the forces developed on the model (pressure distribution over the model) change? From this point of view, interference gradients about the model are automatically taken into account.

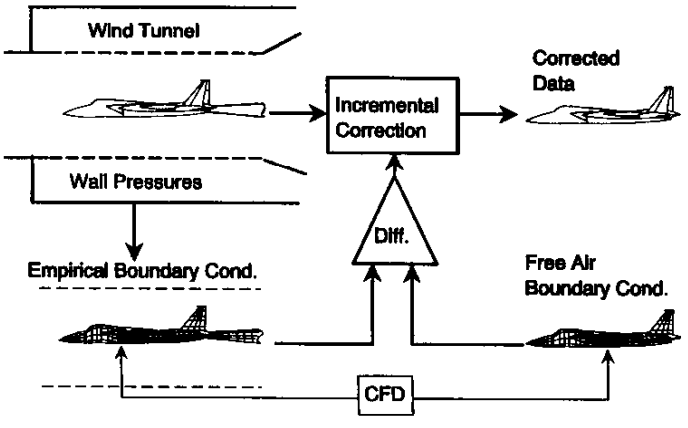

Figure 5.30 : Boundary Interference Correction Method

As shown in Figure 5.30, the correction procedure involves three steps. First, an appropriate numerical flow solver is used to simulate the aircraft model, model support structure, and wind tunnel walls. Measured wall pressures are used

with an empirical procedure to compute the equivalent inviscid boundary conditions simulating the non-linear viscous wall interaction. Second, numerical solutions are obtained with the walls and model support removed (free-flight boundary conditions). Third, the incremental differences in the computed forces and moments are applied to the experimental data as a correction.

5.3.2.4 Application of the MDA Wall Flow Model

The wall flow model of Section 5.2.3.1.4 has been used successfully with flow solvers ranging from panel codes to Navier-Stokes codes. For Mach numbers producing only weak shocks, high order panel codes or full potential methods are useful. For higher Mach numbers, Euler solvers are required. Figure 5.31 shows typical application of the wall flow model. Generally three or four iterations of the wall flow model, separated by a few hundred solver iterations is adequate. Figures 5.32, 5.33, and 5.34, compare computed interference factors using panel and Euler solvers with the empirical interference factors discussed in Section 5.2.3.2. Figures 5.35 and 5.36 show typical corrections of PSWT data for MCM (a super cruise variant), and a 6% scale F-18. The MCM was tested in the PSWT (4x4-foot tunnel) and the NASA Ames 11-Ft Transonic Tunnel. The F-18 was tested in the PSWT and the NASA Langley 7x10-Ft Transonic Tunnel. The PSWT wall, with 22.5% porosity produces open-jet type interference effects. The corrections applied make a considerable improvement.

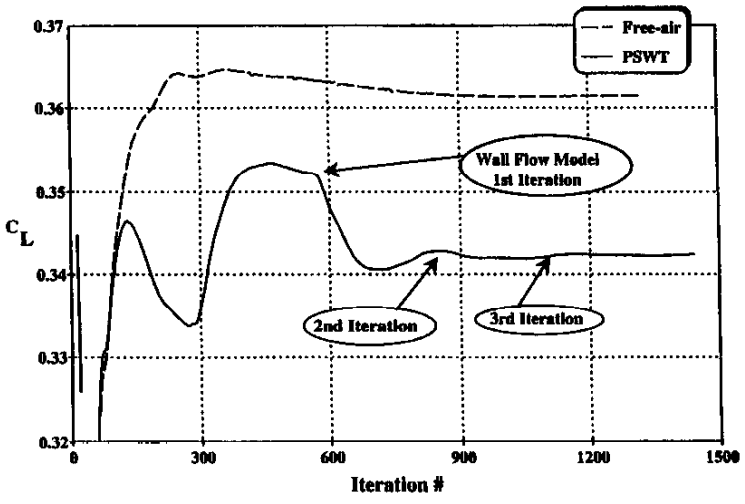

Figure 5.31 : Lift Iteration History

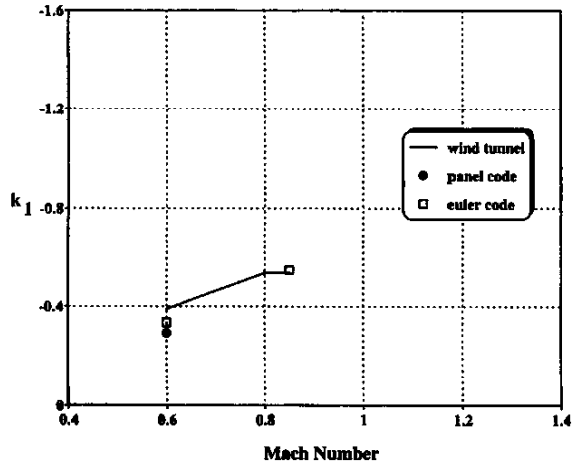

Figure 5.32 : Angle of Attack Interference Factor in the PSWT

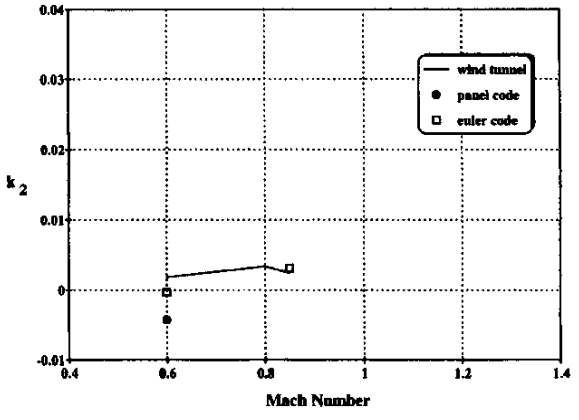

Figure 5.33 : Induced Drag Interference Factor in the PSWT

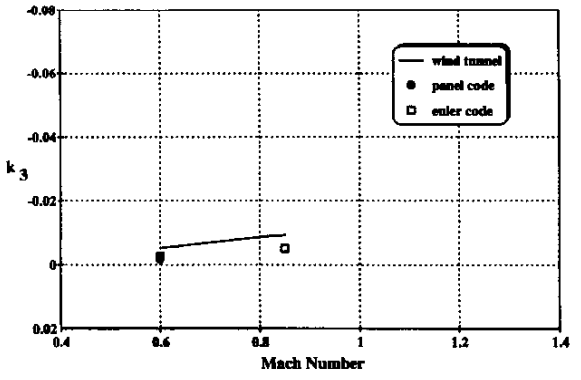

Figure 5.34 : Pitching Moment Correction Factor in the PSWT

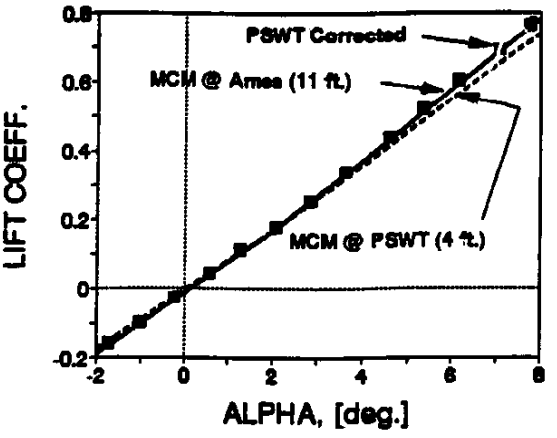

Figure 5.35 : Correction of MCM Lift

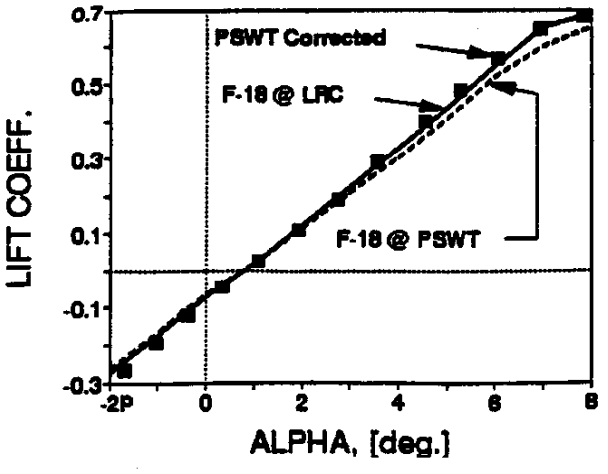

Figure 5.36 : Correction of F-18 Lift

5.3.3 AEDC Wall Interference Computations

5.3.3.1 Introduction

The development of present and future flight systems is placing stringent demands on wind-tunnel facilities to provide high-quality data at transonic speeds. Wall interference can significantly compromise the quality of transonic wind-tunnel data (Whoric and Hobbs [183]). While the perforated walls of AEDC transonic wind tunnels minimise wall-interference effects, significant wall interference can occur at high-subsonic and low-supersonic flow conditions even for models below one-percent solid-blockage ratio (Kraft, *et al.* [109]). In order to use wind-tunnel data to predict a flight vehicle's performance with confidence, the data must be assessed and/or corrected for wall effects. Wall interference is more pronounced and more difficult to correct at high-subsonic conditions where the sonic regions extend to

the walls. Such flows have been classified as Group 2 flows in Hornung [86] and Erickson [51], whereas Group 1 flows have lower Mach numbers with subcritical flows at the walls.

Model sizing is becoming a critical issue in testing. Users want larger models to achieve maximum possible Reynolds number. In the past, models for aerodynamic testing were sized to span less than sixty percent of the tunnel width and to be less than one-percent solid-blockage ratio. Although wall interference can compromise data at certain conditions for these size models, wall interference was not considered to significantly affect the data quality, and corrections for wall interference were not routinely applied. With more stringent data-quality requirements and the desire to test larger models, this assumption is no longer the case. At present no capability exists to routinely correct transonic data for wall interference. As will be shown, corrections are performed only for limited programs and only for limited flow conditions using computationally-intensive CFD techniques.

Several wall-interference assessment/correction (WIAC) techniques have been developed for three-dimensional non-linear flows and are summarised in Kraft, *et al.* [109]. A WIAC technique uses boundary data measured at an interface which is on or near the wind tunnel walls and consists of two components: (1) a flow solver that adequately represents the tunnel and free-air flows, and (2) a procedure for using the measured boundary data and the flow solver to determine wall interference. Although these techniques have been demonstrated numerically for Group 2 flows, there is a considerable need to validate them with experimental data (Kraft, *et al.* [109]). The examples in this contribution address that need.

Wall-interference corrections can also be obtained by pretest-predictive techniques. Application of these techniques requires a representation of the wall behaviour instead of measured boundary data. Classical global descriptions of the ventilated-wall boundary characteristics have proved to be inadequate. AEDC has developed a local semi-empirical description of the perforated-wall characteristic (Sec. 5.2.3.2). Provided that an adequate model of the ventilated walls can be achieved, the pretest procedure is an attractive alternative because it does not require the installation of a measurement system.

Application of WIAC and pretest-predictive techniques to experimental three-dimensional subsonic and transonic data were evaluated in Sickles and Erickson [167],[168]. Use of inviscid flow solvers gave accurate wall-interference corrections for subsonic and mildly supercritical Group 1 flows ($M \leq 0.8$). However, erroneous corrections were obtained for strongly supercritical Group 2 flows ($M \geq 0.9$). In most cases, the sign and magnitude of the lift increment were in error. The cause of the inaccuracies was attributed to the inability of the inviscid flow solvers to simulate the viscous effects on the model. Viscous effects become important for strongly supercritical flow, namely proper shock characterisation and trailing-edge behaviour, and must be represented in order to determine accurate corrections.

5.3.3.2 Wall Interference Procedure

Wall-interference effects are predicted by taking the difference between two CFD analyses. The first is a free-air flow-field calculation, while the second is a tunnel flow-field calculation which includes either a perforated-wall boundary condition for the pretest-predictive approach or a boundary condition where the measured pressure is specified for the WIAC approach. Thus, a pair of calculations must be performed for each test condition under investigation. The difference in calculated local pressures can then be used to correct the experimental pressure measurements. Also, the experimentally measured force and moment can be corrected by appropriately integrating the computed pressure differences and adding the integrated values to the measured data.

This procedure is an incremental approach that looks at the difference between two calculations. Therefore, exact replication of the experimental results with computations is not necessary, but rather the increments must be accurately simulated. However, previous investigation has shown that to obtain accurate increments certain attributes of the flow, such as shock position and strength, must be replicated with some degree of certainty. The sections that follow illustrate the AEDC approach and give results for research configurations as well as realistic test articles.

5.3.3.3 Wall Interference Results

Wall-interference assessment and corrections are given for four models. All models were tested in AEDC wind tunnels which employ perforated walls with sixty-degree inclined holes. The database for each model, except for the Space Shuttle Launch Vehicle (SSLV), consists of data obtained on the same model in a larger tunnel where conditions are assumed to be interference-free. For the SSLV, data exists for a smaller scale model in the same tunnel and in a different tunnel. All models are pressure-instrumented to make detailed comparisons of pressure distributions between data with and without interference. Details of these configurations as well as the wall-interference computations can be found in Martin, et. al., [126] and Sickles, *et al.* [167], [168], [169].

5.3.3.4 Model Descriptions

The first two models are similar. They are generic wing/body/tail vertically-symmetric configurations with constant chord, 30-degree swept lifting surfaces. The first model is shown in Figure 5.37. The lifting surfaces have NACA 0012 cross sections. The model was tested in AEDC Aerodynamic Wind Tunnel (4T), in which the blockage ratio is 0.16 percent, to obtain reference data assumed to be interference-free. Data with varying amounts of wall interference were measured in the adaptive-wall test section of AEDC Aerodynamic Wind Tunnel (1T) (Erickson [51]; Martin, *et al.* [126]; and, Sickles and Sinclair [169]), in which the blockage ratio is 2.5 percent. This model will be referred to as the WIM1T (wall interference model for 1T). The pressure distribution was measured near the tunnel walls with a system of rotated static pipes shown in Fig. 5.38. The second generic configuration, to be referred to as WIM4T, is shown in Fig. 5.39. This model was tested in Tunnel 4T with a blockage ratio of 1.33 %, and in Aeropropulsion Wind Tunnel (16T) for reference data assumed to be interference-free, since the blockage ratio is 0.08%. The lifting surfaces have NACA 0010.4 sections.

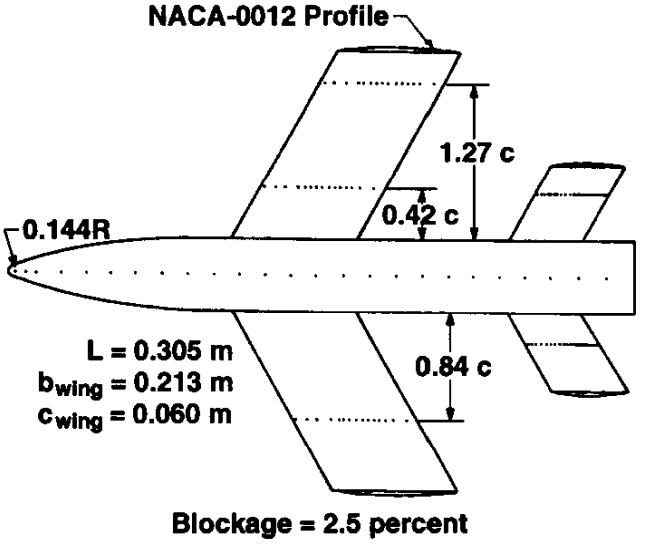

Figure 5.37 : Wall interference model for tunnel 1T (WIM1T)

The third model is a three-percent model of the Space Shuttle Launch Vehicle (SSLV) which is shown in Fig. 5.40. This model was tested twice in 16T. The blockage of this model at angle of attack α = -5°, is 0.7 %. The second entry involved a refurbished, modified

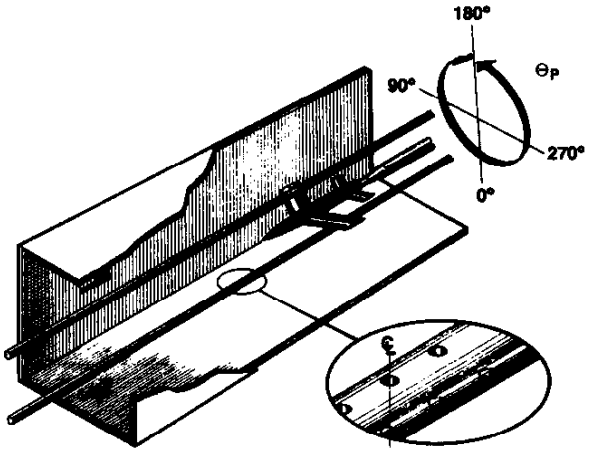

Figure 5.38 : Tunnel 1T interface measuring system

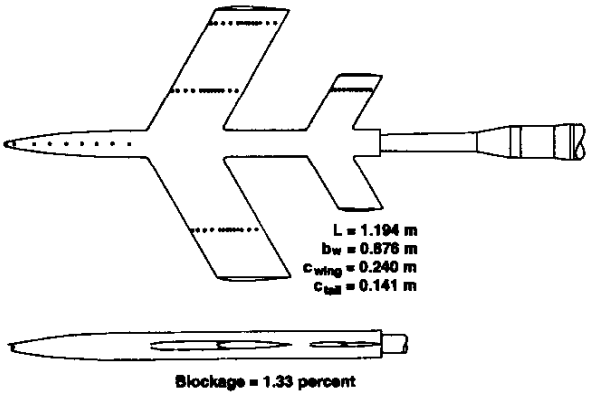

Figure 5.39 : Wall interference model for Tunnel 4T (WIM4T)

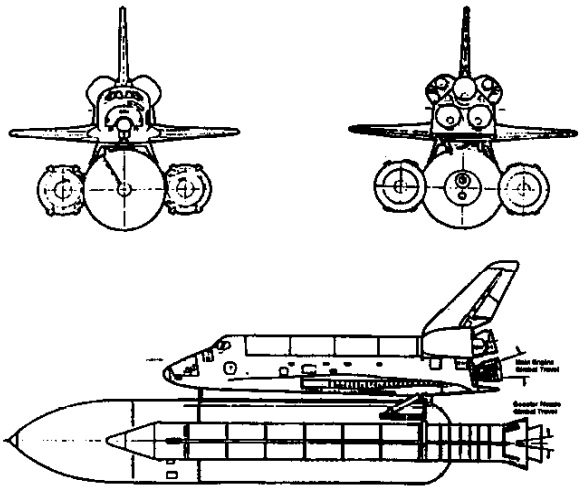

Figure 5.40 : Space shuttle launch vehicle model

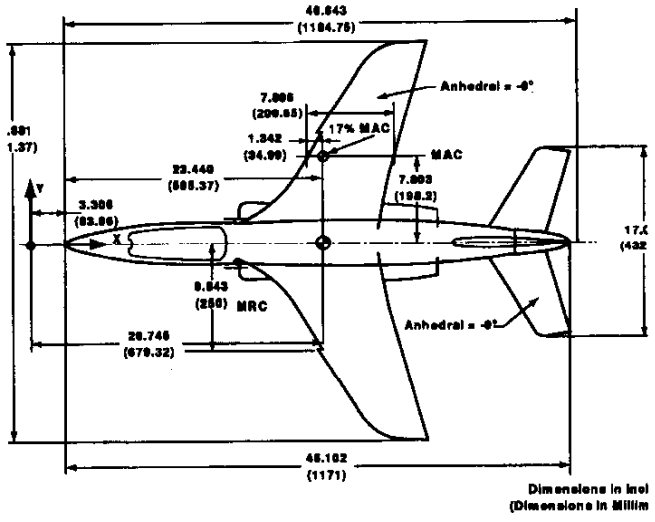

Figure 5.41 TST model schematic

configuration of the first model. A smaller scale model (two-percent scale with a different support system) was also tested and will be used as reference data. The blockage of this model is 0.3% at α = -5°.

The fourth model is the TST model, a 1/10-scale model of the Dornier Alpha Jet configured with a transonic technology wing, and is shown is Fig. 5.41. Tests were conducted in 1992 in Tunnels 4T and 16T as part of a co-operative effort between the United States Air Force (USAF) and the German Ministry of Education and Science, Research and Technology (BMBF). Additional test were conducted in the DLR Kryo Kanal Köln (KKK) and the NASA Langley National Transonic Facility (NTF). Data were obtained over a wide range of chord Reynolds numbers that included conditions from conventional wind tunnels to flight. The objective of the test program was to develop a quality database for studying the interaction of tunnel-environment, wall-interference, and Reynolds-number effects that prevent wind tunnel data from being totally representative of flight, and to confirm the Viscous Simulation Methodology developed by AGARD Working Group 09. The primary objective of the 4T test was to study wall interference and to evaluate the AEDC correction procedures.

The TST model is large for 4T (solid blockage ratio of 1.8%) and significant wall interference was anticipated, particularly at the higher subsonic freestream Mach numbers. Although the TST model is a large model for an aerodynamics test, it is considered a typical size model for Captive Trajectory Support (CTS) testing. To determine the effects of wall interference, the 4T data are compared to the 16T data. The TST model is an extremely small model in 16T (0.1% blockage), and the data from 16T is considered interference-free.

Flow-field pressure measurements were made in 4T during the testing of the TST model to aid in understanding the data and to assist in the validation of the wall interference correction techniques. These pressure measurements were made on a circular interface near the tunnel walls with a series of two-component static pipes that ran nearly the entire length of the test section. Figure 5.42 shows the cross sectional view of the twelve pipe system. The diameter of the interface is 20.5 inches. Six pipes were instrumented with pressure orifices. The other six were dummy pipes that were installed to maintain flow symmetry. Each metric pipe was instrumented with 46 diametrically opposed orifice pairs, except the lower wall metric pipe which had 44 pairs, and two upstream unpaired orifices on the model side of the pipe. The orifices are aligned in the radial direction.

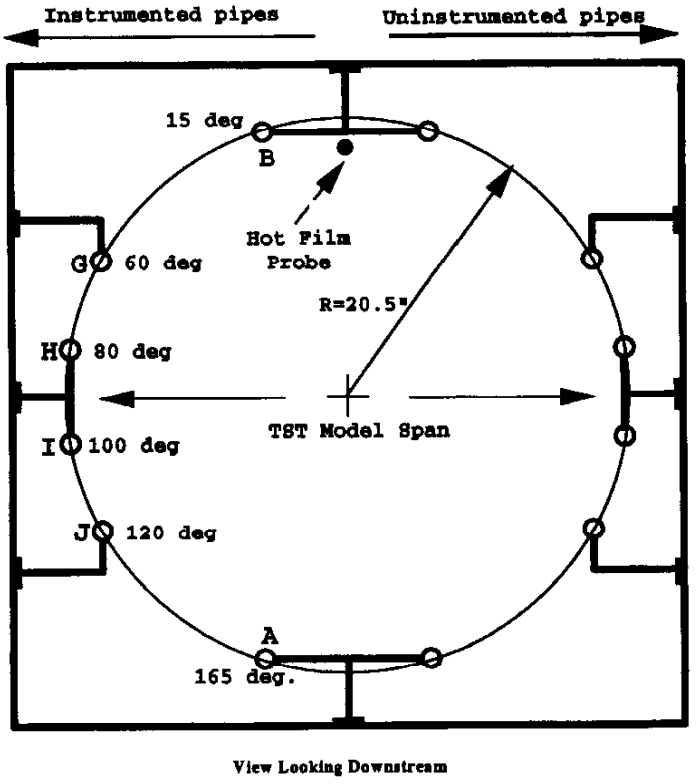

Figure 5.42 : Tunnel 4T static pipe layout for TST test

5.3.3.5 WIM1T AND WIM4T WALL-INTERFERENCE COMPUTATIONS

All flow computations for the WIM1T and WIM4T were performed with the chimera overset-grid code, XAIR (Benek, *et al.* [23]). The near-field about the wings was solved with the thin-layer Navier-Stokes (TNS) equations using a Baldwin-Lomax turbulence model. The fuselage, tail, and far field regions were all solved using the Euler equations. Previous results from Sickles and Erickson [167] showed that the viscous effects must be simulated at high subsonic freestream conditions to achieve accurate wall interference estimates. Both the AEDC perforated-wall boundary condition and a pressure boundary condition were incorporated into the flow solver to perform pretest-predictive and WIAC approaches, respectively.

Comparisons of the WIM1T calculated and measured wing-pressure distributions are given in Figure 5.43 for the WIAC approach and in Figure 5.44 for the pretest approach. The results were obtained for a $M = 0.9$. The Tunnel 1T wall porosity τ was set to three percent open area. Excellent fidelity exists between the calculated free-air and the 4T reference data as well as the calculated tunnel and the 1T

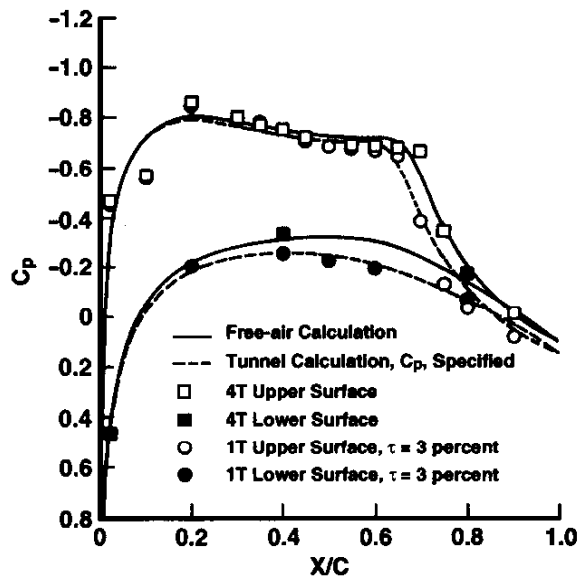

Figure 5.43 : WIM1T model pressures measured and calculated using the WIAC-TNS code at 40-% wing semispan, M = 0,9, α = 4 deg, τ = 3 percent

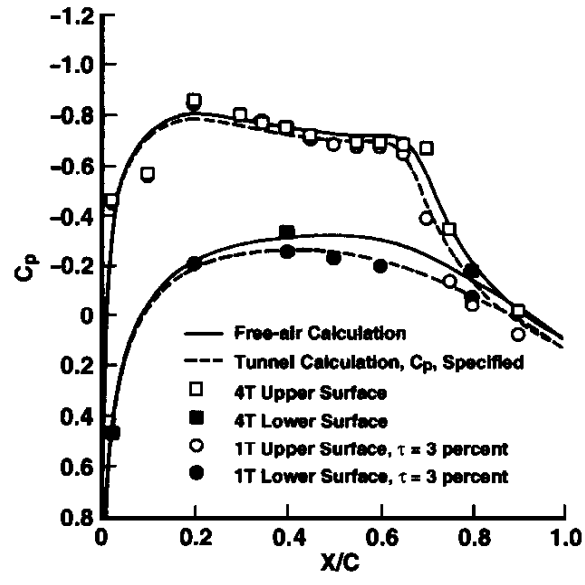

Figure 5.44 : WIM1T model pressures measured and calculated using the Pretest-TNS code at 40-% wing semispan, M = 0,9, α = 4 deg, τ = 3 percent

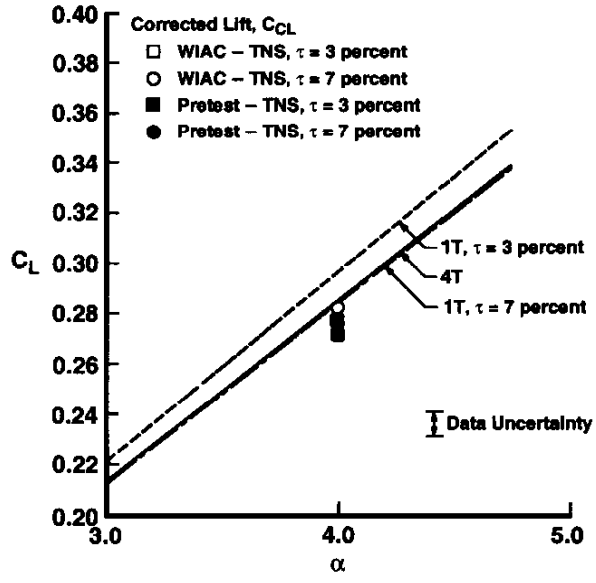

Figure 5.45 : WIM1T corrected lift coefficients using the WIAC-TNS and Pretest-TNS codes, M = 0.9, α = 4 deg

data in the sense that the tunnel calculations with AEDC boundary condition are comparable to the tunnel calculation with measured pressure data prescribed as the boundary conditions. However, the shock is located farther aft on the wing in the tunnel calculations using the AEDC boundary conditions. The difference in shock location tends to amplify in the outboard wing direction (not shown). A comparison between the corrected lift coefficients for the WIAC and pretest codes is shown in Figure 5.45 for the three-percent porosity case and seven-percent case. The pretest corrections for both the $\tau = 3\%$ and the $\tau = 7\%$ cases are larger in magnitude than the WIAC by 0.0057. The larger correction is approximately two percent of the experimental lift, which is smaller than the uncertainty, and is attributable to the aforementioned shock location difference in the calculated pretest wing-pressure distributions. The small differences shown are consistent with the corrections discussed later in Section 5.4.7 and the studies depicted in Figure 5.67. This can be related to the extended validity of slender body theory at transonic Mach numbers when "not-so-slender shapes" look "slender" because of the dominant effect of lateral disturbances along the Mach lines that are almost normal to the freestream, an observation that has been validated by Adams and Sears [1] and others.

The AEDC wall-boundary condition can be evaluated by comparing the calculated and measured distributions at the interface. For most azimuthal locations Θ_p, the calculations using the AEDC

boundary condition does remarkably well at duplicating the measured pressure distributions. A representative comparison is shown is Fig. 5.46 for $\tau = 3\%$ at the azimuthal location $\Theta_P = 85°$ (to the side and below the wing tip). However, the calculated pressure distributions slightly underpredict the measured distribution in the vicinity of the wing. The underprediction is likely caused by the inability of the AEDC boundary condition to represent the behaviour of the walls in the region of strong gradients produced by the close proximity of the wingtip. Also, the underprediction could explain the wing shock location difference and its amplification at the outboard wing station in the pretest calculations. The interface pressures at $\Theta_P = 95°$ indicate that the sonic region extends through the interface near the side wall. Thus, this case can be classified as a Group 2 flow.

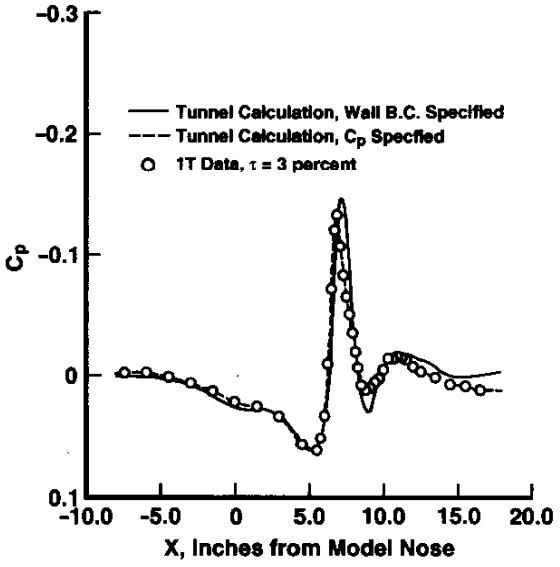

Figure 5.46 : WIM1T interface pressures measured and calculated, M = 0,9, τ = 3 percent.

The pretest approach has been applied to obtain corrections for the WIM4T data at $M = 0.95$ and $\tau = 5\%$ for three angles of attack. Pressures measured near the wall indicate that these cases are clearly Group 2 flows. The sonic region is larger than the WIM1T cases presented and extends to the upper as well as the side walls. Drag corrections for these cases are shown in Figure 5.47. Applying corrections to the Tunnel 4T data gives results that are in very good agreement with the Tunnel 16T reference data. Similar results have been determined for the corrected lift and pitching moment. The drag, lift, and pitching moment errors attributable to wall interference at $\alpha = 4°$ are 11, 4 and 33% of their reference values, respectively, and are all corrected accurately. The uncertainties in the force measurements are approximately the size of the symbol in the graphs.

From another perspective, the results in Figure 5.47 show that the interference is practically constant with angle of attack α to within the data uncertainties. The figure suggests that this interference is simply the zero-lift blockage. This is consistent with the insensitivity of $C_{L\alpha}$ to small, but practical, changes in α, tunnel size and porosity, shown earlier in connection with the WIM1T in Figure 5.45 as well the TsAGI T-128 experiments described in Malmuth, Neyland and Neyland [124] and Section 5.4.9. It can simplify estimating interference effects on drag polars with approximations such as

$$\frac{\Delta C_D}{C_L^2} \sim 1/C_{L_\alpha} .$$

$$\Delta C_D \cong C_D - D_{D_0}$$

For these cases, the major interference effect is the change in zero-lift wave drag which alters C_{D_0}. This can be calculated for many practical shapes such as compact drag-rise fighters and blended wing-bodies from the Transonic Area

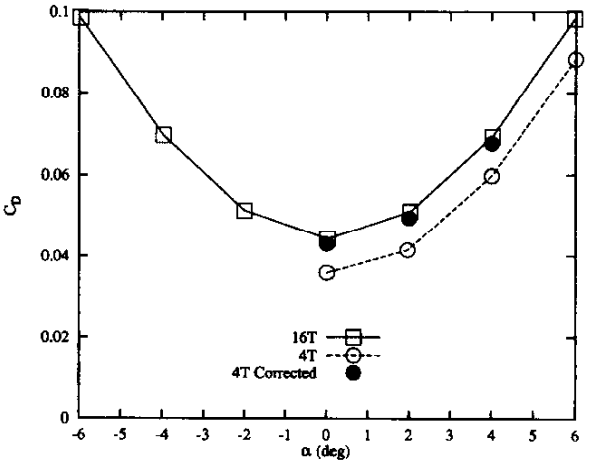

Figure 5.47 : WIM4T corrected drag coefficients using the Pretest-TNS code. M = 0,95, τ = 5 percent

Rule for Wall Interference (TARWI) discussed in Section 5.4.8 and 5.4.9 in which the zero-lift wave drag blockage interference of the full-up three-dimensional configuration is identical to that of its equivalent body of revolution.

Fig. 5.48 tests applicability of the above approximation for the data of Figure 5.47. The solid curve uses the experimental value of C_{L_α} from Figure 5.45.

The dash curve uses the classical theoretical estimate of C_{L_α} described in Heaslet and Lomax[1] (1954) for a swept trailing edge wing body approximating WIM4T

$$C_{L_\alpha} = \frac{\pi}{2} AR\left[1+\left(\frac{R_0}{s_0}\right)^4 - \left(\frac{t_0}{s_0}\right)^2 - \frac{R_0^2}{s_0^2 t_0^2} + \left(\frac{R_0}{s_0}\right)^2\right]$$

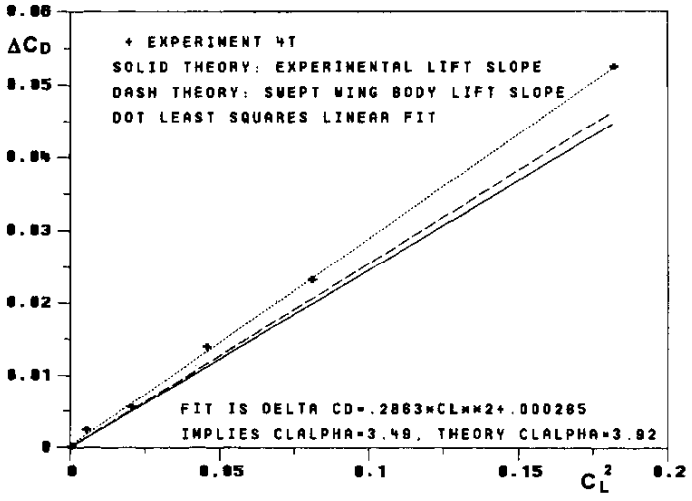

Figure 5.48 : Comparison of WIM4T drag rise due to lift data from AEDC experiments with slender body theory for swept trailing edge wing bodies.

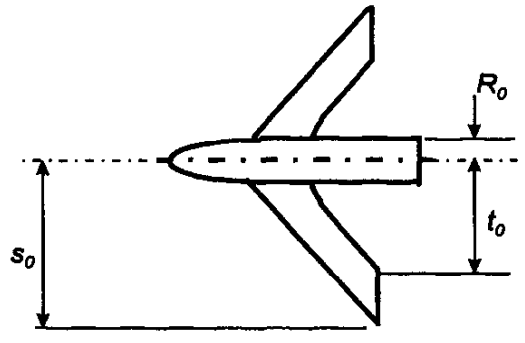

Figure 5.49 : Swept slender body used to estimate C_{L_α} for drag due to lift in the Heaslet and Lomax equation

where AR is the aspect ratio of the wing, R_0 is the body radius, and the other quantities are shown in Figure 5.49. Although a small discrepancy exists, the approximating equation for $\Delta C_D/C_L^2$ matches the trend of the data quite well, in view of the liberties taken in the approximation of WIM4T or WIM1T by the idealised configuration (IC) of Figure 5.49. It has the tips perpendicular to the flow as contrasted to that of WIM4T or WIM1T which are streamwise. Furthermore, the IC trailing edge is curved, to simplify the calculation by eliminating the upstream influence and coupling of the trailing edge vortex sheet. This effect has only received limited theoretical attention in the literature but is a pervasive issue. Additionally, boundary layer separation and transition effects have been ignored. The basic model is the previously-mentioned Adams-Sears transonic not-so-slender body theory which idealises the slender body flow as incompressible. To validate the linearity of the curve of ΔC_D against C_L^2 the dotted empirical linear fit is also shown. (For low aspect shapes, nonlinearities at higher incidence are associated with leading edge separation.) *Summarising, the wall interference is roughly independent of incidence, and can be obtained by solving only* ***one*** *problem for zero lift, i.e. the shift in* C_{D_0} *from the free field to confined flow. This problem*

[1]Heaslet, M.A. and Lomax, H. 1954, "Supersonic and Transonic Small Perturbation Theory," High Speed Aerodynamics and Jet Propulsion VI, General Theory of High Speed Aerodynamics, Princeton Series, pp.122-344

can be further simplified by reducing it from a 3-D to 2-D desktop calculation by the TARWI. The robustness of the latter for not-so-slender swept trailing edge wing bodies such as the WIM1T needs to be assessed.

5.3.3.6 SSLV WALL-INTERFERENCE COMPUTATIONS

Computations of the Tunnel 16T wall interference were part of an effort to study the difference between existing wind-tunnel database and flight-measured, transonic aerodynamic loads experienced by the SSLV during ascent. The AEDC wall boundary condition was incorporated into the NASA/ARC OVERFLOW code (Buning, *et al.* [31]). The computations were all performed with the OVERFLOW code which was used to solve the TNS equation with a Baldwin-Lomax turbulence model in all regions except the far field. All tunnel computations were performed with the AEDC wall boundary condition. Wall interference computations were performed at one high subsonic freestream Mach number and at two low supersonic freestream Mach numbers, M = 1.05 and 1.25. The former Mach number led to Group 3 flow.

A comparison of free-air and tunnel Mach number contours is shown in Figure 5.50 for $M = 1.05$ and α = -4.66°. The contours are shown for the lateral plane of symmetry with subsonic flow shown in grey, while supersonic flow is shown in colour. The launch vehicle profile is shown in white along with supersonic flow that exceeds M = 1.1. The bow shock and downstream Mach contours are seen to obliquely cross the line where the wind-tunnel walls would be located.

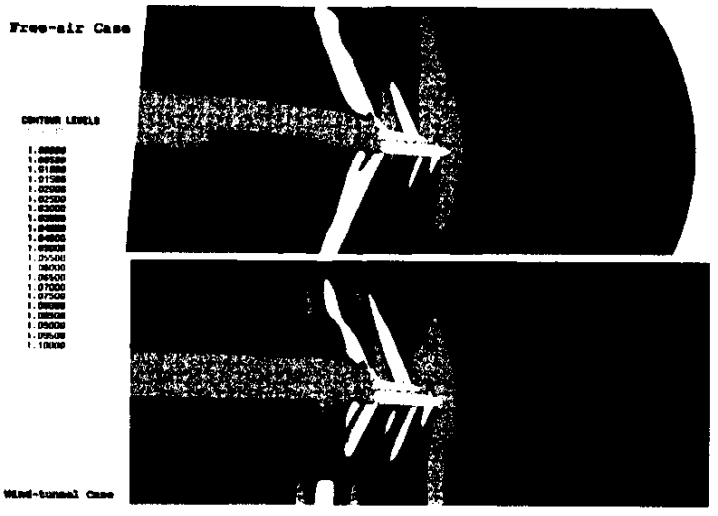

Figure 5.50 : Computed Mach number contours on the plane of symmetry, M = 1,05, α = -4.7 deg.

A comparison of the Orbiter forebody (all surfaces except the base and top of the body flap) normal force and pitching moment for three 16T wind-tunnel tests is shown in Figure 5.51 along with the numerical results. The three wind-tunnel tests show very interesting trends. At $M = 0.95$ and $M = 1.25$, the data from IA-156 and IA-105A, which were conducted in 1977, agree very well thus indicating the lack of wall-interference effects at these Mach numbers. The data at $M = 1.05$ for the two-percent model (IA-156, blockage ratio = 0.3 percent) show a negative increment in forebody normal force, and a positive increment in forebody pitching moment, relative to the three-percent model (IA-105A, blockage ratio = 0.7%). These increments are attributed to wall interference effects in the data from the three-percent model.

In addition to the wall-interference effect, the bias between the recent IA-613A data and the two older tests is also very interesting. The difference between the test results could be due to the improved fidelity of the blockage between the Orbiter and ET at the aft attach station for the IA-613A test. Regardless of the cause, the data have moved closer to the Orbiter flight data.

The computed normal force and pitching moment from the free-air and wind-tunnel CFD solutions at $M = 1.25$ are in very good agreement with each other and the IA-613A data, indicating the absence of

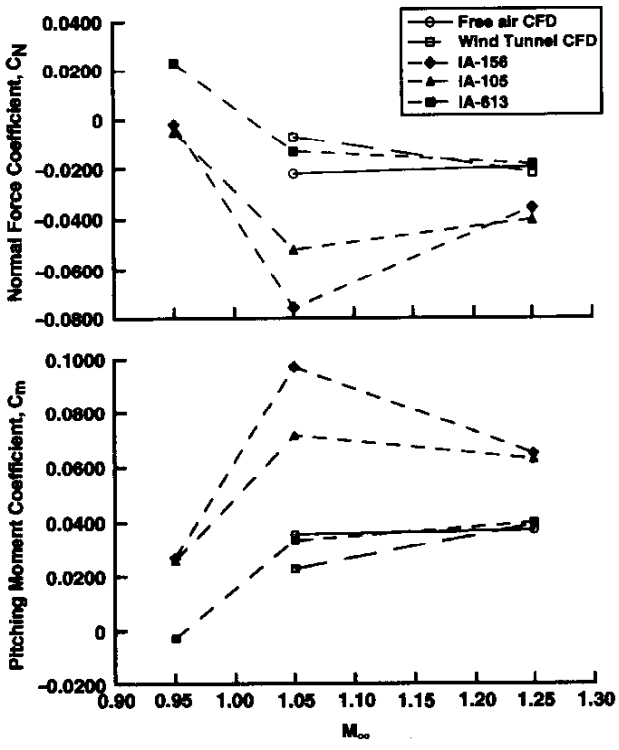

Figure 5.51 : Computed and experimental Orbiter forebody integrated loads

wall interference effects at this Mach number as do the data from the IA-156 and IA-105A tests. At $M = 1.05$, the numerical results are near the IA-613A data, with the wind-tunnel CFD results showing a positive normal force and a negative pitching moment increment. The increment magnitude is approximately 70 percent of the difference between the IA-156 and IA-105A data. Absolute fidelity between the IA-613A data and the computed tunnel values is not achieved in the $M = 1.05$ case as in the $M = 1.25$ case. However, the increments are shown to be in the right direction and could be used to correct 70 percent of the wall interference at a near sonic condition.

By comparing the tunnel flow-field calculations with corresponding free-air flow-field calculations, an assessment of the wall interference was made. Significant wall interference effects were demonstrated at $M = 1.05$ while results at M = 1.25 showed no interference. Inclusion of the tunnel wall boundary condition in the CFD model improved the correlation of the numerical results with the tunnel data. Agreement between the calculated wind-tunnel and the Tunnel 16T pressure distributions improved, particularly on the mid section of the vehicle where the interference effects are greatest. Increments between computed free-air and wind-tunnel normal force and pitching moment coefficients compared favourably with incremental data between models of two different scales.

5.3.3.7 TST Wall-Interference Computations

The difficulty of computing transonic wall interference in perforated-wall wind tunnels is demonstrated with this database as well as the need for additional technology development in this area. Wall interference computations for Tunnel 4T were performed on the TST model using the WIAC approach and the pretest-predictive approach. The computations involved computing the flow field with the Euler equations everywhere except in the vicinity of the wing. The near-field wing solutions were obtained by solving the thin-layer Navier-Stokes for fully turbulent flow. A Baldwin-Lomax turbulence model was used. The pretest approach involved imposing the tested wall configuration, 5% uniform porosity on all walls. The WIAC approach involved interpolating the measured pressure distribution onto the computational grid and prescribing it as the boundary condition.

Figure 5.52a shows a comparison of 16T reference and 4T drag variation with Mach number (drag rise) at a fixed lift coefficient C_L = 0.3 for natural transition at a chord Reynolds number (Re_c) of 2.7 × 10^6. At $M = 0.6$, the drag measured in 4T is 22 counts (1 count = 0.0001) higher than measured in 16T while at $M = 0.9$ the 4T drag is 104 counts lower than 16T drag. The drag rise is delayed in 4T. A crossover point, where the drag difference is zero, occurs at $M = 0.835$. Figure 5.52b shows the drag rise

comparison for the same conditions while forward tripping the boundary layer at approximately 10% of wing chord. The drag levels for the tripped and untripped configurations are different, but the differences between 16T and 4T are almost identical indicating that wing transition is not a significant factor between 16T and 4T for this model at these conditions. This figure also illustrates how much the sign and magnitude of wall interference vary over the transonic regime.

At $M = 0.6$, the flow is subcritical and offers the opportunity to look at the data and computational comparison without shocks. Figure 5.53 shows the force and moment data comparisons between 16T and 4T for natural transition at $Re_c = 2.7 \times 10^6$. The normal-force coefficient comparison when plotted against angle of attack shows no slope difference and only a small variation at the larger angles. However, pitching-moment coefficient does show a slope variation. The slope of the 4T pitching-moment curve is much smaller than 16T. The drag-coefficient difference between the two tunnels remains fairly constant with angle of attack at approximately 22 counts.

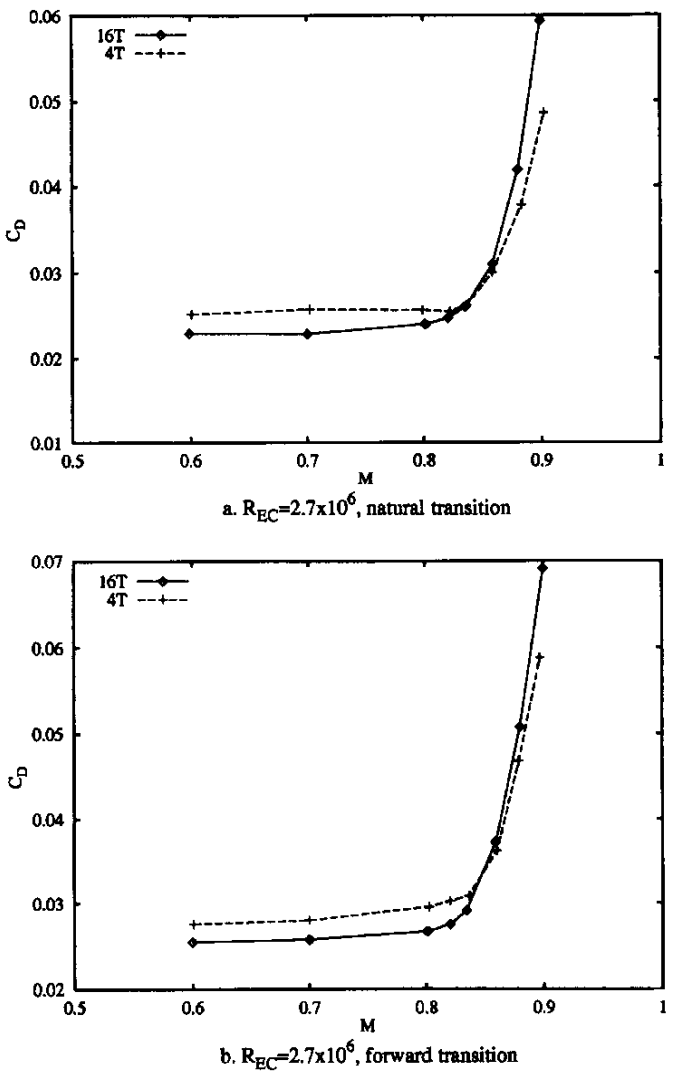

Figure 5.52 : 16T/4T drag-coefficient vs. Mach-number comparison, $C_L = 0.3$

The corresponding model pressures at the five wing spanwise arrays and on the canopy are shown in Fig. 5.54 for $\alpha = 3°$. Also shown in Fig. 5.53 is a comparison of balance-cavity and average duct-exit pressures. The experimental model pressures indicate virtually no difference in the flow over the forward fuselage or the wings. Wall interference does not appear to be a factor on the local flow over these areas of the model. However, model pressures from the cavity and duct pressures (located at approximately the same model station) show a difference between the tunnels. Both show a slightly lower pressure in Tunnel 4T indicating a slight gradient in the pressure difference between the tunnels over the aft portion of the model. Figure 5.55 shows the pressures measured with the pipes corresponding to the model pressures in Fig. 5.54. These pressures indicate an acceleration of the flow above the centreline and starting at tunnel station 130. The end of the model was at tunnel station 130.7. The downstream pressure variation produces a buoyancy effect where the lower pressure in this region causes a higher drag coefficient in 4T. The lower pitching-moment coefficient slope is also attributed to the downstream variations. The flow accelerates over the tail and generates more lift and nose down pitching moment. Because most of the model lift is generated by the wings, it follows that an aft model

gradient would not significantly affect the lift slope in 4T, which the data support. Since the pressure coefficient at the upstream pipe location is approximately zero, the blockage of the model did not affect the tunnel Mach number at these conditions.

Also, Figs. 5.54 - 5.55 show the computed model and measurement-surface pressure distributions for the free-air boundary condition, the AEDC boundary condition and the measured pressure distribution imposed. Good agreement is shown between the computed results and the corresponding data. The model-pressure increment between the free-air and AEDC boundary condition is larger than the experimental data show. These computational results indicate the AEDC perforated wall boundary condition prescribes a wall behaviour that is slightly too open. In addition, the AEDC boundary condition does not duplicate the downstream behaviour of the pressure distribution at the measurement surface. Imposing the measured pipe pressures yields model pressures that are in better agreement with the free-air computations than the wall boundary results. Specifying the pressures boundary condition does not seem to have any effect on the aft fuselage pressure distribution. To see an effect, the fuselage region must be computed by solving the Navier-Stokes equations. The pressure increments between the in-tunnel solutions and the free-air solutions have not been integrated to determine the force and moment corrections to the 4T data from these calculations.

The flow at $M = 0.835$ is supercritical. The force and moment data comparison between 16T and 4T are shown in Fig. 5.56, and the model pressure distribution for $\alpha = 3°$ is shown in Fig. 5.57. The wing and canopy pressures distributions show significant differences between 16T and 4T. All but the first few canopy pressures in 4T are higher, the 4T shock position is upstream of 16T, and the 4T wing pressures are generally higher forward of the shocks. These model-pressure differences indicate that the 4T walls at a uniform porosity (τ) of five percent are too open for this flow condition. The 4T normal-force coefficient agreement is in good agreement with 16T and the drag coefficient difference is small. The 4T pitching-moment coefficient is more negative resulting from the drop in forward wing loading. The average duct-exit and balance-cavity pressures now show a higher pressure in 4T than 16T (reversed from the $M = 0.6$ trend). The pipe pressures in Figure 5.58 also show a trend reversal from the $M = 0.6$ data. The flow at the end of the test section is now decelerating (increasing pressure). The cavity pressures are sensing this increase while the duct-exit pressures are sensing the wall openness and the change in the duct flow due to local flow changes. Although the drag difference between the facilities is small, neither the local effects of wall interference nor the buoyancy effects from the downstream pressure are small. At this flow condition the effects tend to cancel each other. The downstream pipe measurements as well as the 4T balance-cavity and duct-exit pressures show an increase in the base pressure which decreases the drag. The much higher forebody and wing pressures indicate that the 4T walls are too open. These higher local pressures increase the drag. The openness of the wall reduces the shock strength and tends to alter the aft wing pressure recovery at $\alpha = 4°$. Again, the upstream pipe pressure coefficients and the upstream canopy pressures appear to indicate tunnel Mach number is $M = 0.835$.

Figures 5.57 - 5.58 show the model and measurement-surface pressure distributions at $M = 0.835$ for the three computations. The model-pressure agreement between the AEDC tunnel wall boundary condition specified and with the interface pressure specified is good. The calculations also reproduce the corresponding measured model pressure including the difference in shock location and strength. In addition, the wall boundary condition reproduced the wall pressure signature everywhere except at the downstream end of the test section. Again, specifying the pressure boundary condition does not seem to have any effect on the aft fuselage pressure distribution. The pressure increments between the in-tunnel solutions and the free-air solution have not been integrated to determine the force and moment corrections for these calculations.

Goethert [71] shows the acceleration or deceleration of the downstream flow is caused by providing the wrong mass flow through the perforated walls. Excessive outflow causes the flow to decelerate, and insufficient outflow causes the flow to accelerate. From the pipe pressure measurements, it is evident that this is exactly the situation that occurred during this test. Because of the length and position of TST model, the downstream pressure distribution has a strong buoyancy effect. However, calculations to date, have not shown the buoyancy effect. Additional investigation is needed to integrate force on different areas of the test article, to model and compute the fuselage region using Navier-Stokes equations, and to investigate the use of different downstream boundary conditions.

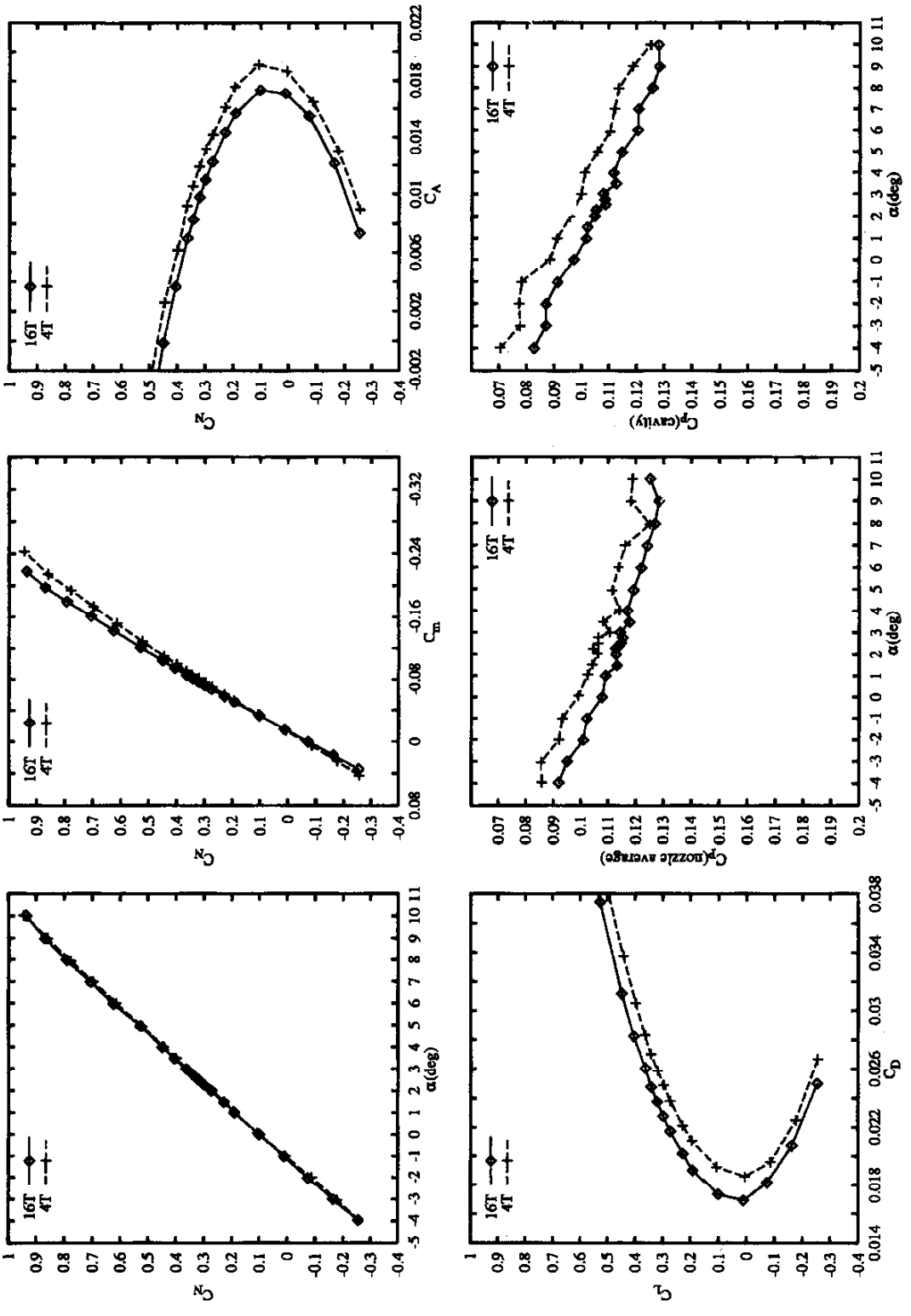

Figure 5.53 : 16T/4T force and moment, duct exit and balance cavity comparisons, M=0.6, R_{EC}=2,7x10^6, natural transition

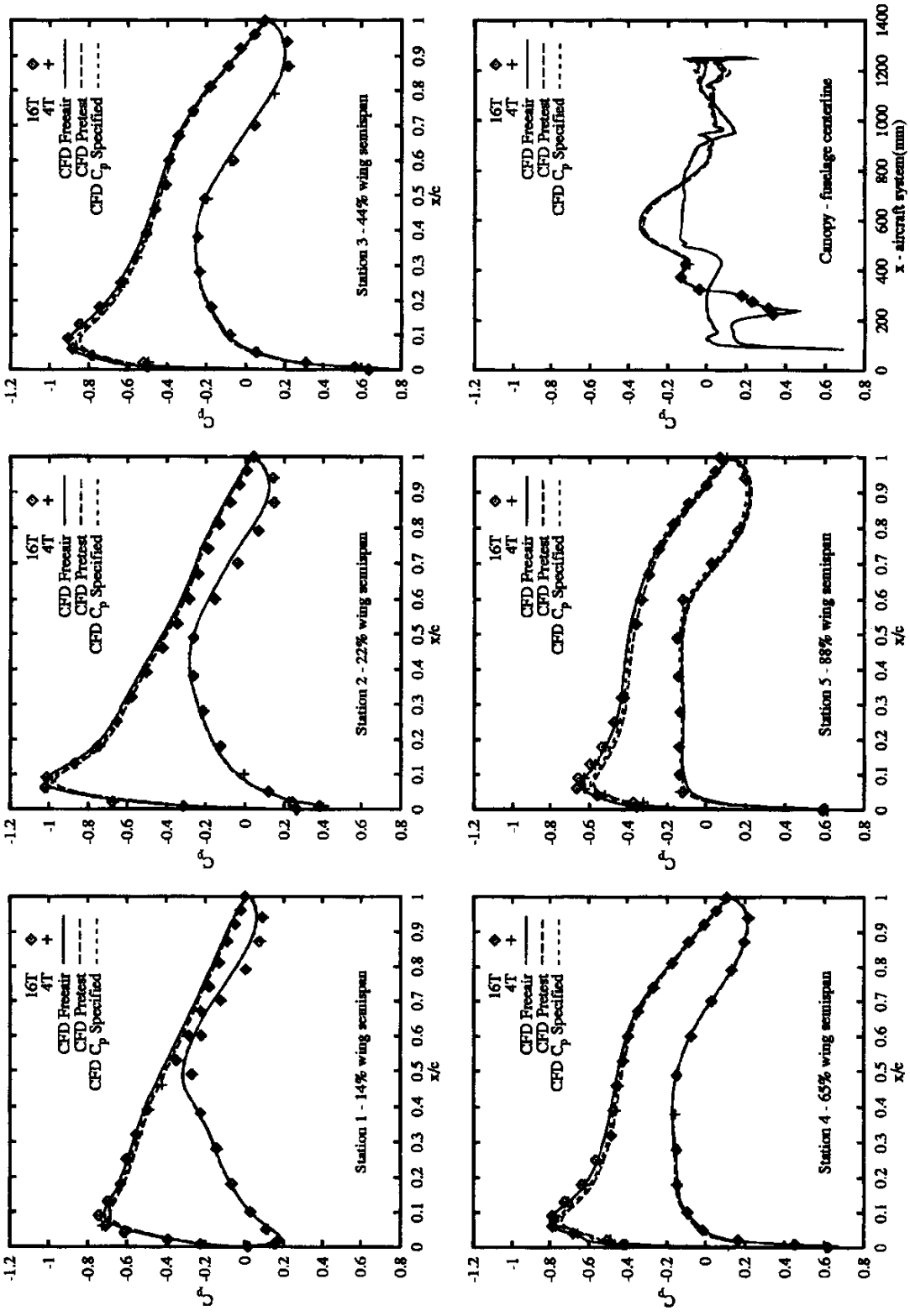

Figure 5.54 : Measured and computed model pressures, M=0.6, α=0.3 deg, R_{EC}=2.7x10^6

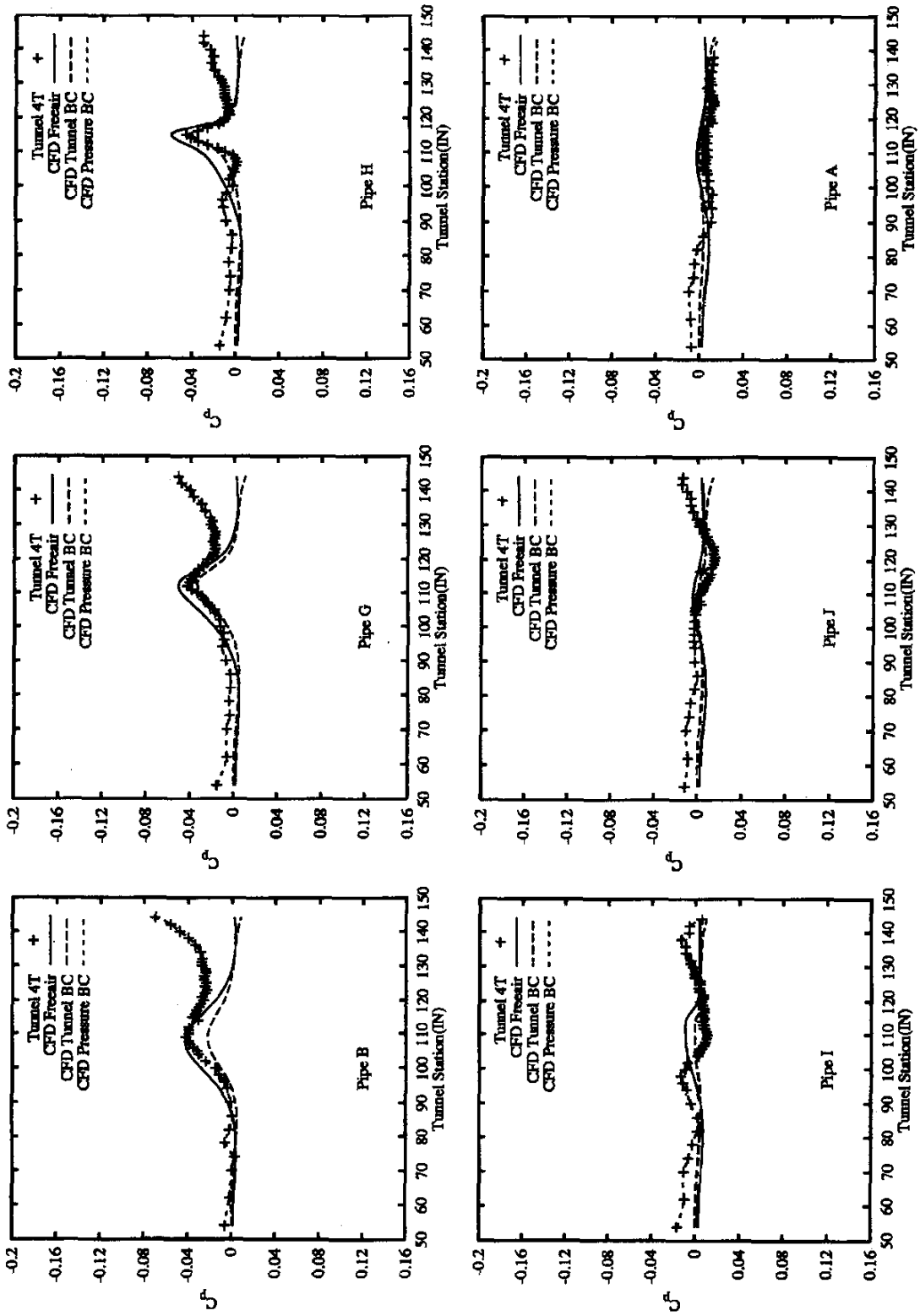

Figure 5.55 : Computational and measured interface-pressure comparison, M = 0.6, α = 3 deg, $R_{EC} = 2.7 \times 10^6$, natural transition

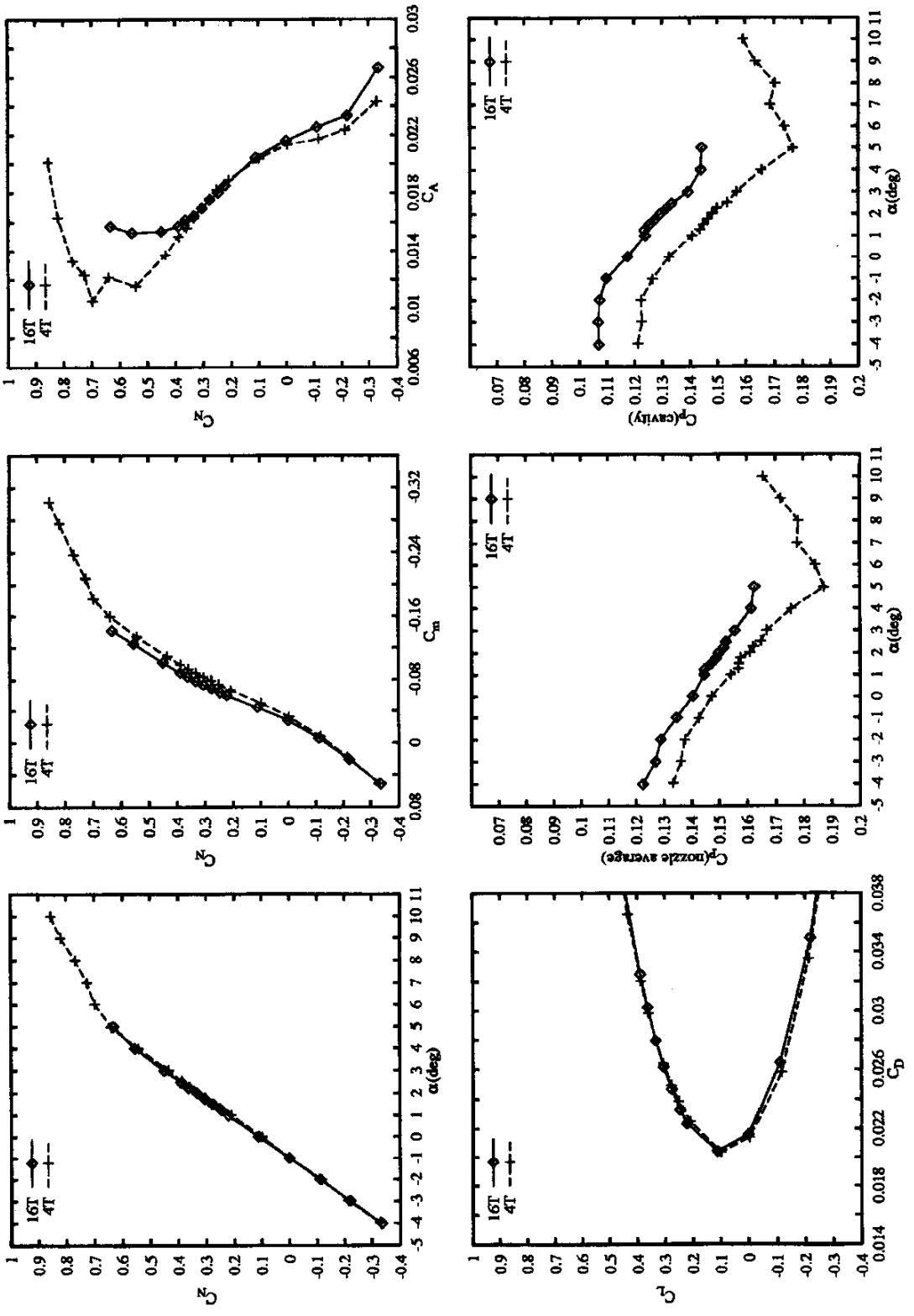

Figure 5.56 : 16T/4T force and moment, duct-exit and balance-cavity comparisons, M = 0.835, R_{EC} = 2.7x10^6, natural transition

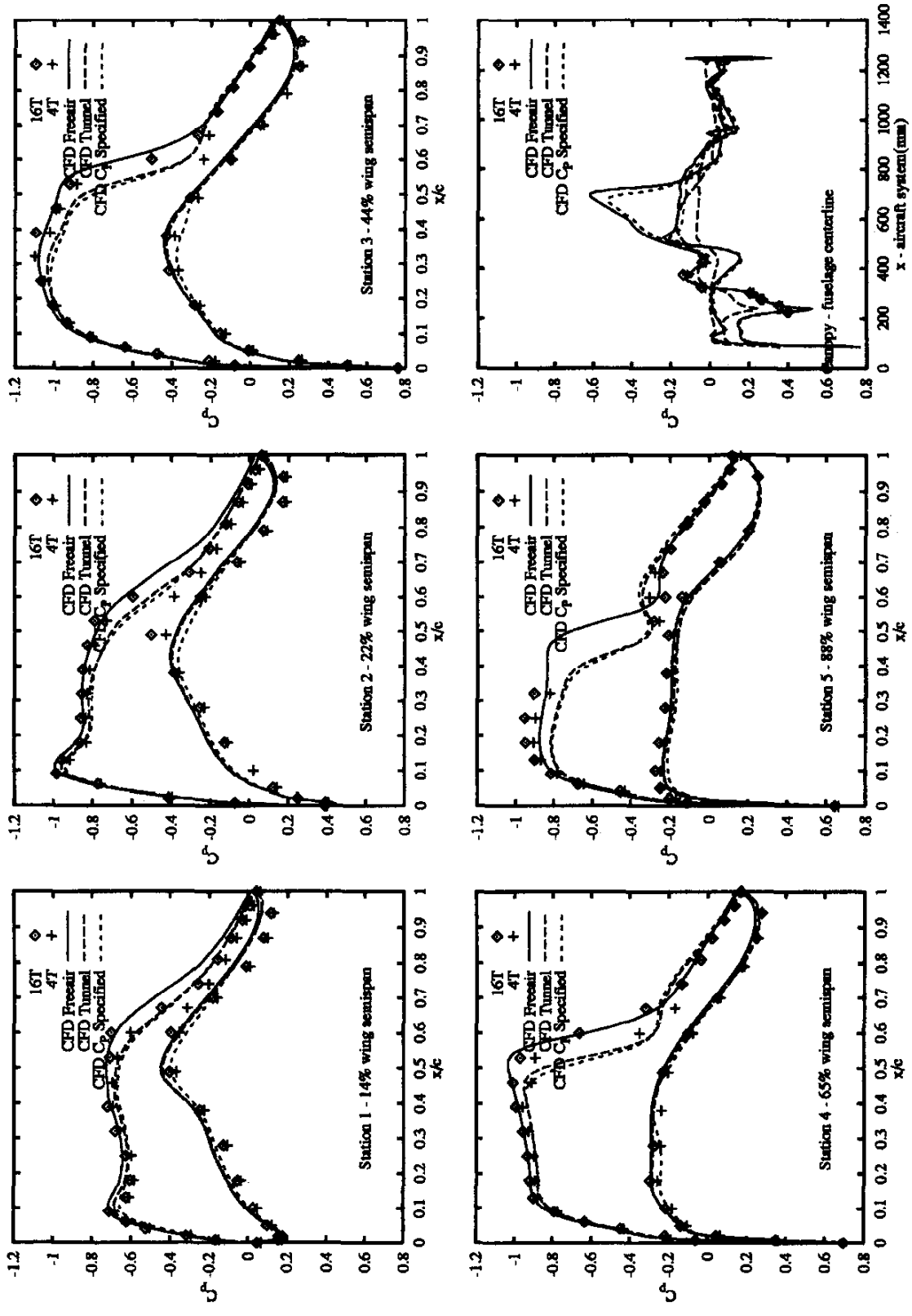

Figure 5.57 : Measured and computed model pressures, M = 0,835, α = 3 deg, $R_{EC} = 2.7 \times 10^6$, natural transition

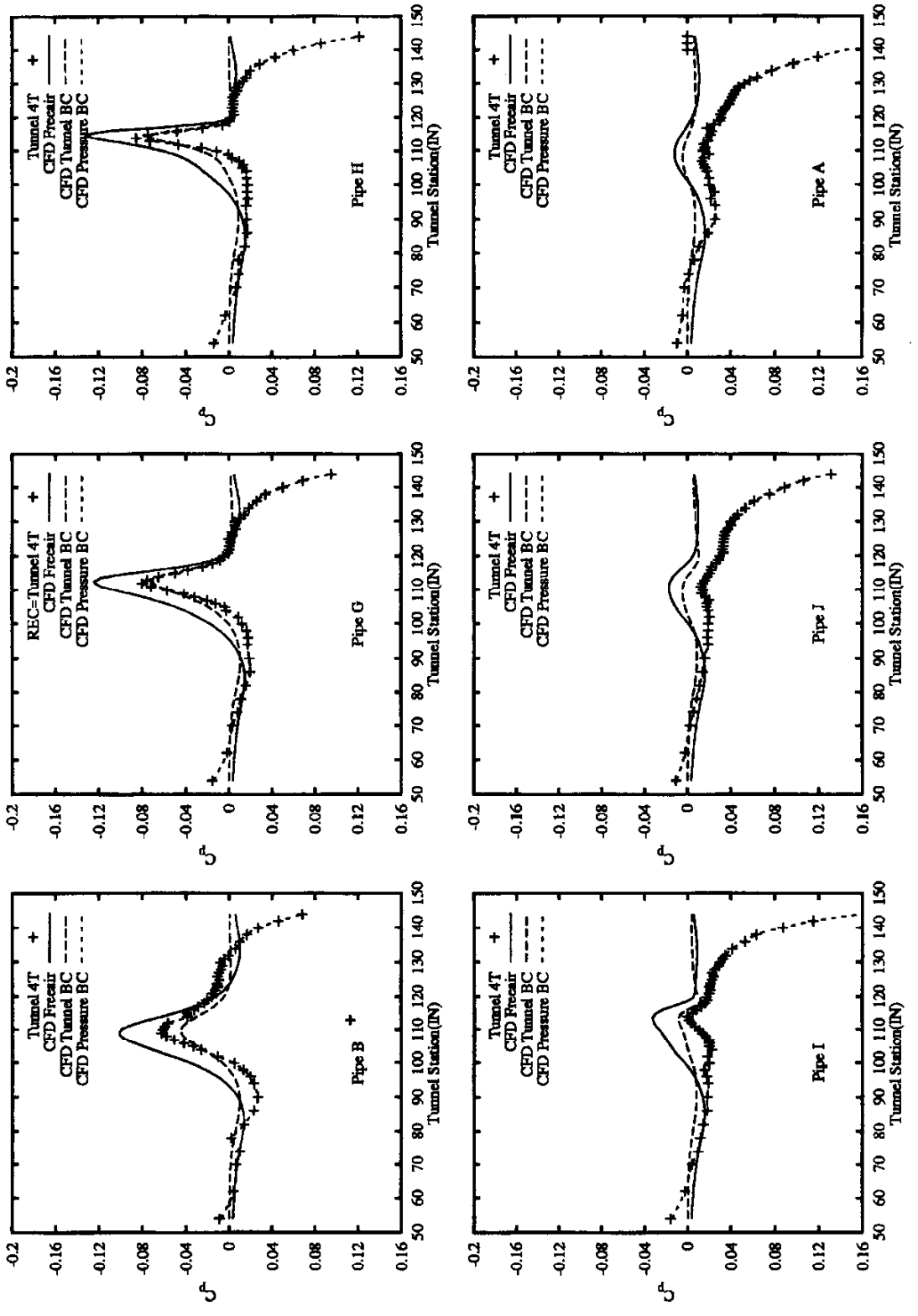

Figure 5.58 : Computational and measured interface-pressure comparison, M = 0.835, α = 3 deg, $R_{EC} = 2.7 \times 10^6$, natural transition

5.3.3.8 CONCLUSION

Accurate wall interference corrections were demonstrated for high subsonic flow and low supersonic flow using the pretest-predictive approach where the AEDC perforated wall boundary condition is specified and using the WIAC approach where the pressure distribution is specified near the wall. The specification of the AEDC perforated wall boundary condition reproduced the pressure signature near the wall to a high degree of accuracy and yielded model pressures in good agreement with the pressure specified results. The TST database is an excellent database to evaluate wall interference strategies and should be exploited for these purposes.

5.3.4 NASA LANGLEY WIAC METHODS

The research interest in transonic wall interference correction techniques and methods at NASA Langley Research Center was prompted by the decision to build the National Transonic Facility (NTF) there in the mid 1970's. Since the NTF would be a variable speed, pressure, and temperature (cryogenic) facility, then one could simultaneously match flight Mach number, Reynolds number, and dynamic pressure, thereby ideally, leaving tunnel interference (wall and support) as the major source of uncertainty in its data. A summary of the resulting wind-tunnel-wall interference assessment and correction (WIAC) research from the mid 1970's through about 1990 is given in Newman, *et al.* [142], [143]. Many references giving the approaches used, details, and results are cited in these two papers.

The development of several sequences of WIAC codes occurred, more or less, in parallel. The non-linear transonic WIAC procedures were to be studied using a 2–D TSDE approximation in conjunction with an extensive airfoil database being generated in the 0.3-m Transonic Cryogenic Tunnel (TCT). Both linear (fast) and non-linear 3–D procedures were envisioned for eventual use in the NTF and sequences of WIAC codes were developed for both. Initial 3-D studies and codes were developed under NASA Contract by Flow Research Company with later development, implementation, and testing done in-house. The following two subsections will briefly discuss the 2–D and 3–D developments separately, with that for the non-linear airfoil WIAC first. Some of the important lessons learned there have not yet been incorporated in any 3–D procedure. However, a few remarks regarding the relationship of the present WIAC philosophies and procedures to those already discussed in 5.3.2 and 5.3.3 are needed first.

The WIAC procedures discussed in all three sections (5.3.2, 5.3.3, and the present section, 5.3.4) utilise differences between two CFD solutions, one in tunnel and one in free-air, to determine interference corrections and use measured wall or near-wall pressures to formulate the "wall" boundary condition for the in-tunnel simulation. However, for the WIAC procedures previously described in 5.3.2 and 5.3.3, corrections are made to determine a pressure difference on the model and, when integrated, corrections for the forces and moments result. This assumption is that the tunnel Mach number (M) and angle-of-attack (α) are correct. The present philosophy is that there are corrections to M and α, just as in the classical low-speed flow, because the tunnel has imposed an incorrect far field on the model flow. It is not known what the correct far-field conditions are, and the present non-linear procedures search for a far field M and α for which the computed surface pressure (not pressure coefficients) distribution best matches that measured (or computed) in the tunnel. This philosophy intends to preserve the sensitive transonic flow and its shock-wave/boundary-layer interactions which occurred in the tunnel flow on the model. In addition to the corrections for M and α, there also result corrections to the forces and moments due to normalising stream properties and incidence corrections. The present procedures are, therefore, variants of the initial or first point of view as discussed in 5.3.2.3. In any case, from whatever point of

view, one can determine corrections only by holding some property or properties invariant; perhaps it is not yet clear what the physical invariant(s) should be.

5.3.4.1 NON-LINEAR AIRFOIL TUNNEL WIAC CODES

The sequence of codes leading to TWNTN4A were developed from about 1977 to 1988. These codes are based on the (non-linear) TSDE CFD approximation and 1–D measured pressure data arrays on the top and bottom tunnel walls (outer boundary) and upper and lower airfoil model surfaces (inner boundary) are used as boundary conditions for the in-tunnel simulation. That is, this is a two-measured data array WIAC procedure. This inverse (pressure prescribed) boundary condition is essentially applied along the airfoil, a two-sided slit along the y=0 line of length equal to the chord, and allows an effective inviscid shape to be determined which approximates many of the viscous layer responses, including those associated with shock interactions and flow separations. It is then this effective inviscid shape which is used as the inner boundary condition for the free-air CFD calculation which is done on a Cartesian grid which is simply an extension of the in-tunnel grid. That is, the in-tunnel grid is a proper subset of the free-air grid, allowing cancellation of computational truncation errors in the flow field around the model.

The basic ideas and initial code, TWINTAN, were developed by Kemp [99], [100] and it was soon realised that the sidewall boundary-layer approximate models discussed in 5.2.2 due to Barnwell and Sewall [19] needed to be included for correction of the 0.3-m TCT airfoil data taken in the 8- X 24-inch slotted wall test section (see Kemp and Adcock [102] and Kemp [101]). Incorporation of this 4-wall code, TWINTN4, into an automated procedure for use with 0.3-m TCT airfoil data was accomplished by Gumbert, *et al.* [80], Gumbert and Newman [79], and Gumbert [78]. This procedure included a capability for multi-pass corrections, using the airfoil leading edge as a flow angularity probe, to iteratively determine the unmeasured far-upstream flow angularity. Use of this procedure by Gumbert, *et al.* [81] also uncovered limitations due to the subsonic origins of the SWBL approximations as mentioned in 5.2.2. Inclusion of the wall shapes appropriate to an adapted wall as the outer boundary upon which the measured far-field pressures are imposed on the in-tunnel flow simulation, produced the tool TWNTN4A, capable of also assessing and correcting residual interference in adapted-wall airfoil tunnels. The procedure and results have been reported by Green and Newman [75], [76], Green and Mineck [74], and Green, *et al.* [77].

The general premise is that transonic airfoil data contain wall interference; it is just a matter of how much. The TWNTN4A WIAC procedure is a post-test means for trying to quantify the severity of wall effects. Incorporation of the TWNTN4A code as part of the 0.3-m TCT data reduction is contemplated in the current re-engineering of NASA tunnels and is possible with present-technology high-end workstations. Space here does not permit showing the many WIAC results from the papers cited above, and showing only a few results would not be representative of all the studies. The major conclusions from these 2-D WIAC studies are:

(a) Both upstream flow angle assessment and a non-linear SWBL approximation are required in transonic airfoil WIAC procedure.

(b) Both the linear CAE-NAI interference potential and the non-linear NASA TSDE WIAC procedures make nearly the same and reasonably good corrections for M and α into the transonic flow regime if both items in (a) above are included.

(c) The model shock interacting with the SWBL generally destroys the 2–D symmetry before this shock reaches the top or bottom tunnel walls.

(d) Valid correction of transonic data that are subject to unsteady and even moderate 3–D SWBL effects may require an unsteady, 3–D, Navier-Stokes WIAC procedure.

5.3.4.2 Linear and Non-linear 3D WIAC Codes

Initial NASA Langley 3-D WIAC studies were done and codes developed under a contract to Flow Research Company. Linear, slender lifting-body, and non-linear TSDE potential theory based WIAC codes and procedures were formulated, developed, and tested, code-on-code. These results were reported by Rizk and Smithmeyer [156] and Rizk, *et al.* [157], [158]. Elements of the linear code LINCOR, written by Rizk and Smithmeyer [156], were used by Kemp [98], [95] in the STIPAN analysis and PANCOR WIAC codes, developed for the slotted-wall NTF, as discussed in 5.3.1.1. The non-linear TSDE WIAC code TUNCOR, originally developed by Rizk *et al.* [157], and later enhanced by Rizk [155], has been tested at NASA Langley and AEDC on transonic tunnel data. The NASA Langley results for several applications are given in Newman, *et al.* [142], [143]; results from the linear code PANCOR are also included. Both of these procedures are one-measured data array schemes; that is, 2-D pressure data arrays measured on or near the walls are used in the outer boundary condition for the in-tunnel flow simulation.

As pointed out by Sickles and Erickson [167], [168] and discussed here in 5.3.3.1, application of the TUNCOR and other inviscid flow solvers gave accurate corrections for subcritical and mildly supercritical flows (Group 1) but were inadequate, giving wrong corrections, for strongly supercritical flows (Group 2). This behaviour was associated with the inviscid codes' inability to properly simulate the viscous flow, particularly for strongly shocked and separated flows. As a consequence, NASA Langley began implementing the correction procedure of TUNCOR into another TSDE code in which a number of approximation improvements, including an interacted boundary layer (IBL) were being incorporated. This new code, WIACX (see Garriz and Haigler [68], has been used by Garriz, *et al.* [69] and Green, *et al.* [77] to correct semi-span wing data which falls into the Group 1 category. Since the IBL procedure has not been incorporated into the WIACX code, it has not been tried on Group 2 flows. However, the IBL procedure gives remarkable results for shocked and separated transonic flows when used in the CAP-TSD analysis code upon which WIACX is based.

As noted in 5.4.4.1, the TWNTN4A airfoil WIAC code makes use of two 1-D measured pressure arrays: the far-field array; generally taken above and below the airfoil and an airfoil surface array. Extensions of this concept to 3-D were made assuming that model surface pressure measurements would never be detailed enough to provide an adequate inner boundary condition for an inverse problem reconstruction of the effective test article shape. In addition, for many tests, pressure measurements are not made. Consequently, the 3-D implementations of Kemp's [99], [100] original concept were with 2-D measured far-field pressure arrays and a geometric model description as the inner boundary condition for a direct problem. Using this latter boundary condition, the flow code is required to produce the viscous effects, including shock interactions and separations, in order to obtain the effective shape that is present in the tunnel test and also the free-air simulation, both of which are required in a non-linear WIAC procedure. Successful application of pressure sensitive paint, predicted by some to be a routine technique soon, would provide the 2-D measured surface pressure arrays needed for a 3-D, two-measured variable array WIAC procedure, not requiring measured flow angularity arrays. Details of the envisioned procedure would involve using an unstructured grid Euler flow solver (to easily mesh the configuration and tunnel test section geometry) on a rather coarse grid (by current CFD standards) to solve the inverse in-tunnel problem very efficiently. The resulting "effective inviscid shape" (which contains viscous effect

contributions) is then used in the free-air simulation (unstructured-grid Euler flow solver with in-tunnel grid augmented to reach the required free-air far-field boundary) to obtain the Mach number and angle of attack which minimise an equivalence condition for determining wall interference. In this procedure, it is assumed that the pressures measured on the model are correct (valid) but that the tunnel has imposed the wrong far-field flow. The WIAC procedure deduces effectively averaged corrections to the magnitude and direction of the far-field flow subject to an equivalence condition. Experimental data are then re-reduced at the corrected flow conditions.

5.4 ASYMPTOTIC METHODS FOR TRANSONIC TUNNEL WALL INTERFERENCE*

5.4.1 BACKGROUND

As previously discussed, procedures to treat subsonic wall interference have received considerable attention. A view of existing wall correction technology for this regime can be obtained from Garner *et al.* [67], Pindzola and Lo [151], and Mokry *et al* [133], other chapters in this AGARDograph and previous sections in this chapter. By contrast and as has been previously indicated in this chapter, the methodology for the transonic case is much less developed since it gives rise to a particularly difficult non-linear, mixed-flow environment. Current approaches are exemplified by Kraft *et al.* [109], Donegan *et al.* [47], and Newman *et al.* [142] and in Section 5.3. In addition to the utility of large-scale computationally intensive methods for transonic wall correction prediction, approaches that can reduce the number of input parameters necessary to compute the correction, shed light on the physics of the wall interference phenomena, simplify the necessary computations, and apply to three dimensions as well as unsteady flows are needed. Asymptotic as well as combined asymptotic and numerical (CAN) procedures such as those described in Lifshitz and Fonarev [115], Chan [34], Blynskaya and Lifshitz [29], Cole [39], Berndt [24], Malmuth and Cole [122], Malmuth *et al.* [125], Malmuth [121], [125], provide such advantages. Furthermore, such techniques can stimulate valuable interactions with the other methods previously mentioned to suggest possible improvements, as well as derive beneficial features from them. This section summarises CAN methods for predicting wall interference. Theories for slender aeroplane configurations and high aspect ratio wings will be outlined as well as computational methods to determine the interference flows for these limiting cases. Other approaches in which the asymptotics can be integrated with experimental measurements to improve WIAC procedures such as those in Sickles and Erickson [167], are summarised in Malmuth *et al.* [125], and Malmuth *et al.* [123].

5.4.2 OVERVIEW OF ASYMPTOTIC PROCEDURES FOR SMALL SLENDER AND LARGE ASPECT RATIO CONFIGURATIONS

For both the slender body and high aspect ratio cases, the wall interference is obtained by a systematic asymptotic expansion procedure. Each is represented by a secondary approximation within a Karman-Guderley (KG) Transonic Small Disturbance Theory framework. In what follows, the asymptotic structure for the two limits and the formulation of the boundary value problems for the interference perturbation potential are outlined.

* Portions of this effort were sponsored by the Air Force Office of Scientific Research, Air Force Materials Command, USAF under Contract No. F49620-96-C-0004, as well as Arnold Engineering Development Center. Air Force Systems Command, under Contracts F40600-82-C-0005 and F40600-84-C-0010. The U.S. government is authorized to reproduce and distribute reprints for government purposes notwithstanding any copyright notation thereon. The views and conclusions herein are those of the authors and should not be interpreted as necessarily representing the official policies or endorsements, either expressed or implied, of the Air Force Office of Scientific Research or the U.S. Government.

5.4.3 SMALL SLENDER CONFIGURATIONS

Figure 5.59 shows a schematic of a slender aeroplane of characteristic thickness ratio δ and incidence α within a circular wind tunnel. The quantities h and h' respectively represent radii of "pressure-specified interface" and wall cylinders. The h interface surface has been introduced to provide experimental pressure data to bypass difficult simulation of ventilated wall boundary conditions. A double limit consisting of the transonic small disturbance slender body theory (TSDST) described in Cole and Cook [37], and large tunnel radius in units of the body length h in Malmuth [121], [125], and Malmuth [120], give the three-deck structure shown. In the horizontally shaded "axis" region, cross-flow gradients dominate and the flow is nearly harmonic in cross flow planes. In the slant-shaded "central" zone, relaxation to an axisymmetric non-linear TSDST environment has occurred. This leads to the Equivalence Rule given in Oswatitsch and Keune [147], and elsewhere for the free field (no walls present) flow. TSDST in the central region is formulated within a distinguished asymptotic limit involving δ, α, and the freestream Mach number M_∞ and leads to the axisymmetric KG equation for the perturbation potential ϕ. For $H \equiv h\delta \to \infty$ as $\delta \to 0$ the walls linearly and weakly perturb the central region flow. Treatment of the case $H = O(1)$ is given in Section 5.4.8 . **If the walls are axially symmetric,* then Malmuth [122], [121], [125], demonstrate that an "area rule for wall interference" holds in which the interaction of an asymmetric body with walls is the same as its equivalent body of revolution.** This interaction is computed from solution of a boundary value problem of the wall correction ϕ_1 to the basic free field flow perturbation potential ϕ_0 whose equation of motion is linear and of mixed type with variable discontinuous coefficients. It is similar to an equation to be shown for the high aspect ratio problem. For slender bodies, boundary conditions for this "variational" equation are obtained from matching with the axis region and a wall region (unshaded zone in Figure 5.59) where the approximation of small perturbations of the central region becomes nonuniform due to the $O(1)$ wall boundary conditions. This wall region is governed by the Prandtl-Glauert equation and the body appears as an imaged multipole for free jet and solid walls. An inner limit of the wall region provides far field boundary conditions for the variational equation of the central region interference flow. More general pressure-specified wall boundary conditions introduce Fourier transforms and averages of the wall pressure distribution into the far field boundary conditions. Involved matching procedures to establish this result are detailed in Malmuth [125] Numerical procedures and associated issues in solving boundary value problems of this type have been also discussed for the high aspect ratio theory in Malmuth [121], [125], [123].

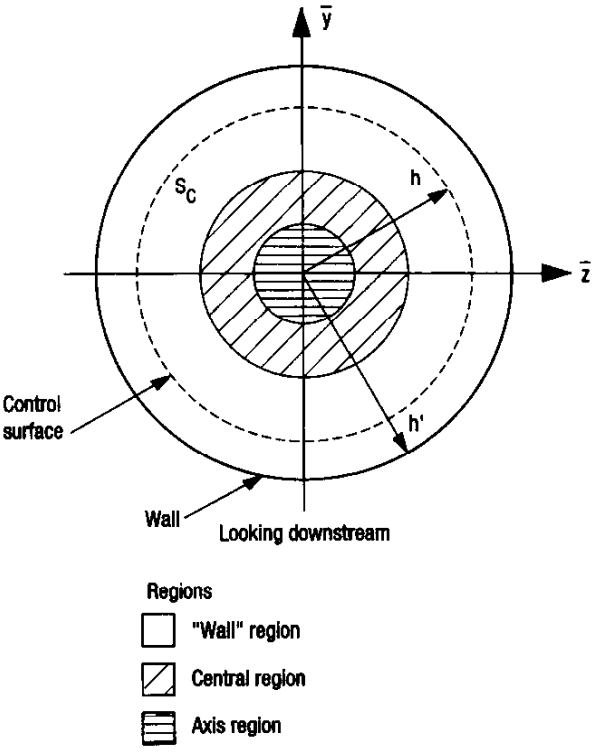

Figure 5.59 : Slender body within control surface in tunnel for $H^{-1} = O(1)$

* As will be seen in subsequent sections, this condition as well as $H = O(1)$ can be relaxed.

5.4.4 HIGH ASPECT RATIO THEORY

A high aspect ratio wing is shown schematically in Figure 5.60 as confined within a cylindrical-pressure-specified interface. In contrast to the slender body case, the effect of the lift interference is more significant. Moreover, only two decks are in the flow. One of these is the classical "strip theory" inner (near field) region of lifting line theory in which each span station of the wing is in a two-dimensional flow independent of the others. As in the slender case, the basic flow is assumed to be given by a KG model, which differentiates it from the classical Prandtl lifting line theory for incompressible flow. For slightly subsonic freestream conditions, the outer (far field) region structure is that of a lifting line with a trailing vortex sheet in the Prandtl-Glauert (PG) subsonic linear regime. Downwash from this vortex assemblage changes the "geometric" wing incidence. Cook and Cole [40], obtained this correction by matching for the free field problem. Small [171], computed the solution of this problem for the case of "similar wing sections" in which all airfoil sections are affinely related along the span. Proper matching conditions for the interference case considered here were obtained from an integral equation based on Green's theorem using a special kernel involving a source reflected in a free jet cylindrical boundary. Further information on these developments is given in Malmuth [125], [123]. Pressure boundary conditions are incorporated into the model by a superposition procedure detailed in Malmuth [125]. For the latter, only the first few angular harmonics of Fourier means are important as well as the streamwise variations near the wing, in an asymptotic limit of span and wall height tending to infinity at the same rate. Matching, using the asymptotic solution of the non-linear integral equation, gives the induced downwash on the loaded line. The reflection effect arises naturally with use of the Green's function and can be interpreted to be phenomenologically the same as that for incompressible flow, *i.e.*, **inversion of the vortex system projection in the Trefftz plane into the wall/interface projection.** Non-linear corrections can be obtained systematically using this method. On implementing these ideas, the variational equation for the wall interference potential ϕ_1 is similar to that for slender bodies. This is a linear variational equation of mixed type whose variable discontinuous coefficients depend on the KG basic free field flow disturbance potential ϕ_0. Asymptotic developments leading to this structure are detailed in Malmuth [125] and lead to the following boundary value problem for the wall correction potential ϕ_1 for "classical" free jet and solid wall boundary conditions

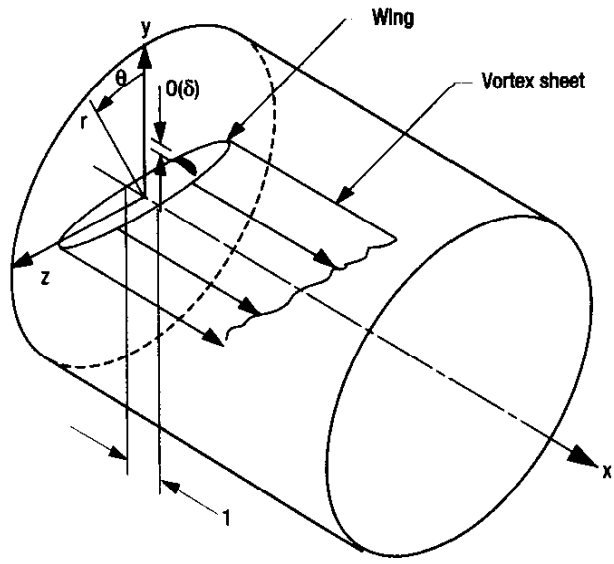

Figure 5.60 : Confined high aspect ratio wing

$$L[\phi_1] = \left(K - (\gamma+1)\phi_{0_x}\right)\phi_{1_{xx}} - (\gamma+1)\phi_{0_x}\phi_{1_x} + \phi_{1_{\tilde{y}\tilde{y}}} = 0$$

$$\phi_{1_{\tilde{y}}}(x,0) = 0; \quad \phi_1 \to -\tilde{y}[d(z)+w(z)] - [\Gamma_1(z)/2\pi]\theta + \cdots \text{ as } r \to \infty$$

$$[\phi_1]_{\text{wake}} = \Gamma_1(z) \equiv [\phi_1]_{\text{te}}.$$

Here, $d(z)$ and $w(z)$ are crucial functions controlling the size of the aspect ratio and wind tunnel corrections, respectively. They are given by the integrals

$$d(z) = \frac{1}{4\pi} \text{P.V.} \int_{-1}^{1} \frac{\Gamma_0'(\xi)}{x - \xi} d\xi$$

$$w(z) = \pm \frac{\mu^2}{4\pi} \text{P.V.} \int_{-1}^{1} \frac{\Gamma_0(\xi)}{\left(z\xi - \mu^2\right)^2} d\xi ,$$

where P.V. signifies that the principal value of the integral is to be taken. The function $\Gamma_0(z)$ is the spanwise circulation distribution along the wing in the free field basic flow. The quantity $w(z)$ was obtained from the previously indicated integral equation far field analysis detailed in Malmuth [125], the (+) and (-) apply to free jet and closed wall test sections, respectively, and μ is the test section width in units of the wing span. A derivation using Green's theorem and a Green's function for the geometry shown in Figure 5.61 is given for free jet wall boundary conditions in Malmuth [125], [123].

Details of the special numerical methods needed to solve the preceding boundary value problem and its analogue for the slender body wall interference case are contained in Malmuth [125], [123], which are generalisations of methods used by Small [171]. As a practical outgrowth of this theory procedures in which asymptotics can be integrated with pressure and wake measurements to correct for viscous effects in interference estimates are discussed in Malmuth [125], [123].

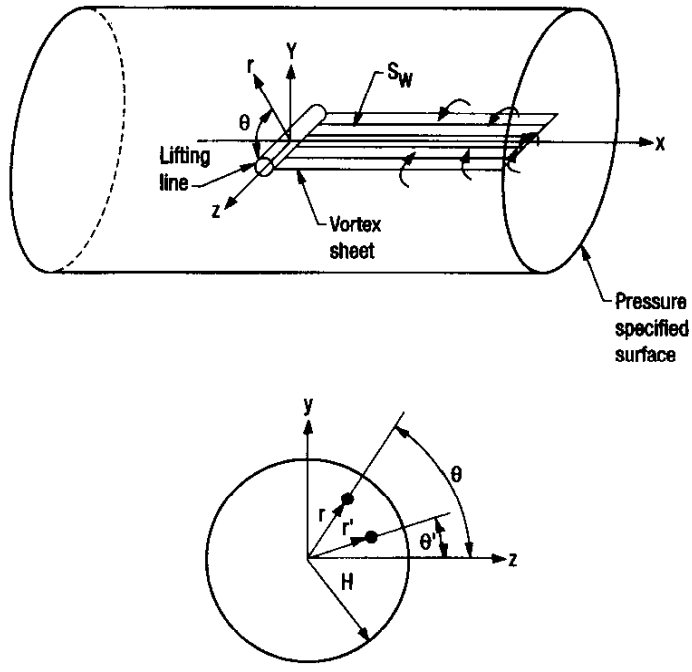

Figure 5.61 : Far field flow configuration showing lifting line and vortex sheet

5.4.5 Results - Small Slender Bodies

Calculations for confined slender bodies for which $H^{-1} = o(1)$ discussed in Malmuth, [121], [123], [125], show a spikelike interference pressure field as well as a change of interference drag to thrust as the Mach number approaches unity and show the intrinsic similitudes of the asymptotic theory which is consistent with those obtained by Goethert [71] using non-asymptotic procedures. The spikelike detail which diffuses with decreasing Mach number is also obtained for high aspect ratios since it is due to the translation of the shock from its free field position. **Since the boundary conditions (obtained from asymptotic matching) depend only on the streamwise area progression rather than the cross sectional shape of the body, an equivalence rule holds that states that the interference flow for asymmetric bodies is identical to those for their equivalent bodies of revolution in TSDST.** Although this argument is made here for the $H^{-1} = o(1)$ case, a more detailed analysis given in Section 5.4.8 shows that it holds for $H = O(1)$. Also indicated in Malmuth [121], [123], [125], is the resemblance of the pressure distribution away from the spike with that obtained by Malmuth [119], for incompressible flow. Another outgrowth of our analyses of these

slender body flows is the shock position invariance law reported in Wu [186], Cole and Malmuth [38], Malmuth [120].

5.4.6 Results - Large Aspect Ratio Wings

For high aspect ratio wings, free jet boundary conditions as well as pressure interface conditions such as

$$C_{P_I} = \varepsilon_2 e^{-|x|}\left(1 + \varepsilon_1 \cos\theta\right), \quad -\infty \le x \le \infty$$

having certain qualitative features of near-wall pressure distributions were considered, where C_{PI} = the interfacial pressure distribution, ε_1 and ε_2 are constants set to the value .2 for the calculations and $\mathrm{sgn}(x) = 1$ for $x > 0$ and -1 for $x < 0$. In Figure 5.62, results for an aspect ratio 8 elliptic planform having a NACA 0012 airfoil section are presented. The freestream Mach number M_∞ is .63 and the incidence α=2° for this subcritical case. If the three-dimensional wing has the same airfoil section along its span, (similar airfoil sections), the problem can be reduced to a two-dimensional one as shown in Malmuth, [125]. Effects of finite span and free jet wall interference on the chordwise pressures show the reduction of lift from both phenomena. Corresponding supercritical results for M_∞ =.75 at the same angle of attack are shown in Figure 5.63. The upstream movement of the shock is associated with the loss of lift that also occurs at this higher Mach number. Such behaviour is consistent with qualitative arguments concerning the fact that for proper imaging in the free jet boundary, the image vortex system outboard of a wingtip has the same sense as that around the wingtip. This therefore adds to the increased downwash associated with finite aspect ratio and reduces the angle of attack further. The assumed interface pressure gives the same effect in this example. Figure 5.63 shows an increase in the rate of re-expansion immediately downstream of the shock when the latter is weakened. This somewhat counterintuitive behaviour can be understood in terms of the singularity of Transonic Small Disturbance Theory discussed in Cole and Cook [37], and Gadd [65]. The trends in Figure 5.61 are supported by experiments and other calculations and are discussed more fully in Malmuth [125], [120]. The relevance of the experiments is that if the Reynolds number is sufficiently high, the post-shock expansion resembles that obtained from the inviscid predictions described in this review. (Smaller Reynolds numbers will result in post-shock boundary layer separation and are not germane to this discussion.)

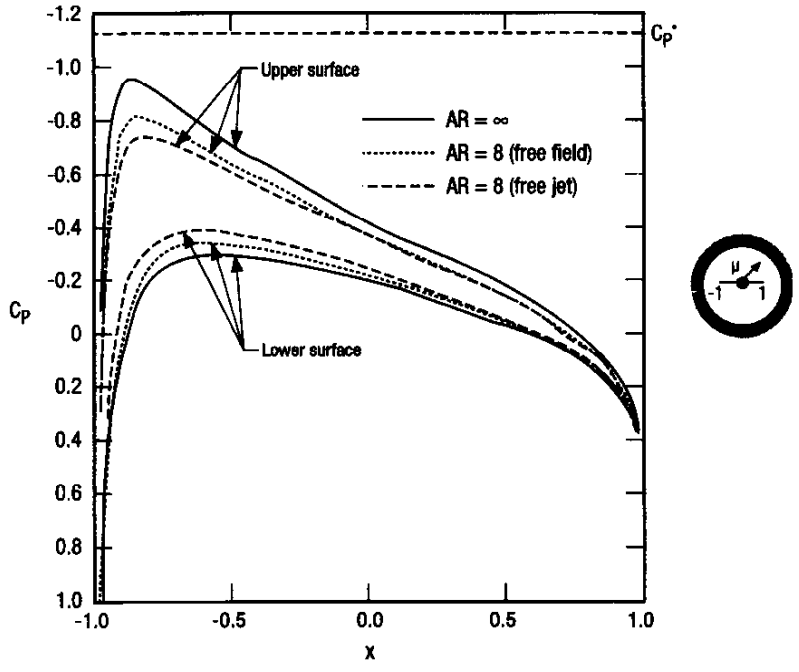

Figure 5.62 : Chordwise pressures on NACA 0012 wing, M = .63

In addition to the high aspect ratio cases shown, non-similar wings have been analysed. A normalising transformation that simplifies the computational problem has been discovered. Details of this transformation are discussed in Malmuth [125]. **An important result of the analysis is that with the renormalisations, the calculation can be reduced to the similar section calculation with the exception that the term $\phi_{0_x}\phi_{1_{xx}}$ in (1a) is no longer computed at** $z = 0$. In addition, the quantities d and w are used parametrically at each span station from a knowledge of $\Gamma_0(z)$, the spanwise loading of the zeroth order problem. This corresponds to a kind of strip theory. In order to obtain Γ_0, the semispan wing is divided into n span stations, and the zeroth order (KG) problem detailed in Malmuth [125] is solved at each. For the results to be presented, n was selected to be 5. Depending on the planform, some investigation is required to determine if this value provides a good enough approximation of the spanwise loading to obtain the ϕ_1 variational solution accurately. Chordwise pressure distributions on the swept wing (wing A) configuration of Hinson and Burdges (1980), [84], were computed at various angles of attack α, and Mach number M_∞. To achieve rapid convergence, the streamwise grid was clustered near the blunt leading edge.

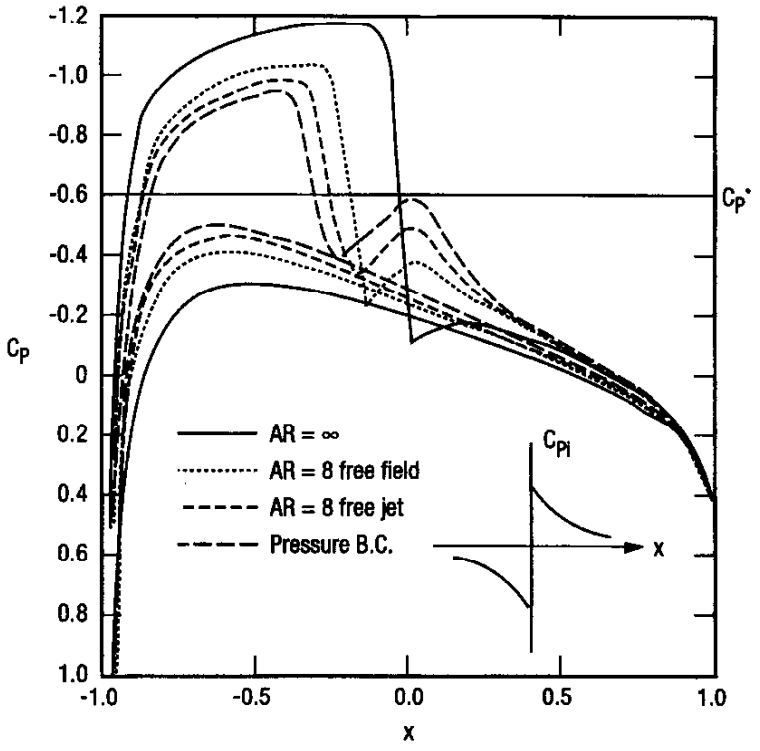

Figure 5.63 : Chordwise pressures on NACA 0012 wing, $M_\infty = .75$, $\varepsilon_1 = \varepsilon_2 = .2$

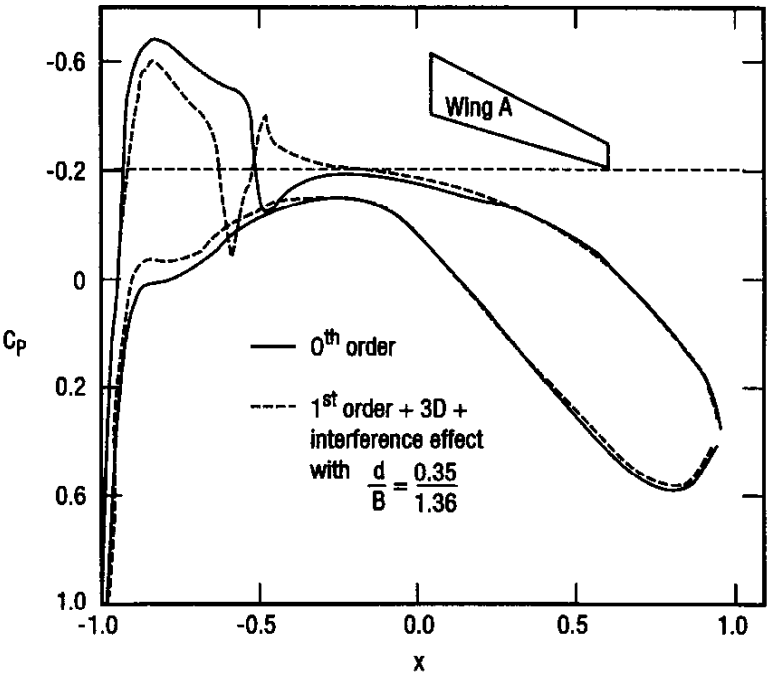

Figure 5.64 : Zeroth and first order chordwise pressure distributions on wing A, $\eta = .45$, $M_\infty = .76$, $\alpha = 0°$

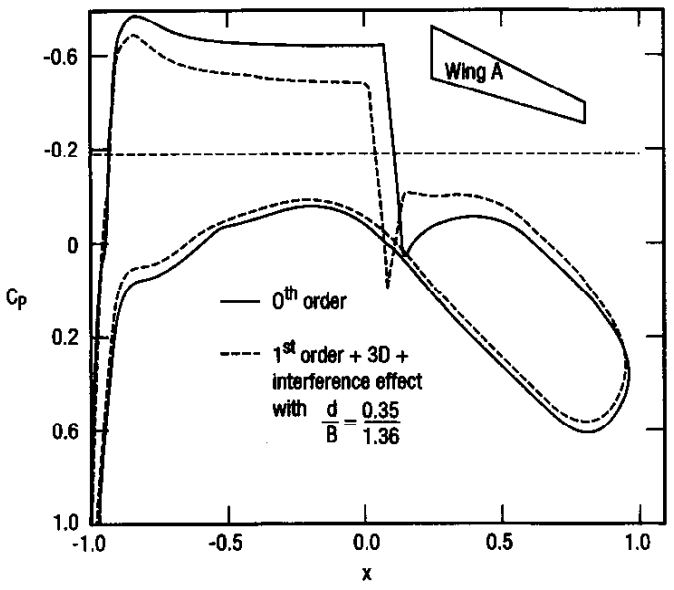

Figure 5.65 : Zeroth and first order chordwise pressure distributions on wing A, η = .5, M_∞ = .76, α = 1°

To demonstrate a typical calculation, Figure 5.64 and Figure 5.65 show the effect of wall interference and finite span corrections on the chordwise pressures of wing A at nearly midspan, and at two angles of attack. The largest corrections appear to be near the shock at $\alpha = 0^\circ$. By contrast, the more supercritical case corresponding to $\alpha = 1^\circ$ shows a greater extent of the corrections. For both incidences, they are most pronounced on the upper wing surface. In Cole and Cook [37], [40], modifications to the zeroth order KG boundary value problem are discussed for a yawed wing. The analysis shows that these changes occur in the far field for the three-dimensional first order perturbation flow and in both the far field and equations of motion for the second order flow. The high aspect ratio code is based on a theory not designed for swept wings. This is because the dominant approximation of the inner flow assumes that all spanwise stations are approximately two-dimensional. If a discontinuity occurs in the slope of the leading edge, a local three-dimensional flow occurs, nullifying this assumption. Such discontinuities occur at the root apex and tips of swept and other kinds of planforms. More general cases are cranked shapes. Asymptotic procedures are under consideration to treat these corner flows and involve "canonical" numerical problems for the non-linear flow near the corner. These canonical problems remain the same for planform changes away from the corner. In spite of this limitation, it was of interest to assess the correctability of the wing A results using the zeroth order code. Figure 5.66 and Figure 5.67 indicate chordwise pressure comparisons of our zeroth order code with data from Hinson and Burdges [84]. In both figures, the effective tunnel Mach number and angle of attack were modified to match the data. The similarity of the pressure distributions suggests the correctability of the test data. The sweep effect delaying supercriticality is evident and is not reflected in the unswept lifting line forming the basis of the present analysis. In Figure 5.66, the influence of shock-boundary layer interaction is not as great as in Figure 5.67. Results showing effective treatment of viscous effects are reported in Malmuth [125]. These

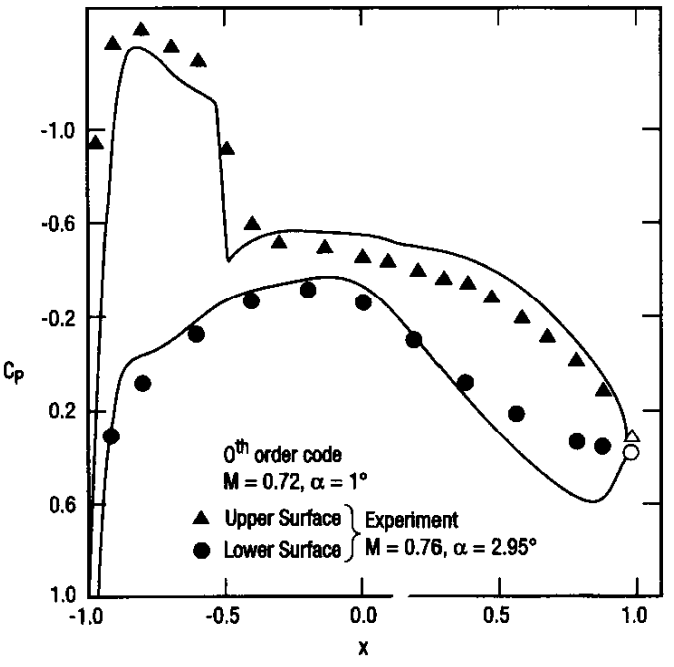

Figure 5.66 : Comparison of theoretical and experimental chordwise pressures for wing A, η = .5, tested at M_∞ = .76, α = 2.95°

calculations which use an interactive boundary layer model based on Green's lag entrainment method suggest that the effective increment in K associated with the combined Mach, angle of attack corrections used in Figure 5.66 and Figure 5.67 can be reduced if viscous interactions effects are systematically incorporated. In comparisons such as Figure 5.66 and Figure 5.67, what needs to be analysed are the combined effects of sweepback and viscous interactions on the interference. In Malmuth [125], the similarity parameter K was allowed to vary from the zeroth order flow to the first order wall interference flow. This flexibility should be investigated with the aim of systemising the corrections that can be obtained through studies of the type associated with Figure 5.66 and Figure 5.67. The variation of K is expressed in a perturbation form related to the asymptotic expansion of the perturbation potential ϕ. This perturbation gives the flexibility of varying the tunnel Mach number and geometric angle of attack to correct or simulate free field conditions.

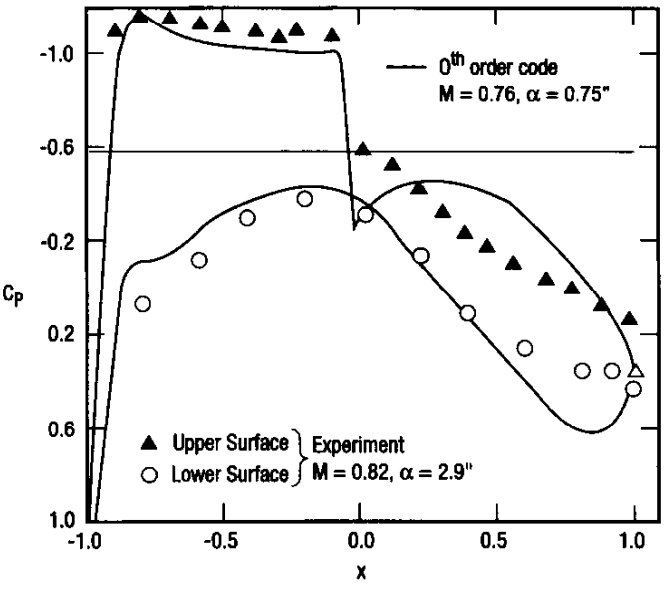

Figure 5.67 : Comparison of theoretical and experimental chordwise pressures for wing A, η = .5, tested at M_∞ = .82, α = 2.9 °

5.4.7 Lift Interference and Porous Wall Effects on Slender Wings

A current thrust of the CAN methodology is to develop a systematic asymptotic framework for computation of lift corrections due to the interaction of a slender model with walls. Strong theoretical evidence exists that the restrictions of slenderness are elastic so that lift corrections for slender shapes can be applied to not-so-slender-shapes. Because of the resemblance of the asymptotic developments to those for transonic flow, the subsonic case was considered for convenience. As indicated later, this approach actually seemed to provide good comparison with experiment at near-sonic speeds.

Initial developments are described in Malmuth, Neyland and Neyland [124]. There, the free field and wind tunnel problem of the incompressible flow over a flat wing of arbitrary planform in a circular wind tunnel test section was outlined. An in-depth continuation of that introductory treatment will be summarised in what follows: Malmuth and Cole [118] used expansions of limit process type to study the matching process in greater detail than in the preliminary analysis of Malmuth, Neyland and Neyland [124], as well as to derive a second order inner approximation.

Letting Φ be the velocity potential, limits involving the semispan of the wing b and the angle attack α have been considered. Near the wing, a limit process in which $b \to 0$ is used. Referring to Figure 5.68, an inner limit is defined as

$$\frac{\Phi_{inner}}{U} = x + ab\varphi_1(x, y^*, z^*) + ab^3 \log\frac{1}{b}\varphi_{21}(x, y^*, z^*) + ab^3\varphi_2 + \cdots \qquad (5\text{-}20)$$

where the inner limit is

$$a = \tan\alpha,\ A = \alpha / b,\ y^* \equiv y / b,\ z^* \equiv z / b,\ \text{fixed as } a, b \to 0 \qquad (5\text{-}21)$$

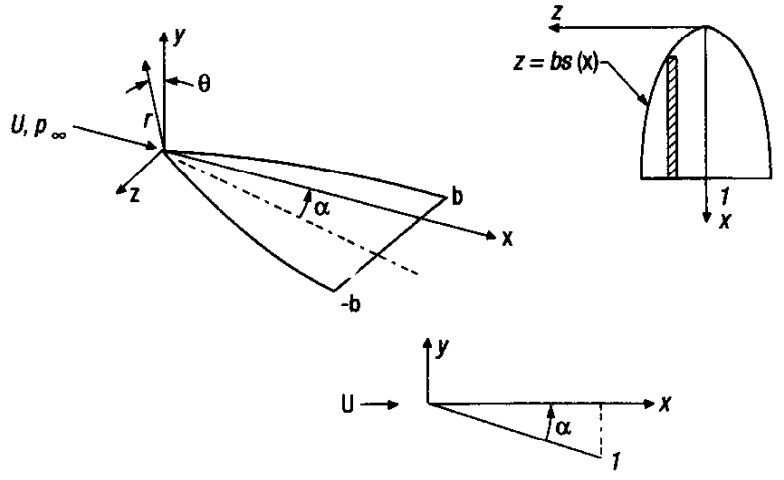

Figure 5.68 : Schematic of slender wing

In (5-21), the characteristic wing chord is fixed while the semispan b and angle of attack α tend to zero at the same rate. Near the wing, cross flow gradients dominate and these parameters give the characteristic lateral scale of the flow which is b. Equation (5-20) is an inner expansion for the velocity potential Φ in terms of approximating perturbation potentials φ_ν, (ν = order of the approximation). It contains the "switchback" term φ_{21} and the indicated gauge functions in anticipation of matching.

As detailed in Malmuth and Cole [122], the problems for the φ_ν are obtained by substituting the asymptotic developments into the exact problem for Φ. The dominant orders in (5-20) solve harmonic boundary value problems in the cross plane perpendicular to the freestream and the higher orders solve Poisson problems.

The dominant inner approximation provides a first estimate for the flow and pressure field of the wing. The leading edge square root singularities dominate this flow field which is the stagnating flow on a finite flat plate. From a Joukowski mapping to the circle plane or the Circle Theorem, the solution of the dominant problem is

$$\varphi_1 = -i\,\mathrm{Re}\left\{\left[\sigma^2 - s^2\right]^{1/2} - \sigma\right\} \quad \sigma \equiv z^* + i(y^* + Ax) \qquad (5\text{-}22)$$

in which the freestream velocity has been normalised to unity through the non-dimensionalisations in (5-20). This solution has the proper far field (downwash at infinity) related to matching with outer solution.

A similar procedure gives

$$\varphi_{21} = -\,\mathrm{Re}\frac{i}{2}(ss')'\sqrt{\sigma^2 - s^2}\ . \qquad (5\text{-}23)$$

Refinements of the unconfined flow field and wall interactions come from coupling with the far field. An outer expansion involving an $O(1)$ transverse length scale as $b \to 0$ gives a semi-infinite line doublet for this part of the flow. In particular, for an outer limit

$$x, y, z, A \ \text{ fixed as } a, b \to 0,$$

the appropriate outer expansion is

$$\frac{\Phi_{\text{outer}}}{U} = x + ab^2\phi_1(x,y,z)+\cdots. \tag{5-24}$$

The solution ϕ_1 can be written as

$$\phi_1 = -\frac{1}{4\pi}\frac{\partial}{\partial y}\int_0^\infty \frac{D(\xi)d\xi}{\sqrt{(x-\xi)^2+r^2}} + \text{wall correction function} \tag{5-25}$$

where the first term is a line doublet distribution of strength D(ξ) that satisfies an approximation of the classical Darcy law boundary condition. The wall correction function is needed to satisfy Darcy's law. In (5-25), the Kutta condition at the effective trailing edge provides the appropriate continuation of the line doublet to downstream infinity and its convergent integral representation. Furthermore, (5-25) gives upstream influence not present in the inner solutions.

The inner expansion of (5-25) can be obtained from the $r \to 0$ expansion of its Fourier transform. This gives

$$\phi_1 \cong \frac{D(x)}{2\pi}\frac{\cos\theta}{r} - \frac{D''(x)}{2\pi}\left\{\frac{r}{2}\log r - \frac{r}{4}\right\}\cos\theta - G''(x)\frac{r}{2}\cos\theta + my + \cdots \text{as } r \to 0$$

where

$$my \equiv \cos\theta\left\{\frac{D(x_T)r}{2h^2}\lambda - \frac{r}{2\pi h^2}\int_0^{x_T} D'(\xi)d\xi \int_0^\infty q\left[\frac{\beta^2(K_0q+K_1)(I_1-qI_0)+q^2I_1K_1}{\beta^2(qI_0-I_1)^2+q^2I_1^2}\right]\sin\frac{q(x-\xi)}{h}dq\right\}$$

$$-\cos\theta\left\{\frac{\beta r}{2\pi h^2}\int_0^{x_T} D'(\xi)d\xi \int_0^\infty \frac{q^2}{\beta^2(qI_0-I_1)^2+q^2I_1^2}\cos\frac{q(x-\xi)}{h}dq\right\}$$

$$\lambda = \ 1 \text{ for } \beta \neq 1, \text{ (includes porous and closed walls)}$$
$$= -1 \text{ for } \beta = 0, \text{(free jet), (degenerate limit } \beta \to 0) \tag{5-26}$$

$$G(x) \equiv -\frac{1}{4\pi}\int_0^1 D'(\xi)\,\mathrm{sgn}(x-\xi)\log 2|x-\xi|d\xi$$

$$D(x) \equiv \frac{s^2(x)}{2}\alpha$$

where h is the wall height in units of the body length, β is the Darcy constant, $s(x)$ is the local semispan and the term my in (5-26) is the wall interaction effect due to the imaging of the doublet in the walls. As an alternate approach for the first term of (5-25), the integral can be directly expanded for $r \to 0$. This delicate procedure is described in Kevorkian and Cole [105]. In the Fourier integral method used, the solution naturally decomposes into a free field (no walls present part) and a wall interaction portion as indicated in (5-26). Special limiting processes of the singular integrals were developed to handle zero and infinite porosity, corresponding to solid wall and free jet cases respectively. Equation (5-26) agrees with the results from Pindzola and Lo [151], Goodman [72], and Baldwin [16], in the limit of vanishing chord to tunnel radius ratio. Extensions of our asymptotic procedure can be used to compute the **camber effect** associated with non-vanishing chord. To our knowledge, this study has not been made and we believe it is an important factor entering the comparison of our results with experiment to be discussed.

The inner and outer solutions match directly as shown in Malmuth and Cole [118], to the orders in (5-20). This can be shown by expressing each in terms of an intermediate variable r_η. For this purpose, an intermediate limit

$$r_\eta \equiv \frac{r}{\eta(b)} \text{ fixed as } b \to 0, \tag{5-27}$$

is used to compare the inner and outer representations in an "overlap domain" $r_\eta = O(1)$ in which both expansions are mutually valid. Note in the intermediate limit

$$r^* = \frac{\eta r_\eta}{b} \to \infty, \; r = \eta r_\eta \to 0, \frac{\eta(b)}{b} \to \infty, \; \eta(b) \to 0.$$

The matching process consists of writing inner and outer expansions in terms of the intermediate variable r_η and comparing similar terms to determine unknown elements as detailed in Malmuth and Cole [118].

The essential wall interference effect is the additive term m from (5-26) affecting the matching. Another viewpoint is that the solution of which consists of a superposition of its homogenous solution (response to homogenous equation of motion and boundary conditions) and the effects of the forcing terms in the equation of motion and boundary conditions. The homogeneous solution is non-trivial because of the downwash far field associated with the line doublet imaging in the porous walls. Another interesting point is the surprising appearance of switchback terms. These normally are associated with transonic flow. They arise in this subsonic flow from logarithmic elements in the expansions.

Integration of the pressures on the wing gives the following expressions for the lift L. For the free field,

$$\frac{L}{\rho U^2} = b^2 \tan\alpha \, \ell_1 + b^4 \log\frac{1}{b} \tan\alpha \, \ell_{12} + b^4 \tan\alpha \, \ell_2 + \cdots \tag{5-28}$$

where

$$\begin{aligned} \ell_1 &= \int_1^1 [\varphi_1] dz^* = \pi \\ \ell_{12} &= \int_1^1 [\varphi_{12}] dz^* = \tfrac{\pi}{2}(ss')'_{x=1} \\ \ell_2 &= \int_1^1 [\varphi_{21}] dz^* = (\ell_{12}/2)(1+\log 2) - \tfrac{\pi}{2}(G''_{TE} + s'^2{}_{TE} + A^2) \end{aligned} \tag{5-29}$$

where G is an integral that involves the span function $s(x)$ and its derivatives and $_{TE}$ signifies the trailing edge. The dominant term for the lift ℓ_1 and pressure distribution agrees with Jones' (1946), [89], theory and a detailed analysis of Wang [181] who did not study wall interference.

As an experimental validation of the lift interference theory, Figure 5.69 compares lift versus angle of attack predicted by our asymptotic theory with transonic tests of a wing-body combination at TsAGI in Moscow and reported in Malmuth, Neyland and Neyland [124]. It is striking that the incompressible theory agrees so well with the experiment for the high transonic Mach numbers $M = .99$ and 1.02 tested. Plausibility of this finding is related to the elasticity of slender wing theory to not-so-slender planforms as $M \to 1$ as discussed in Cole and Cook [37], and Adams and Sears [1].

Approximations of wall interaction integrals give the porous wall corrections for wall openness factors f = 2 and 10% indicated in the figure. It shows that the experimental trend with increasing f is captured by the lift interference theory for vanishing chord to tunnel radius ratio. However, the comparison with the data shows an increasing slope with incidence not captured by the first order theory. Preliminary indications are that the free field second order effect shows a reduction in lift slope that is counter to experimental evidence. It is likely that the reverse trend is due to leading edge viscous separation and vortex formation as well the need to account for the finite chord of the wing. A refinement accomplished is an estimate of the effect of a vortex at the wing-fuselage juncture occurring at higher angles of attack.

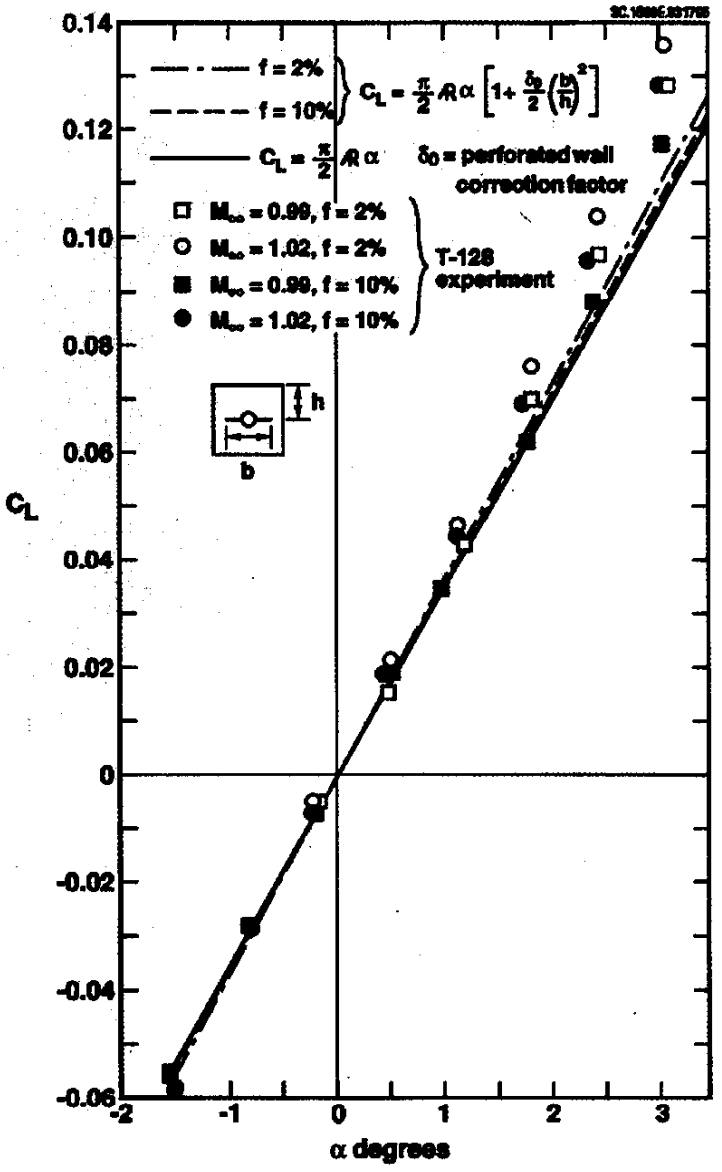

Figure 5.69 : Comparison of lift interference theory with TsAGI experiment

An oil flow visualisation of this phenomenon from our Russian TsAGI experiment reported in Neyland and Neyland [144], is shown in Figure 5.70. Results from a preliminary model based on conical invariance of the vortex field is shown in Figure 5.71. The improvement in agreement is striking and suggestive of the importance of modelling discrete vortex effects. In spite of these, the wall interaction theory shows promise of modelling **relative** trends. As in the blockage theory work for wall height of the order of the body length to be discussed, estimation of the **absolute** levels can be improved independently of the interference estimations using vortex dynamic and leading edge separation approaches such as those just mentioned.

The main point of the previously discussed subsonic asymptotic framework is that it provides a natural launching pad for extension of the theory to non-linear transonic flow, accounting for higher approximations, thickness, viscous interactions and finite chord to tunnel height as well as systematic higher order refinement. With the exception of switchback terms and gauge functions, the inner problems for the transonic case are expected to resemble those associated with the incompressible asymptotic theory. However, the outer expansions will solve the three-dimensional Karman-Guderley instead of Laplace equation in the dominant approximation, and forced versions in the higher orders. However, a major simplifi-

cation of the usual lifting surface (transonic small disturbance theory) numerical problem is anticipated since the angular variation can be separated out by matching with the inner multipole structure.

Figure 5.70 : Wing-body-juncture vortex formation in TsAGI wind tunnel

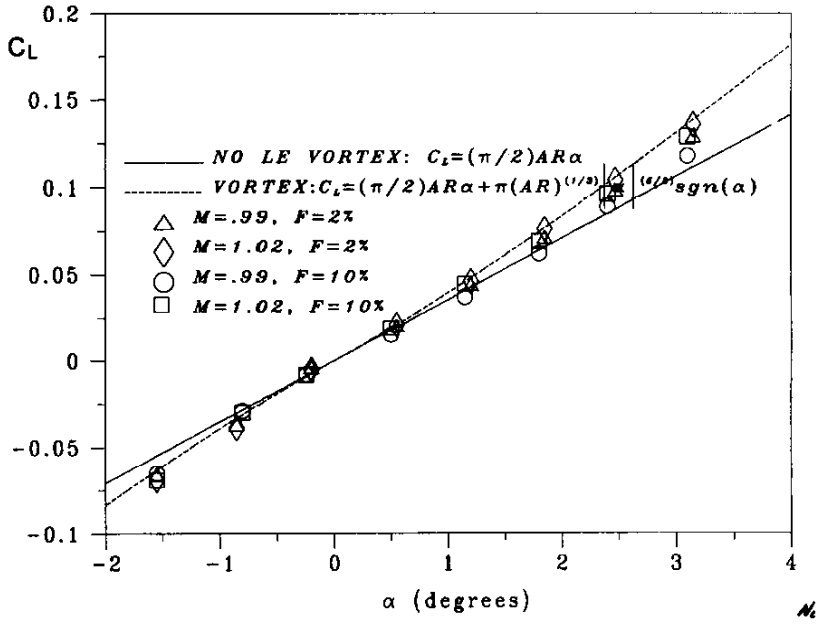

Figure 5.71 : Comparison of vortex improved theory with experiment

5.4.8 EXTENSION OF LARGE WALL-HEIGHT BLOCKAGE INTERFERENCE THEORY TO MODERATE WALL HEIGHT CASE

This section will deal with

1. Validating a transonic small disturbance baseline model for the flow in a wind tunnel against experimental data
2. Validating the equivalence rule for transonic wall interference

Referring to Figure 5.72, the walls or pressure interface boundary where pressures are assumed to be specified from experiment are at $r = h$, where h is assumed constant for convenience herein (circular test section).* Defining $H = \delta\, h$, the case $(i)\ H = O(1)$ was considered, in contrast to the less practical situation (*ii*) described previously where $H \to \infty$. As indicated in Malmuth and Cole [118], the asymptotic solution of the Full Potential formulation, for Case (*i*) leads to two, rather than three decks associated with (*ii*), *i.e.*, no wall layer is required, the confined flow consisting only of a nearly axisymmetric "outer" region and a cross flow gradient-dominated inner core which is the near field of the body. In an inner limit in which

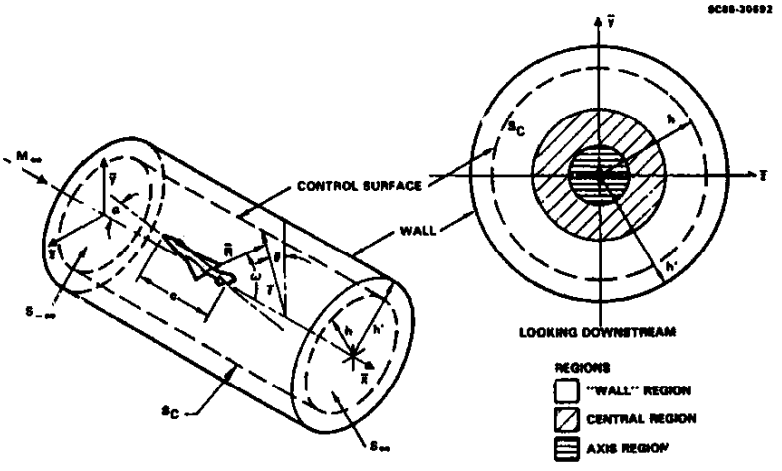

Figure 5.72 : Schematic of confined slender aeroplane

$$r^* \equiv r/\delta\ ,\ K \equiv \left(1 - M_\infty^2\right)/\delta^2,\ A \equiv \alpha/\delta \ \text{ fixed as}\ \delta \to 0, \tag{5-30}$$

where α is the angle of attack, δ is the maximum thickness ratio of the equivalent of body of revolution and M_∞ is the freestream or tunnel Mach number which will correspond for convenience to the flight Mach number. The inner expansion (near field) of the slender aeroplane model $B = r - \delta F(x,\theta) = 0$ is

$$\frac{\Phi_{\text{inner}}(x,r,\theta\,;M_\infty,\delta,\alpha)}{U} = x + \left(2\delta^2 \log\delta\right) S_1(x) + \delta^2 \varphi_1(r^*,\theta\ ;x) + \cdots \tag{5-31}$$

where $S_1(x)$ is a source strength determined by matching with the outer solution.

The outer limit is

$$\tilde{r} \equiv \delta r,\ K \equiv \left(1 - M_\infty^2\right)/\delta^2,\ A \equiv \alpha/\delta \ \text{ fixed as}\ \delta \to 0. \tag{5-32}$$

For (5-32), the appropriate outer expansion is

$$\frac{\Phi_{\text{outer}}(x,r,\theta\,;M_\infty,\delta,\alpha)}{U} = x + \delta^2 \phi_1(x,\tilde{r},\theta\ K,A) + \cdots \tag{5-33}$$

*All lengths are in units of the body length.

Malmuth and Cole [118] use these expansion procedures to obtain to the extension of our transonic area rule for wall interference (TARWI) from $H \to \infty^*$ to $H = O(1)$. From this generalisation, more practical situations than those for $H \to \infty$ can be considered in which the model distance from the walls is of the order of its length. These are typical of transonic testing. It should be noted that angle of attack effects are higher order for this $A = O(1)$ case as contrasted to $A \to \infty$ cases where they will interact with the near field in the dominant orders through line doublet-wall-imaging/reflection-induced downwash.

5.4.9 Validations of Theoretical and Computational Simulations for Moderate Wall Height Case

Experiments in TsAGI's T-128 wind tunnel in Moscow, Russia, described in Malmuth, Neyland and Neyland [124], have been performed to validate the previous theoretical developments. Figure 5.73 and Figure 5.74 show one of the wing-body configurations tested. Results for pressures over the equivalent body of revolution (EBR) for this wing body are shown in Figure 5.75 which compares the combined asymptotic and numerical method exemplified by Malmuth *et al.* [123], [125], and Malmuth and Cole [118], with the TsAGI experiments for the $H=O(1)$ case discussed in the previous section.

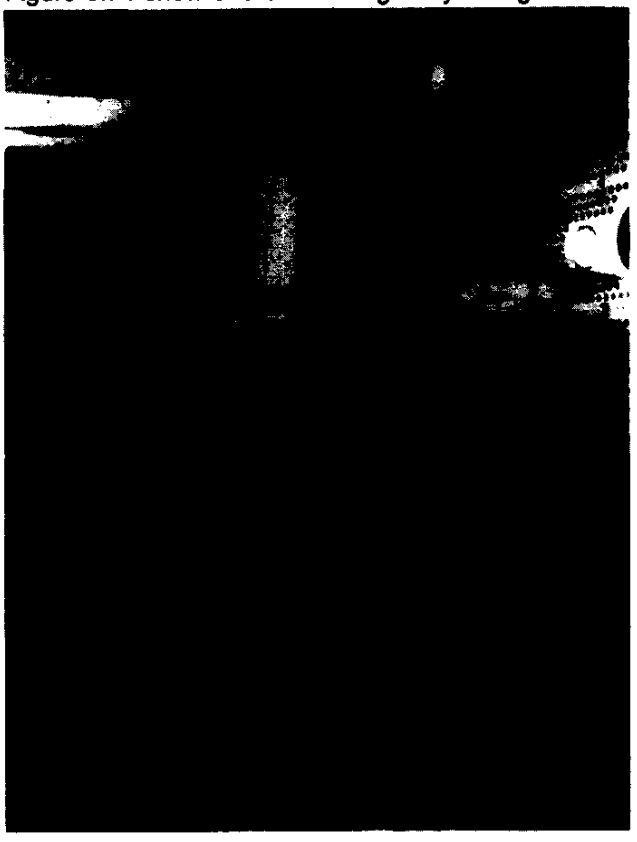

Figure 5.73 : Wing-body WB1 tested in TsAGI T-128 wind tunnel

The code is quite efficient, requiring only a minute of execution time on a VAX 3100 work station and only 100 iterations to obtain the 2000 iteration fully converged solution. Figure 5.75 shows excellent agreement between the theory and experiment. To achieve this fidelity, it was important to accurately simulate the sting model support. This element was necessary to capture the proper recompression process to ambient levels. Additional validations discussed in Malmuth, Neyland and Neyland [124] are that the shock position estimates from Wu [186], Cole and Malmuth [38], and Malmuth [120], agree well with the TsAGI measurements. Work continues on specially designed experiments to adjust the level of interference by altering the wall porosity. This will provide a useful database for comparison with the $H=O(1)$ theory.

* Enunciated in [125]

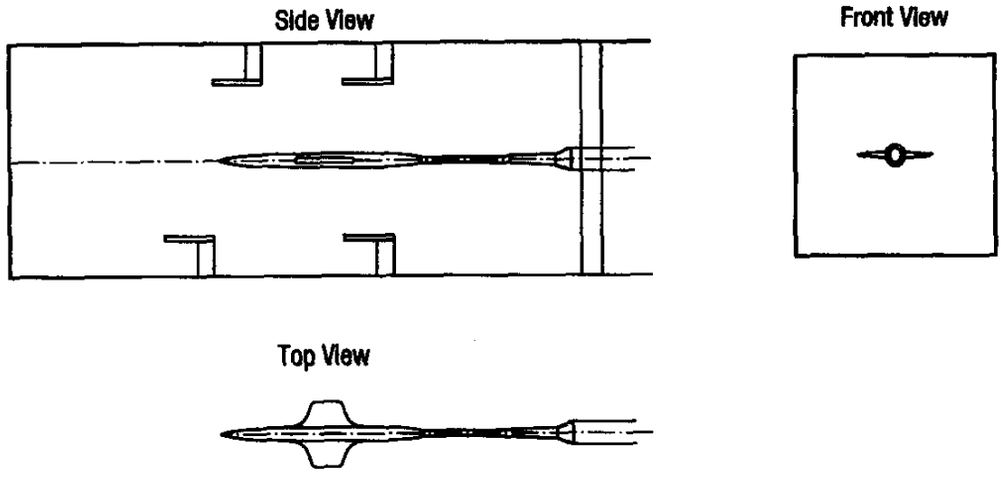

Figure 5.74 : WB1 three-view

A comparison of the larger aspect ratio wing-body with a smaller version is shown in Figure 5.76. Figure 5.77 and Figure 5.78 compare the drag rise of the smaller and larger aspect ratio wing body WB1 and WB2 respectively with their equivalent bodies EB1 and EB2 for two different wall porosities. These are

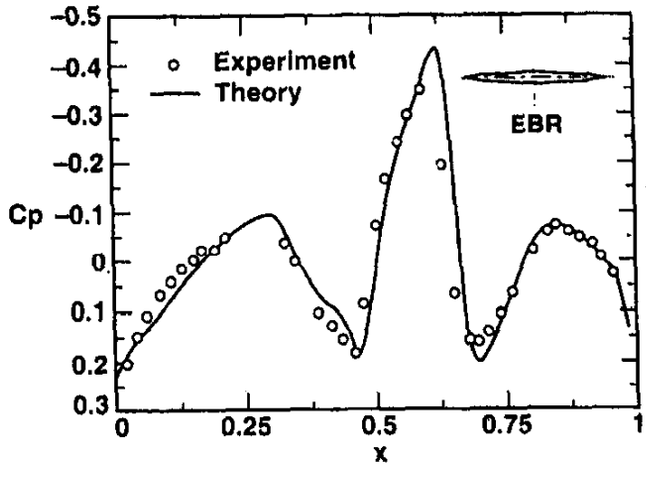

Figure 5.75 : Comparison of present theory with TsAGI experiment

expressed in terms of the wall openness area ratio, f , which is the area of the wall perforations as a percentage of the test section cross section area. Values of f were 2 and 10% for this study. Figure 5.77 and Figure 5.78 are, to our knowledge, the first experimental confirmation of the transonic area rule for wall interference (TARWI) previously discussed, *i.e.*, if

$$\Delta C_D \equiv C_D\big|_{f=10\%} - C_D\big|_{f=2\%}, \qquad \text{then}$$

$$\Delta C_D\big|_{WB} = \Delta C_D\big|_{EBR} \quad \bullet \qquad (5\text{-}34)$$

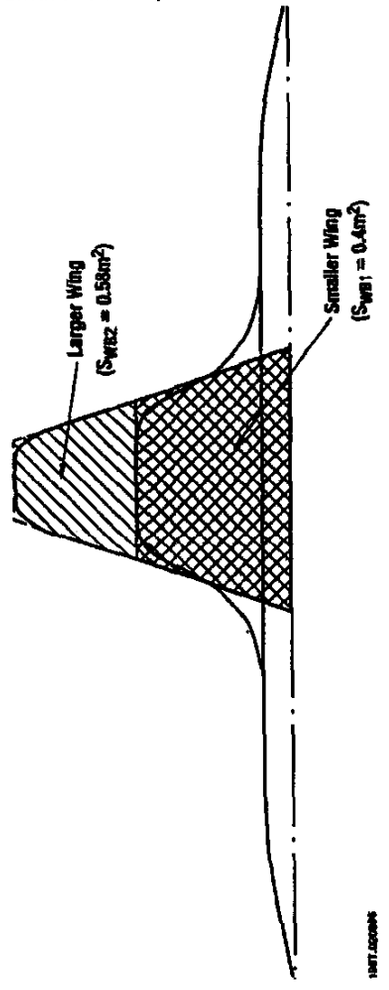

Fig. 5.76: Wing-body configurations tested

where C_D is the drag coefficient, subscripts WB and EBR denote the wing-body and its equivalent body respectively. Figure 5.78 shows the TARWI (5-34) has surprising robustness, *i.e.*, although the aspect ratio of WB2 is considerably larger than WB2, the TARWI (5-34) still holds near $M_\infty = 1$. This is related to the elasticity of slender body theory to not-so- slender shapes near sonic speeds. It is associated with the coefficient of the x derivative terms in the KG equation (28) being proportional to M_{local} -1 as $M_\infty \to 1$, where M_{local} is the local Mach number. Thus, although the cross flow gradients are no longer $O(1/\delta)$ but $O(1)$ for not-so-slender shapes such as WB2, the x derivative terms are still higher order. Accordingly, the near field remains harmonic in cross flow planes as in the classical slender body theory. Other robustness of (5-34) should also noted. Although (5-34) is applicable to $H = O(1)$, the *nominal* H is closer to 0.1 for the Figure 5.77 and Figure 5.78 cases. This is related to the larger length body associated with inclusion of the sting in its definition for the computational modelling. However, if a large part of the sting is at nearly ambient conditions, $H = O(1)$ rather than the nominal $H = o(1)$.

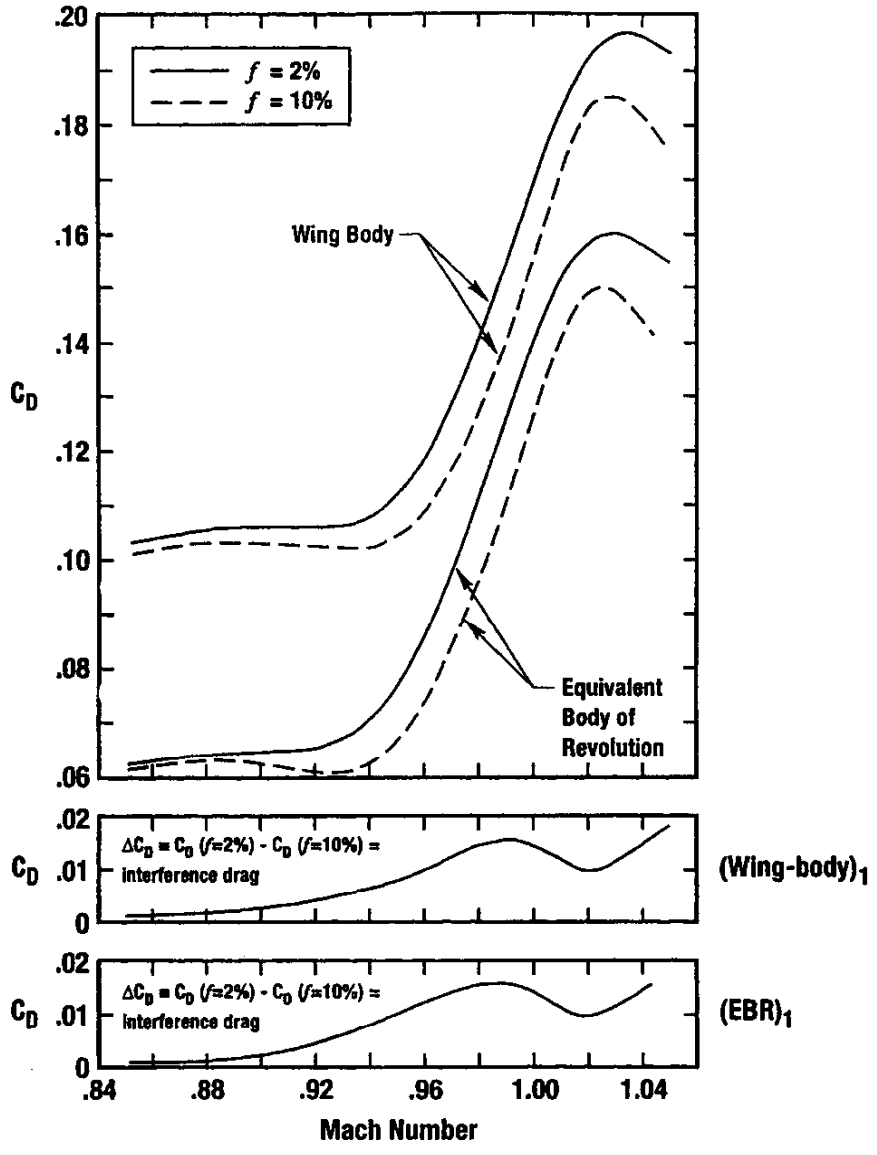

Figure 5-77 : Comparison of wave drag for wing-body WB1 and its equivalent body EBR1

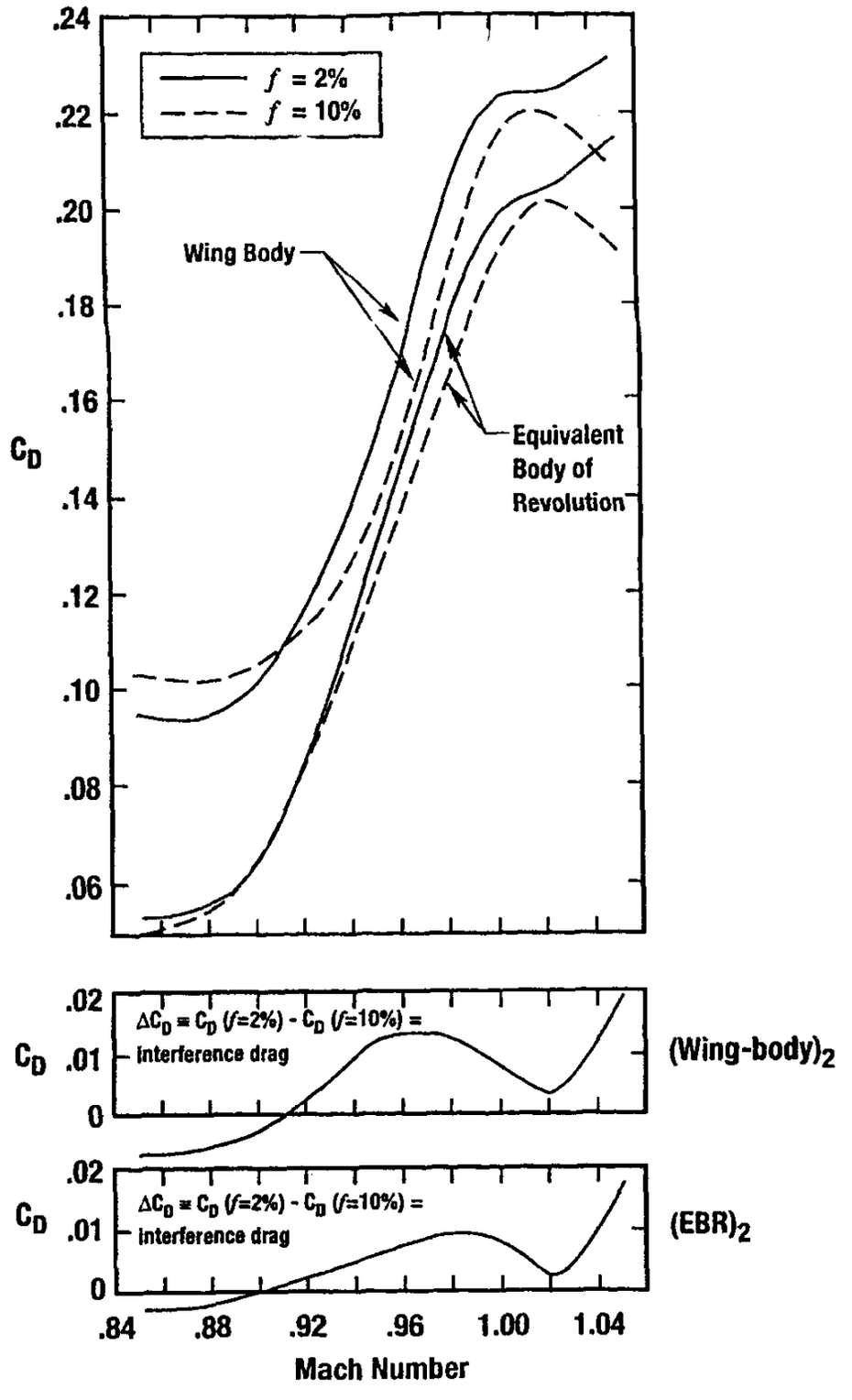

Figure 5-78 : Comparison of wave drag for wing-body WB2 and its equivalent body EBR2

5.4.10 NON-CIRCULAR WIND TUNNEL SECTIONS

Many wind tunnel test sections are non-circular. Typical U.S. installations have octagonal and rectangular test sections. Our testing in the T-128 wind tunnel strongly suggests that these non-circular cross sections have only a mild influence on the axisymmetric far field of a slender model tested at transonic Mach numbers. This observation motivated the theory to be described.

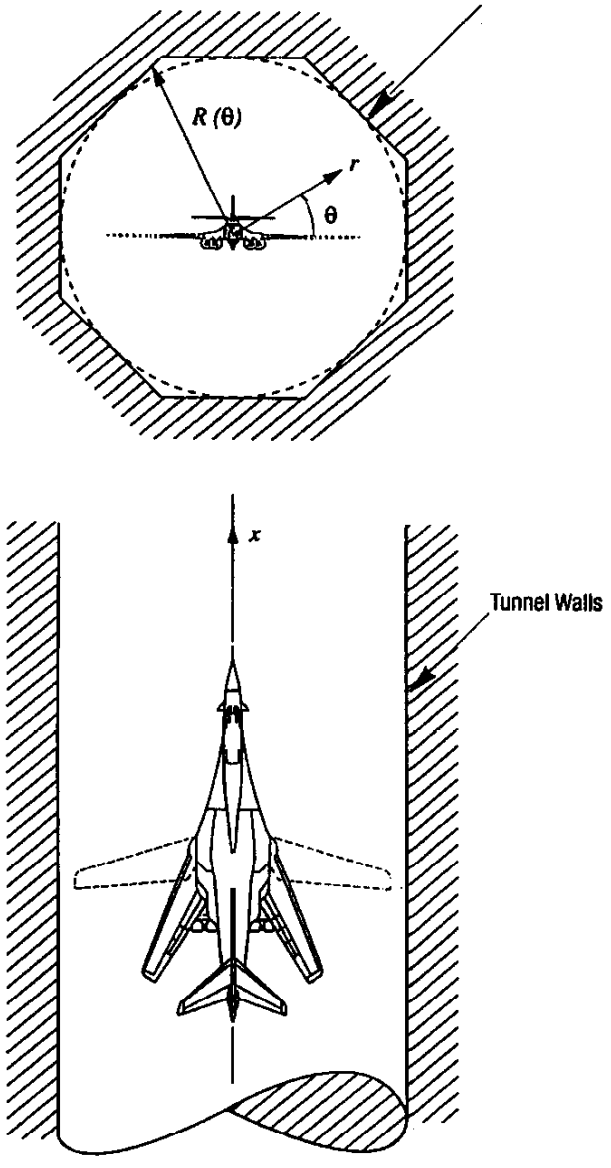

Figure 5-79 : Schematic of model in non-circular test section

If the flow near the walls is subsonic, which is the case in transonic flow with a subsonic freestream, it is reasonable to expect rapid elliptic decay of the disturbances inward toward the centreline of the wind tunnel. This contrasts to Group 2 and 3 cases such as slightly supersonic freestreams, near choking and supersonic bubbles of the unconfined flows penetrating the walls. To explore this hypothesis, the flow inside a test section that is a slight perturbation of circular section will be treated. Figure 5.79 shows an example of such as perturbation which is an octagon. For generality, the following wall shape,

$$R = h + \varepsilon g(\theta) \tag{5-35}$$

in which $\varepsilon << 1$ and h is a constant. For specific shapes, it is possible to get an approximate numerical order of magnitude for ε which can be written as

$$\varepsilon = \frac{g_{\max}{}_{0\le\theta\le\frac{\pi}{2}} - g_{\min}{}_{0\le\theta\le\frac{\pi}{2}}}{h} \tag{5-36}$$

Values of ε for square, hexagonal and octagonal test sections are given in Table 1.

Table 1

Section	n	ε
square	4	.414
hexagon	6	.155
octagon	8	.082

These are based on the following relations for an n-sided polygon:

$$\frac{g}{h}=\frac{\sec\left(\theta-\frac{2k\pi}{n}\right)-1}{\sec\left(\frac{\pi}{n}\right)-1},\quad k\frac{\pi}{4}\le\theta\le(k+1)\frac{\pi}{4},\quad k=1,2,3,\ldots,n, \tag{5-37}$$

$$\varepsilon=\sec\left(\frac{\pi}{n}\right)-1. \tag{5-38}$$

In the first quadrant,

$$k=0,1,2,3,\ldots,n/4,\ 0\le\theta\le\pi/2.$$

Using the polar co-ordinates previously introduced and referring to Figure 5.79, as well as the outer limit (5-32) and expansion (5-33) as well dropping the subscript unity notation in ϕ_1, the equation for the perturbation potential in the outer region is

$$\left(K-(\gamma+1)\phi_x\right)\phi_{xx}++\tilde{r}^{-1}\left(\tilde{r}\phi_{\tilde{r}}\right)_{\tilde{r}}+\tilde{r}^{-2}\phi_{\theta\theta}=0. \tag{5-39}$$

For convenience, a free jet boundary condition is considered. Accordingly, the exact boundary condition

$$C_p(x,R(\theta))=0$$

implies

$$\phi_x(x,R,\theta)=0.$$

Since R is independent of x,

$$\phi(x,R,\theta)=\text{constant}. \tag{5-40}$$

The constant can be assumed to be zero without loss of generality. Corresponding to (5-35), the perturbation potential ϕ can be decomposed into the axially symmetric outer part corresponding to $\varepsilon = 0$ and the secondary perturbation associated with the deviation of the walls from a circular cross section. Thus,

$$\phi(x,\tilde{r},\theta)=\phi_0(x,\tilde{r})+\varepsilon\phi_1(x,\tilde{r},\theta)+\ldots \tag{5-41}$$

A Fourier decomposition to reduce the three-dimensional Transonic Small Disturbance (TSD) problem for a wall perturbation from cylindrical to one in two dimensions is

$$\phi_1=\sum_{n=0}^{\infty}\phi_{1_n}(x,\tilde{r})\cos n\theta. \tag{5-42}$$

This decomposition exploits the fact that the only way that asymmetry is introduced into the perturbation problem is through the multiplicative factor $g(\theta)$ in (5-35). Note also that the assumption of small perturbations allows the boundary conditions to be transferred from the perturbed surface to the simpler cylindrical test section's. This is essential to the reduction of the dimensionality of the problem. Equation (5-42) is a **factorisation** that reduces the problem P1 to the form

$$\left\{K-(\gamma+1)\phi_{0_x}\right\}\phi_{1n_{xx}}-(\gamma+1)\phi_{1n_x}\phi_{0_{xx}}+\frac{1}{\tilde{r}}\left(\tilde{r}\phi_{1n_{\tilde{r}}}\right)_{\tilde{r}}-\frac{n^2}{\tilde{r}^2}\phi_{1n}=0 \tag{5-43}$$

$$\lim_{\tilde{r}\to 0}\tilde{r}\phi_{1n_{\tilde{r}}}=0 \tag{5-44}$$

$$\phi_{1n}(x,H)=\phi_{0_{\tilde{r}}}(x,H)A_n \tag{5-45}$$

$$A_n \equiv \frac{4}{\pi}\int_0^{\frac{\pi}{2}} g(\theta)\cos n\theta d\theta, (n>0) \tag{5-46}$$

$$A_0 \equiv \frac{2}{\pi}\int_0^{\frac{\pi}{2}} g(\theta)\cos n\theta d\theta \tag{5-47}$$

By Malmuth and Cole [118], the function $g(x)$ which controls the drag and pressure distribution is the only part of the dominant near field that interacts with the dominant outer solution. Since there is no θ dependence in this portion, the only solution of interest is that corresponding to n =0. Thus the effect of the higher harmonics A_n for $n>0$ are negligible to this order. Effectively, the angular dependence is "averaged out". **This is another kind of area rule for the effect of slightly asymmetric wall sections**.

To quantify this effect, the mild transonic case corresponding to large K in (5-43) was considered. To simplify the analysis, the problem is reduced to a harmonic (incompressible) one by scaling out K by an x transformation and noting that the second and third terms in (5-43) are negligible. The x transformation is

$$\tilde{x} = x/\sqrt{K}\,. \tag{5-48}$$

This is equivalent to another procedure that relates the KG to the Prandtl-Glauert (PG) equation from the definition of K in (5-32) and the fact that the appropriate outer variable for subsonic flow is r rather than $\tilde{r}$ in the KG regime. This gives the reduced PG equation

$$\phi_{1nXX} + \frac{1}{r}\left(r\phi_{1nr}\right)_r - \frac{n^2}{r^2}\phi_{1n} = 0. \tag{5-49}$$

where with some redundancy in notation used in a previous section, the transformation

$$X = x/\beta$$

in which

$$\beta \equiv \sqrt{1-M_\infty^2}$$

is used.

The boundary conditions (5-44) and (5-45) are unaffected by the large K approximation. These relations and (5-49) constitute the problem $\mathrm{P1}'$ which can be solved by the exponential Fourier transform pair using the procedure detailed in Malmuth and Cole [118], to give the difference of the non-circular and circular cross section wind tunnel pressures on a body as

$$\Delta C_p \equiv C_p\big|_{\varepsilon\neq 0} - C_p\big|_{\varepsilon=0}, \tag{5-50}$$

where

$$\Delta C_p = \frac{\delta\varepsilon}{\beta\pi^2 h} A_0 \int_0^{\beta^{-1}} A'(\xi)d\xi \int_0^{\infty} \frac{\sin k\left(X-\xi\right)}{I_0^2(kh)}dk. \tag{5-51}$$

To illustrate (5-51), a parabolic arc body of revolution inside a square cross section tunnel is considered.

For this case

$$r_b(x) = \delta x(1-x), 0 \le x \le 1 ,$$

where r_b is the body radius. Accordingly,

$$A = \pi r_b^2 = \pi\delta^2\left(x^2 - 2x^3 + x^4\right) \tag{5-52}$$

and

$$A_0 = \frac{2^{-1/2}}{\left(\sqrt{2}-1\right)\pi}\left\{\log\left(\frac{\tan\frac{3\pi}{8}}{\tan\frac{\pi}{8}}\right) + \frac{\pi}{2}\right\} = 1.81. \tag{5-53}$$

Figure 5.80 shows the effect of increasing Mach number on the normalised correction of the pressures from a circular to a square test section, $\Delta\tilde{C}_p$, where,

$$\Delta\tilde{C}_p \equiv -\frac{\Delta C_p}{\frac{\delta\varepsilon}{\beta\pi^2 h}A_0}, \tag{5-54}$$

when h =1 for a parabolic arc body, *i.e.*, the tunnel average radius is equal to the body length. Note that although the body is in the interval $0 \le x \le 1$, wall asymmetry influences the flow considerably upstream

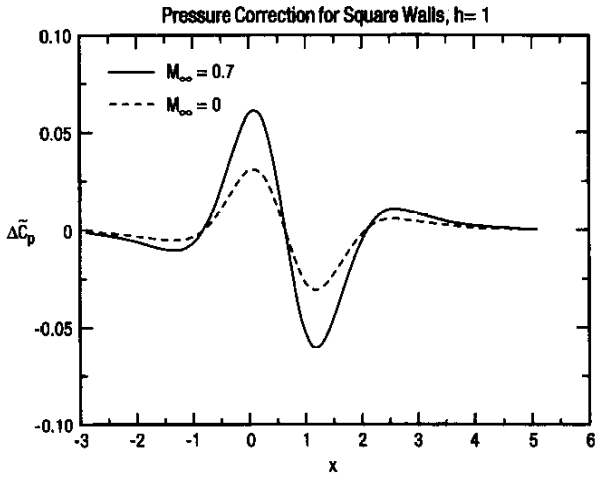

Figure 5-80 : Pressure corrections from circular to square test sections, parabolic body, h = 1

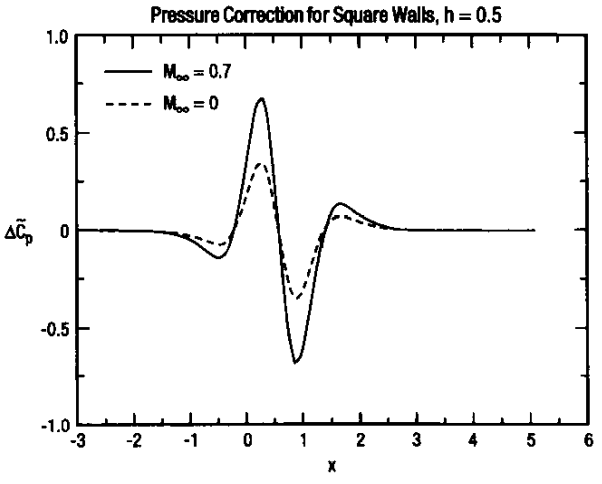

Figure 5-81 : Pressure corrections from circular to square test sections, parabolic body, h = 0,5

of the body nose. Moreover, the largest effects appear at the nose and tail of the body and the correction increases with Mach number as expected. Another observation is the rapid upstream and downstream decay of the effect. This is consistent with the flow ellipticity. Lastly and most important is the smallness of the effect which is in sharp contrast with the results for h =.5 which shows a dramatic ten-fold increase with merely halving the wall height. This effect is brought out in Figure 5.81 and Figure 5.82. for M_∞ =0 and .7 respectively. In accord with expectations, Figure 5.83 shows that compressibility increases the change in pressure associated with wall asymmetry.

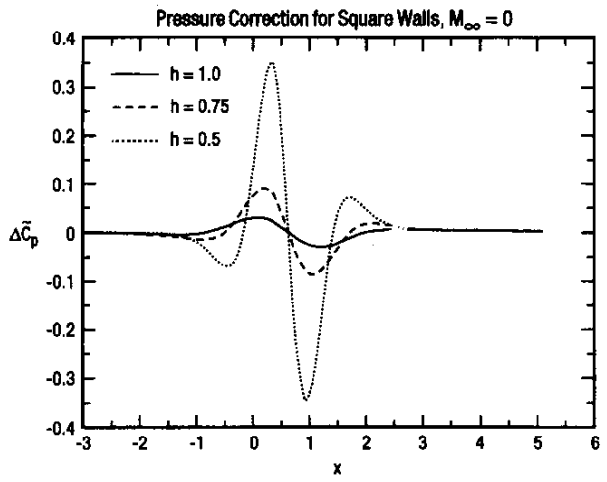

Figure 5-82 : Pressure corrections from circular to square test sections, parabolic body, effect of h for M∞ = 0

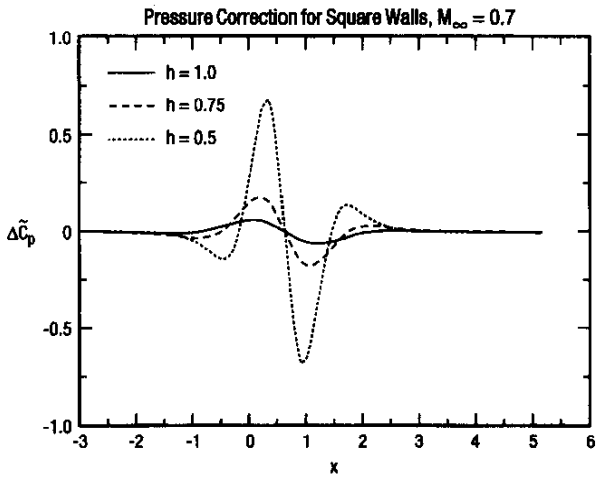

Figure 5-83 : Pressure corrections from circular to square test sections, parabolic body, effect of h for M∞ = 0,7

5.4.11 SUMMARY, CONCLUSIONS AND RECOMMENDATIONS

The CAN methodology described in the previous sections provides a number of unique and useful tools to the wind tunnel test engineer. These are:

1. An area rule for blockage interference for wall heights of the order of the body length.
2. A systematic asymptotic theory for lift interference.
3. Simplified corrections for asymmetric deviations of circular wind tunnel sections.
4. Emerging database for transonic wall interference theories from Russian tests. Items 1 and 2 apply to porous wind tunnels. Item 3 can be readily extended to such sections.

The ultimate impact of this work is to

- Reduce computational intensity of transonic wall interference estimation.
- Help optimise model sizing to maximise test Reynolds number while minimising wall interference.
- Provide a quick means of extrapolating ground tests to free flight.

To enhance the utility of these tools the following further effort is recommended:

- Apply Items 1 and 2 to corrections to drag polars as in Section 5.3.3.5 .
- Extend Item 2 to transonic flow, moderate chords, and thickness
- Extend Item 3 to the moderate K case.
  - Strong evidence exists that the n =0 solution of (5-43) is appropriate to the strongly non-linear transonic case. The argument is similar to that following (5-50).
  - It is envisioned that $\delta'(x)$ "spiky" behaviour of the variational solution near shocks will be the principal modification of the solutions previously discussed for the high subsonic large K case.
  - Validation of the subsonic solutions against the exact eigenfunction and elliptic function Green's functions should be performed.

5.5 ASSESSMENT OF STATE OF THE ART

The previous sections gave a perspective of various aspects of transonic wind tunnel wall interference. Obviously, many topics could not be covered in this brief discussion. Nevertheless, some indication will be made where further improvement is needed. Some key issues in this connection are:

- Wall boundary conditions (wall boundary layer interactions; effects of geometry, viscosity, Reynolds number; acoustics, etc.)
- Identification of non-physical flow conditions (correctable vs. uncorrectable)
- Interaction with support interference
- Fast turn-around wall interference predictions/assessments
- Multibody problems
- Boundary layer transition considerations
- Turbulence modelling-direct simulation
- Transition
- Separation
- Coupling of separation and transition
- Reynolds number scaling to flight
- Unsteady effects

Since these topics strongly interact with each other, no attempt will be made to deal with them separately in this short overview.

In Section 5.2, current wall boundary condition technology was reviewed. In spite of progress involving the pressure pipe method and other boundary-measurement techniques, more work is required to enable accurate non-invasive static pressure measurements in the vicinity of ventilated walls. Detailed experiments which examine viscous interactions within the tunnel close-wall flow field are required for all types of wall geometries, particularly for conditions where flow is into the test section and where large model-induced gradients significantly interact with the wall boundary layers. Relatively minor changes in wall geometry can make significant changes in the close-wall flow field (or boundary condition) and, thereby, induce great changes in the wall-induced interference distribution in the vicinity of the model. Because of this, research directed at tailoring the wall flow via small modifications to wall geometry may enable inexpensive quasi-adaptive techniques for ventilated tunnels, i.e. the correctable-interference tunnel. Reynolds number scaling to flight issues will require transonic tunnels with quiet walls, and studies which examine the acoustic properties of various wall geometries are needed for both assessment of effects on model aerodynamic data and quiet wall/tunnel design. Very little has been done to quantify the upstream and downstream (test section end) effects on the corrections, and this should be addressed.

Computational methods were presented in section 5.3. Section 5.3.2.2.6 shows good progress in our ability to compute transonic wall interference over a complex configuration such as the fully-mated Space Shuttle launch configuration (SSLV). Reynolds-Averaged Navier Stokes (RANS) computational modelling has improved substantially since the last AGARD review. Modern unstructured grid methods as well as parallel computing have made simulation of complex configurations in wind tunnels more practical.

However, in addition to turbulence modelling, issues in computing such a shape are many. At transonic speeds, the interaction of the support structure in the wind tunnel is an artifact not seen in the free flight environment. Simulation of plumes and their interaction with walls and stings can be a source of concern in ground test-to-flight extrapolation. This effect is highly Reynolds number-dependent and solid wall simulation may be unrealistic, even for single plumes, to say nothing of multiple ones such as those from the Solid Rocket Boosters, External Tank and Orbiter. More work is required to deal with the very special questions associated with this topic such as interaction of the wakes and shear layers with each other and the walls.

Similar issues relate to wall corrections for transonic characteristics of HSCT's. Recent internally reported work by Malmuth, Neyland, and Neyland in 1995 [124] for TsAGI T-128 tunnel tests has studied the interaction of nacelle flows with wall interference and transonic wave drag rise simulations.* More effort will be required in dealing with the trade-off of model size needed for proper unit Reynolds number simulation at the expense of large wall corrections, or in the extreme, uncorrectability. For the unsteady ascent trajectory of vehicles such as SSLV and reusable launch vehicles (RLV), the adequacy of the pseudo-steady approximation especially at the maximum q (dynamic pressure) trajectory point needs further attention.

These questions also arise in assessment of wall interference associated with store carriage and separation. Currently, the Captive Trajectory Support System (CTS) is the workhorse of experimental databases for store certification. Complex store configurations such as the F-15, F-16 and F-22 involve multiple interfering bodies such as bombs, missiles, pylons, racks with parent bodies. The CTS method intrinsically assumes pseudo-steady conditions. Effort such as free drops in the wind tunnel is needed to validate this approximation. This becomes particularly important for simulating store separation from weapons-bay cavities. Here, as above, the interaction of the support and wall interference is critical. Also key is the coupling of the shear layer with the body dynamics and the store's steep wave system impinging on the walls. These are complexities that arise in the correlation of wind tunnel results and flight experiments as well as predictions.

Large-scale and CAN mid-range simulations such as those discussed in this chapter should be used to study the various time scales in the weapons-release problem. Unit problems that relate the wind tunnel simulation to the free flight environment should be tackled. They should evaluate sting mounted arrangements and their relationship to unsupported ones in and out of cavities. More work should be done with research configurations rather than complex ones to isolate the basic effects. Physical mechanisms that should be studied are unsteady shock and vortex evolution and convection effects. The data coming from such computational and experimental models could stimulate theoretical development and enhance our understanding of the various processes.

In the previous sections, the issue of correctability was mentioned. At transonic speeds, shock-induced transition plays strongly into this problem. Since a strong Reynolds number dependence is relevant, pre-test assessment of wall interference depends on accurate turbulence models. Although much effort has gone into developing such simulations, much more is required. As computer power increases into the next century, Direct Numerical Simulations (DNS) could provide dramatic new insights. This could flow to improved RANS and mid-range approaches that will improve our capability to make such pre-test assessments economically and rapidly

---

* This wave drag rise is vital in accurately assessing the "transonic pinch point" that affects noise-abatement, operational, payload and fuel considerations impacting HSCT and hypersonic vehicle mission viability and affordability.

In many cases, transitional separations are encountered. Treatment of interaction of separation and transition is a challenge in and out of the wind tunnel. It is so difficult that trips are used to provide a baseline for understanding the flow by making it fully turbulent over the model. However, many flight environments are really transitional and it is necessary to improve our computational simulations by inclusion of suitable stability and transition prediction modules so they can relate to natural transition wind tunnel experiments. Unfortunately, current transition prediction modules are in a very early stage of being able to handle interaction of separation and transition, even in the rudimentary cases of a leading edge separation bubble over a two-dimensional airfoil and flap hinge moment prediction.

Improved techniques will have a strong impact on computational simulations as well as adaptive wall technology and our understanding of the complex flow processes that are needed for control and prediction of transonic wall interference.

5.6 REFERENCES FOR CHAPTER 5

[1] Adams, M.C.; and Sears, W.R. 1953: Slender-Body Theory, Review and Extension. J. Aero. Sci., pp. 85-98.

[2] Adcock, J.B.; and Barnwell, Richard W. 1984: Effect of Boundary Layers on Solid Walls in Three-Dimensional Subsonic Wind Tunnels. AIAA J. vol. 22, no. 3, pp. 365-371.

[3] AGARD 1982: Wall Interference in Wind Tunnels. 50th Fluid Dynamics Panel Specialists' Meeting, London, England, May 19-20, 1982, AGARD-CP-335.

[4] AGARD 1990: Adaptive Wind Tunnel Walls - Technology and Application. Report of the AGARD Fluid Dynamics Panel Working Group 12 Hornung, H.G., Chairman. AGARD-AR-269.

[5] AGARD 1993: Wall Interference, Support Interference, and Flow Field Measurements. 73rd Fluid Dynamics Panel Symposium, Brussels, Belgium, October 4-7, 1993, AGARD-CP-535.

[6] Agrell, Nada 1994: Computational Simulations for Some Tests in Transonic Tunnels. Presented at the 82nd Meeting of the Supersonic Tunnel Association, Wright Laboratory Flight Dynamics Directorate, Wright-Patterson Air Force Base.

[7] Agrell, Nada; Pettersson, Björn; and, Sedin, Yngve C-J. 1986: Numerical Design Parameter Study for Slotted Walls in Transonic Wind Tunnels. Paper No. ICAS-86-1.6.2, presented at the 15th ICAS Congress, London.

[8] Al-Saadi, Jassim A. 1991: Wall Interference Calculation in a Transonic Wind Tunnel With Discrete Slots. Ph.D. Dissertation, North Carolina State Univ.

[9] Al-Saadi, Jassim A. 1993: Wall Interference and Boundary Simulation in a Transonic Wind Tunnel With a Discretely Slotted Test Section. NASA TP 3334.

[10] Al-Saadi, Jassim A.; and, DeJarnette, F.R. 1992: Wall Interference Calculation in a Transonic Test Section Including Simulation of Discrete Slots. AIAA Paper No. 92-0032 presented at 30th Aerospace Sciences Meeting & Exhibit, Reno, NV.

[11] Ashill, P.R. 1983: Effects of Sidewall Boundary Layers on Aerofoils Mounted from Sidewalls of Wind Tunnels - Experimental Evidence and Developments of Theory. RAE TR 83065, August 1983.

[12] Ashill, P.R. 1993: Boundary-Flow Measurement Methods for Wall Interference Assessment and Correction - Classification and Review. Pp. 12-1 to 12-21 in AGARD 1993.

[13] Ashill, P.R.; and Weeks, D.J. 1982: A Method for Determining Interference in Solid Wall Tunnels from Measurements of Static Pressure at the Walls. Paper No. 1 in AGARD 1982.

[14] Ashill, P.R.; Taylor, C.R.; and Simmons, M.J. 1994: Blockage Interference at High Subsonic Speeds in a Solid-Wall Tunnel.

[15] Bailey, F.R. 1971: Numerical Calculation of Transonic Flow About Slender Bodies of Revolution. NASA TN D-6582.

[16] Baldwin, B.S.; and Turner, J.B. 1954: Wall Interference in Wind Tunnels with Slotted and Porous Boundaries at Subsonic Speeds. NACA TN 3176.

[17] Barnwell, R.W. 1974: Transonic Flow About Lifting Wing-Body Combinations. AIAA Paper 74-185.

[18] Barnwell, R.W. 1980: Similarity Rule for Sidewall Boundary-Layer Effect in Two-Dimensional Wind Tunnels. AIAA J. vol 18, no 9 , pp 1149-1151.

[19] Barnwell, R.W.; and Sewall, W.G. 1982: Similarity Rules for Effects of Sidewall Boundary-Layers in Two-Dimensional Wind Tunnels. Paper No. 3 in AGARD 1982.

[20] Barnwell, Richard W. 1976: Improvements in the Slotted-Wall Boundary Condition. Proceedings--AIAA Ninth Aerodynamic Testing Conference, pp. 21-30.

[21] Barnwell, Richard W. 1978: Design and Performance Evaluation of Slotted Walls for Two-Dimensional Wind Tunnels. NASA Technical Memorandum 78648.

[22] Baronti, P.; Ferri, A.; and, Weeks, T. 1973: Analysis of Wall Modifications in a Transonic Wind Tunnel. Advanced Technology Laboratories TR-181.

[23] Benek, J.A.; Steger, J.L.; Dougherty, F.C.; and Buning, P.G. 1986: "Chimera 1986: A Grid-Embedding Technique. AEDC-TR-85-64 AD-A167466. April.

[24] Berndt, Sune B. 1977: Inviscid Theory of Wall Interference in Slotted Test Sections. AIAA J., Vol. 15, No. 9, pp. 1278-1287.

[25] Berndt, Sune B. 1982: Flow Properties of Slotted-Wall Test Sections. AGARD Fluid Dynamics Panel Specialist Meeting on Wall Interference in Wind Tunnels, Paper No. 6.

[26] Berndt, Sune B.; and Sörensen, Hans 1976: Flow Properties of Slotted Walls for Transonic Test Sections. Wind Tunnel Design and Testing Techniques, AGARD-CP-174, pp. 17-1—17-10.

[27] Bhat, Maharaj Krishen 1988: On Transonic Flow Over Segmented Slotted Wind Tunnel Wall with Mass Transfer. Ph.D. Diss., The University of Tennessee.

[28] Binion, T.W., Jr. 1975: An Experimental Study of Several Wind Tunnel Wall Configurations Using Two V/STOL Model Configurations. AEDC TR-75-36.

[29] Blynskaya, A.A.; and Lifshitz, Y.B. 1981: Transonic Flows Around an Airfoil in Wind Tunnels. Fluid Dynamics, Vol. 15, pp. 711-718.

[30] Boppe, C.W. 1987: Aerodynamic Analysis for Aircraft with Nacelles, Pylons, and Winglets at Transonic Speeds. NASA CR-4066, April.

[31] Buning, P.G.; Chan, W.M.; Renze, K.J.; Sondak, D.; Chiu, I.T.; and Slotnick, J.P. 1991: OVERFLOW/F3D User's Manual, Version 1.6p, NASA Ames Research Center, Moffett Field, CA, December.

[32] Catherall, D. 1975: The Computation of Transonic Flows Past Aerofoils in Solid, Porous, or Slotted Wind Tunnels. Paper 19, AGARD CP 174.

[33] Chan, Y.Y. 1982: Wall Boundary-Layer Effects in Transonic Wind Tunnels. AGARD-CP-335, May, pp. 7-1 to 7-15.

[34] Chan, Y.Y., 1980. A Singular Perturbation Analysis of Two-Dimensional Wind Tunnel Interferences. ZAMP, 31 pp. 605-619.

[35] Chen, C.F.; and Mears, J.W. 1957: Experimental and Theoretical Study of Mean Boundary Conditions at Perforated and Longitudinally Slotted Wind Tunnel Walls. AEDC TR-57-20.

[36] Chew, W.L. 1955: Cross-Flow Calibration at Transonic Speeds of Fourteen Perforated Plates with Round Holes and Airflow Parallel to the Plates. AEDC-TR-54-65, July.

[37] Cole, J.D.; and Cook, L.P. 1986: Transonic Aerodynamics. North-Holland, New York.

[38] Cole, J.D.; and Malmuth, N.D., 1989: Shock Wave Location on a Slender Transonic Body of Revolution. Mechanics Research Communications, Vol. 10, no. 6, November-December, pp. 353-335

[39] Cole, J.D.; Malmuth, N.D.; and Ziegler, F. 1982: An Asymptotic Theory of Solid Tunnel Wall Interference. AIAA Paper 82-0933, AIAA/ASME 3rd Joint Thermophysics, Fluids, Plasma, and Heat Transfer Conference, St. Louis, Missouri, June 7-11.

[40] Cook, L.P.; and Cole, J.D. 1978: Lifting Line Theory for Transonic Flow. SIAM J. Appl. Math., Vol. 35, no. 2, September , pp. 209-228.

[41] Crites, R. C. 1987: Transonic Wind Tunnel Boundary Interference - A Correction Method. AGARD CP-429, Oct.., pp. 15-1 to 15-16.

[42] Crites, R.; and Rueger, M. 1992: Modelling the Ventilated Wind Tunnel Wall. AIAA Paper No. 92-0035, presented at the AIAA 30th Aerospace Sciences Meeting, Reno, NV, January 6-9.

[43] Crites, R.; and, Steinle, Frank W., Jr. 1995: Wall Interference Reduction Methods for Subsonic Wind Tunnels. AIAA Paper No 95-0107 presented at 33rd Aerospace Sciences Meeting and Exhibit, Reno, NV.

[44] Daugherty, N.S., Jr.; and, Steinle, Frank W., Jr. 1974: Transition Reynolds Number Comparisons in Several Major Transonic Tunnels. AIAA Paper No. 74-627.

[45] Daugherty, N.S., Jr.; Anderson, C.S.; and, Parker, R.L., Jr. 1988: An Experimental Investigation of Techniques to Suppress Edge Tones from Perforated Wind Tunnel Walls. AEDC-TR-75-88.

[46] Davis, Don D., Jr.; and Moore, Dewey 1953: Analytical Studies of Blockage- and Lift-Interference Corrections for Slotted Tunnels Obtained by the Substitution of an Equivalent Homogeneous Boundary for the Discrete Slots. NACA RM-L53-E07b.

[47] Donegan, T.L.; Benek, J. A.; and Erickson, J. C., Jr. 1987: Calculation of Transonic Wall Interference. AIAA Paper No. 87-1432, presented at the AIAA 19th Fluid Dynamics, Plasma Dynamics, and Laser Conference, Honolulu, HI, June 8-10.

[48] Doria, M.L.; and South, J.C., Jr. 1982: Transonic Potential Flow and Coordinate Generation for Bodies in a Wind Tunnel. AIAA Paper 82-0223.

[49] Elsenaar, A., editor 1983: Two-Dimensional Transonic Testing Methods - Final Report. NLR-TR-83086, GARTEUR/TP-011 work completed July, 1981.

[50] Emmons, H. W. 1948: Flow of a Compressible Fluid Past a Symmetrical Airfoil in a Wind Tunnel and in Free Air. NACA TN 1746.

[51] Erickson, J.C. Jr. 1990: Adaptive Wind Tunnel Walls - Compendium of Final Report - AGARD FDP Working Group 12. AIAA Paper No. 90-1405, presented at AIAA 16th Aerodynamic Ground Testing Conference, Seattle, WA, June 18-20.

[52] Erickson, J.C., Jr.; and Homicz, G. F. 1982: Numerical Simulation of a Segmented Plenum, Perforated, Adaptive-Wall Wind Tunnel. AIAA J., Vol. 20, No. 5, May, pp. 612-623.

[53] Everhart, Joel L. 1987: Theoretical and Experimental Analysis of the Slotted-Wall Flow Field in a Transonic Wind Tunnel. SAE Tech. Paper Ser. 871757.

[54] Everhart, Joel L.; and Barnwell, Richard W. 1978: A Parametric Experimental Study of the Interference Effects and the Boundary-Condition Coefficient Slotted Wind-Tunnel Walls. AIAA Paper No 78-805 presented at the AIAA 10th Aerodynamic Testing Conference, San Diego, CA.

[55] Everhart, Joel L.; and Bobbitt, Percy J. 1994: Experimental Studies of Transonic Flow Field Near a Longitudinally Slotted Wind Tunnel Wall. NASA TP 3392.

[56] Everhart, Joel L.; and Goradia, Suresh H. 1991: Mass Flux Similarity for Slotted Transonic-Wind-Tunnel Walls. NASA TM 4281.

[57] Everhart, Joel L.; Igoe, William B.; and Flechner, Stuart G. 1991: Slotted-Wall Flow-Field Measurements in a Transonic Wind Tunnel. NASA TM-4280.

[58] Everhart, Joel Lee 1988: Theoretical and Experimental Studies of the Transonic Flow Field and Associated Boundary Conditions Near a Longitudinally-Slotted Wind-Tunnel Wall. D.Sc. Diss., The George Washington Univ. Available as NASA TM-103381.

[59] Ferri, A., and Baronti, P. 1973: A Method for Transonic Wind-Tunnel Corrections. AIAA J., Vol. 11, No. 1, pp. 63-66.

[60] Foster, Jean M.; and Adcock, Jerry B. 1996: User's Guide for the National Transonic Facility Research Data System. NASA Technical Memorandum 110242.

[61] Freestone, M.M.; and, Henington, P. 1981: Incorporation of Viscous Effects of Perforated Wind Tunnel Walls in Two-Dimensional Flow Calculations. City University (London) Res. Memo Aero 81/1.

[62] Freestone, M.M.; and, Mohan, S.R. 1993: Interference Determination for Wind Tunnels with Slotted Walls. Paper No. 16 presented at AGARD Fluid Dynamics Panel Symposium on "Wall Interference, Support Interference, and Flow Field Measurements," AGARD CP 535, pp. 19-1 to 19-12, Brussels, Belgium.

[63] Freestone, M.M.; Gascoigne, A.; and, Lock, R.C. 1984: Determination of Interference in a Transonic Wind Tunnel having Perforated Liners. Paper presented at Euromech Colloquium 187, Goettingen, West Germany.

[64] Freestone, M.M.; Mohan, S.R.; and, Lock, R.C. 1992: Interference Corrections in Wind Tunnels with Slotted Walls. Paper 16, Proceedings of the Royal Aeronautical Society conference on "Wind Tunnels and Wind Tunnel Test Techniques."

[65] Gadd, G.E., 1960. The Possibility of Normal Shock Waves On a Body With Convex Surfaces in Inviscid Transonic Flow," Zeit. Ang. Math. and Phys., 11 pp. 51-55.

[66] Gaffney, R.L., Jr.; Salas, M.D.; and Hassan, H.A. 1985: Assessment of Wind Tunnel Corrections for Multielement Airfoils at Transonic Speeds. 3rd Symposium on Numerical and Physical Aspects of Aerodynamic Flows, Jan. 20-24, Long Beach, CA.

[67] Garner, H.C.; Rogers, E.W.E.; Acum, W.E.A.; and Maskell, E.E. 1966: Subsonic Wind Tunnel Wall Corrections. AGARDograph 109.

[68] Garriz, J. A.; and Haigler, K. J. 1992: User Guide for WIACX: A Transonic Wind-Tunnel Wall Interference Assessment and Correction Procedure for the NTF. NASA TM-104168.

[69] Garriz, J. A.; Newman, P. A.; Vatsa, V. N.; Haigler, K. J.; and Burdges, K. P. 1990: Evaluation of Transonic Wall Interference Assessment and Corrections for Semi-Span Wing Data. AIAA Paper 90-1433.

[70] Gentry, Garl L.; Igoe, William B.; and Fuller, Dennis E. 1981: Description of 0.186-Scale Model of High-Speed Duct of National Transonic Facility. NASA TM 81949.

[71] Goethert, Bernhard H. 1961: Transonic Wind Tunnel Testing. AGARDograph No. 49 Pergamon Press.

[72] Goodman, T.R., 1951. The Porous Wind Tunnel, Part IV, Subsonic Interference Problems in a Circular Tunnel," Cornell Aeronautical Laboratory Report AD-706-A-2.

[73] Goodyer, M. J. 1975: The Self-Streamlining Wind Tunnel. NASA TM X-72699.

[74] Green, L. L.; and Mineck, R. E. 1991: Wall Interference Assessment/Correction for Transonic Airfoil Data. J. of Aircraft, Vol. 28, No. 11, pp. 774–780, also AIAA 90-1406.

[75] Green, L. L.; and Newman, P. A. 1987: Transonic Wall Interference Assessment and Corrections for Airfoil Data from the 0.3-m TCT Adaptive Wall Test Section. AIAA Paper 87-1431.

[76] Green, L. L.; and Newman, P. A. 1991: Wall Interference Assessment and Corrections for Transonic NACA 0012 Airfoil Data from Various Windtunnels. NASA TP 3070.

[77] Green, L.; Zhang, Q.; Garriz, J.; Wang, S.; Vatsa, V.; Haigler, K.; and Newman, P. 1991: NASA/CAE Wind Tunnel Interference Cooperative Program-- Status and Sample Results, January 1991. ICAW 1991 Paper - W1, in He (1991).

[78] Gumbert, C. R. 1985: User Manual for 0.3-m TCT Wall-Interference Assessment/Correction Procedure: 8- by 24-Inch Airfoil Test Section. NASA TM–87582.

[79] Gumbert, C. R.; and Newman, P. A. 1984: Validation of a Wall Interference Assessment/Correction Procedure for Airfoil Tests in the Langley 0.3–m Transonic Cryogenic Tunnel. AIAA Paper 84-2151.

[80] Gumbert, C. R.; Newman, P. A.; Kemp, W. B., Jr.; and Adcock, J. B. 1984: Adaptation of a Four-Wall Interference Assessment/Correction Procedure for Airfoil Tests in the 0.3-m TCT, pp. 393–414 in Newman and Barnwell (1984).

[81] Gumbert, C.R.; Green, L.L.; and Newman, P.A. 1989: Nonlinear Transonic Wall- Interference Assessment / Correction (WIAC) Procedures and Application to CAST 10 Airfoil Results from the 0.3-m TCT 8- x 24-inch Slotted Wall Test Section. NASA CP 3052, pp 9-35.

[82] Harris, C. D.; Harvey, W. D.; Brooks, C. W., Jr. 1988: The NASA Langley Laminar-Flow Control Experiment on a Swept, Supercritical Airfoil. NASA TP 2809.

[83] He, J.J., editor 1991: Proceedings of International Conference on Adaptive Wall Wind Tunnel Research and Wall Interference Correction ICAW. June 10-14,1991, Chinese Aeronautical and Astronautics Establishment, Northwestern Polytechnical University, Xian, China.

[84] Hinson, B.L.; and Burdges, K.P., 1980: Acquisition and Application of Transonic Wing and Far Field Test Data for Three-Dimensional Computational Method Evaluation," AFOSR Report 80-0421.

[85] Hornung, H.; and Stanewsky, E., editors 1984: Adaptive Wall Wind Tunnels and Wall Interference Correction Methods. Oct. 15-17, 1984, DFVLR-IB-222-84-A-37.

[86] Hornung, H.G., editor 1990: Adaptive Wind Tunnel Walls - Technology and Applications. Report of the Fluid Dynamics Panel Working Group 12, AGARD-AR-269.

[87] Inger, G.R. 1967: Laminar Boundary-Layer Solutions with Strong Blowing. AIAA J., 5 9, Sept., pp. 1677-1679.

[88] Jacocks, J.L. 1977: Aerodynamic Characteristics of Perforated Walls for Transonic Wind Tunnels. AEDC-TR-77-61.

[89] Jones, R.T., 1946: Properties of Low-Aspect Ratio Pointed Wings at Speeds Below and Above the Speed of Sound. NACA Report 835.

[90] Kacprzynski, J.J. 1975: Transonic Flow Field Past 2-D Airfoils Between Porous Wind Tunnel Walls With Nonlinear Characteristics. AIAA Paper 75-81.

[91] Karlsson, K.R.; and Sedin, Y.C.-J. 1979: Axisymmetric Calculations of Transonic Wind Tunnel Interference in Slotted Test Sections. AIAA J. Vol. 17, No. 8, pp. 917-919.

[92] Karlsson, K.R.; and Sedin, Y.C.-J. 1980: Numerical Design and Analysis of Optimal Slot Shapes for Transonic Test Sections - Axisymmetric Flows. AIAA Paper 80-0155, Jan.

[93] Keller, James D. 1972: Numerical Calculation of Boundary-Induced Interference in Slotted or Perforated Wind Tunnels Including Viscous Effects in Slots. NASA TN D-6871.

[94] Keller, James D.; and Wright, Ray, H. 1971: A Numerical Method of Calculating the Boundary-Induced Interference in Slotted or Perforated Wind Tunnels of Rectangular Cross Section. NASA TR R-379.

[95] Kemp W.B., Jr 190: User's Guide to PANCOR: A Panel Method Program for Interference Assessment in Slotted-Wall Wind Tunnels. NASA CR-187479.

[96] Kemp W.B., Jr 1986a: Computer Simulation of a Wind Tunnel Test Section with Discrete Finite-Length Wall Slots. NASA CR-3948.

[97] Kemp W.B., Jr 1986b: User's Guide to STIPPAN: A Panel Method Program for Slotted Tunnel Interference Prediction. NASA CR-178003.

[98] Kemp W.B., Jr 1988: A Panel Method Procedure for Interference Assessment in Slotted-Wall Wind Tunnels. AIAA Paper 88-2537.

[99] Kemp, W. B. 1978: Transonic Assessment of Two-Dimensional Wind Tunnel Wall Interference Using Measured Wall Pressures. NASA CP–2045, pp. 473–486.

[100] Kemp, W. B., Jr. 1980: TWINTAN: A Program for Transonic Wall Interference Assessment in Two-Dimensional Wind Tunnels. NASA TM–81819.

[101] Kemp, W. B., Jr. 1984: TWINTN4: A Program for Transonic Four-Wall Interference Assessment in Two-Dimensional Wind Tunnels. NASA CR–3777.

[102] Kemp, W. B., Jr.; and Adcock, J. B. 1983: Combined Four-Wall Interference Assessment in Two-Dimensional Airfoil Tests. AIAA J., Vol. 21, pp. 1353–1359, also AIAA Paper 82-0586.

[103] Kemp, W.B., Jr 1985: A Slotted Test Section Numerical Model for Interference Assessment. J. Aircraft, Vol. 22, No. 3, pp. 216-222 also AIAA Paper 84-0627

[104] Kemp, W.B., Jr. 1976: Toward the Correctable-Interference Transonic Wind Tunnel. Proceedings, AIAA Ninth Aerodynamic Testing Conference, June, pp. 31-38.

[105] Kevorkian, J.; and Cole, J., 1980: Perturbation Methods in Applied Mathematics. Springer-Verlag, New York.

[106] Kordulla, Wilhelm (Ed.) 1988: Numerical Simulation of the Transonic DFVLR-F5 Wing Experiment. Volume 22, Notes on Numerical Fluid Mechanics, Vieweg Verlag, Braunschweig.

[107] Kraft, E.M. 1983: An Overview of Approaches and Issues for Wall Interference Assessment/Correction. NASA CP-2319, Jan.

[108] Kraft, E.M.; and, Lo, C.F. 1973: A General Solution for Lift Interference in Rectangular Ventilated Wind Tunnels. AIAA Paper No. 73-209 presented at the 11th Aerospace Sciences Meeting, Washington, DC.

[109] Kraft, E.M.; Ritter, A.; and Laster, M. 1986: Advances at AEDC in Treating Transonic Wind Tunnel Wall Interference. ICAS Paper 86-1.6.1.

[110] Kraft, E.M.; Ritter, A.; and Laster, M.L.: Advances at AEDC in Treating Transonic Wind Tunnel Wall Interference. Proceedings, 15th Congress of the International Council of the Aeronautical Sciences, London, UK, September 1986, pp. 748-769.

[111] Kuenstner, Rudi; Deutenbach, Klaus-Rainer; and, Vagt Jorg-Dieter 1992: Measurement of Reference Dynamic Pressure in Open-Jet Automotive Wind Tunnels. SAE Paper 920233.

[112] Ladson, Charles L. 1973: Description and Calibration of the Langley 6- by 19-Inch Transonic Tunnel. NASA TN D-7182.

[113] Laster, M. L., editor 1988: Boundary Layer Simulation and Control in Wind Tunnels. Report of the Fluid Dynamics Panel Working Group 09, AGARD-AR-224.

[114] Lee, K.D. 1980: Numerical Simulation of the Wind Tunnel Environment by a Panel Method. AIAA Paper 80-0419.

[115] Lifshitz, Y.B.; and Fonarev, A.S., 1978: Effect of Flow Boundaries on Parameters of Transonic Flows Around Bodies of Revolution. Fluid Dynamics, Vol. 13, pp. 393-399.

[116] Lockman, William K.; and Seegmiller, H. Lee 1983: Experimental Investigation of the Subcritical and Supercritical Flow About a Swept Semispan Wing. NASA TM 84367.

[117] Lynch, F.T.; Crites, R.C.; and Spaid, F.W. 1993: The Crucial Role of Wall Interference, Support Interference, and Flow Field Measurements in the Development of Advanced Aircraft Configurations. pp. 1-1 to 1-38 in AGARD CP 535.

[118] Malmuth, N.; and Cole, J. 1996: Asymptotic Theory of Slender Configurations in and Out of Wind Tunnels. AIAA Paper 96-2119 at the AIAA Theoretical Fluid Dynamics Meeting, June 17-20, New Orleans, LA.

[119] Malmuth, N.D. 1987: An Asymptotic Theory of Wind Tunnel Wall Interference on Subsonic Slender Bodies. J. Fluid Mechanics, Vol. 177, 1987, pp. 19-35.

[120] Malmuth, N.D. 1993: Some Applications of Combined Asymptotics and Numerics in Fluid Dynamics and Aerodynamics. Chapter in Frontiers in Applied Mathematics SIAM. And Numerical Methods for Partial Differential Equations with Critical Parameters, AGARD. Kluwer Press, H.G. Kaper and M. Garbey, ed., Dordrecht, Holland, pp. 53-79.

[121] Malmuth, N.D., 1991a: Asymptotic Methods for Prediction of Transonic Wind Tunnel Wall Interference. International Conference on Adaptive Wall Wind Tunnel Research and Wall Interference Correction, Xian, Shaanxi, China, June 10-14.

[122] Malmuth, N.D.; and Cole, J.D. 1984. Study of Asymptotic Theory of Transonic Wind Tunnel Interference. Final Report for Period May 30, 1982, through August 30, 1983, Contract No. F40600-82-C-0005, Arnold Engineering Development Center/DOS Report AEDC-TR-84-8, Tullahoma, Tennessee.

[123] Malmuth, N.D.; Jafroudi, H.; Wu, C.; Mclachlan, R.; and Cole, J. 1993: Asymptotic Methods Applied to Transonic Wall Interference. AIAA J. 31 5, pp. 911-918.

[124] Malmuth, N.D.; Neyland, V.M.; and Neyland, V. Ya. 1995: Wall Interference Over Small and Large Aspect Ratio Wings in Wind Tunnels. Second Pacific International Meeting in Aerospace Technology PICAST2-AAC6, in proceedings, Melbourne, Australia.

[125] Malmuth, N.D.; Wu C.C.; Jafroudi, H.; Mclachlan, R.; Cole, J.D.; and Sahu, R., 1991b: Asymptotic Theory of Wind Tunnel Wall Interference. AEDC Final Report for Contract F40600-84-C-0010, AEDC-TR-91-24.

[126] Martin, F.W., Jr.; Sickles, W. L.; and Stanley, S. A. 1993: Transonic Wind Tunnel Wall Interference Analysis for the Space Shuttle Launch Vehicle. AIAA Paper No. 93-0420, presented at the AIAA 31st Aerospace Sciences .

[127] Matyk, Gerald E.; and, Kobayashi, Yasunori 1977: An Experimental Investigation of Boundary Layer and Crossflow Characteristics of the Ames 2- by 2-Foot and 11- by 11-Foot Transonic Wind-Tunnel Walls. NASA TM 73257.

[128] Mercer, J. E.; Geller, E.W.; Johnson, M.L.; and Jameson, A. 1980: A Computer Code to Model Swept Wings in an Adaptive Wall Transonic Wind Tunnel. AIAA Paper 80-0156.

[129] Mercer, J.E.; and Murman, E.M. 1980: Application of Transonic Potential Calculations to Aircraft and Wind Tunnel Configurations. Presented at AGARD Fluid Dynamics Panel Symposium on Subsonic/Transonic Configuration Aerodynamics. AGARD-CP-285, May 5-7.

[130] Milholen, W.E.; and Chokani, N. 1992: Numerical Modelling of Transonic Juncture Flow. AIAA Paper 92-4036.

[131] Mohan, S.R.; and, Freestone, M.M. 1994: Interference Determination for Three-Dimensional Flows in Slotted-Liner Wind Tunnels. ICAS paper no. 94-3.3.1 presented at the 19th ICAS Congress, Anaheim, CA.

[132] Mohan, S.R.; Lock, R.C.; and, Freestone, M.M. 1991: Experimental and Theoretical Investigations of Wall Interference in Slotted Test Sections. Proceedings—International Conference on Adaptive Wall Wind Tunnel Research and Wall Interference Correction, Xian, People's Republic of China, pp. W10-1 to W10-13.

[133] Mokry, M., Chan, Y.Y. and Jones, D.V. 1983: Two-Dimensional Wind Tunnel Wall Interference. AGARDograph 281, edited by L.H. Ohman, Nat. Aeronautical Establishment, Nat. Res. Council, Canada, November.

[134] Murman, E.M.; Bailey, F.R.; and Johnson, M.L. 1975: TSFOIL - A Computer Code for Two-Dimensional Transonic Calculations, Including Wind-Tunnel Wall Effects and Wave-Drag Evaluation. NASA SP-347, Part II, pp. 769-788.

[135] Murman, M. 1972: Computational of Wall Effects in Ventilated Transonic Wind Tunnels. AIAA Paper 72-1007.

[136] Murman, M.; and Cole, J. D. 1971: Calculation of Plane Steady Transonic Flows. AIAA J., vol. 9, no. 1, pp. 114-121.

[137] Murthy, A.V. 1986: Effect of Aspect Ratio on Sidewall Boundary Layer Influence in Two-Dimensional Airfoil Testing. NASA CR-4088.

[138] Newman P.A.; Mineck, R.E.; Barnwell, R.W.; and Kemp, W.B., Jr. 1986: Wind Tunnel Wall Interference. Langley Symposium on Aerodynamics, Vol. I, NASA CP-2397, pp. 225-260.

[139] Newman, P.A.; and Barnwell, R.W., editors 1984: Wind Tunnel Wall Interference Assessment/Correction - 1983. NASA Langley Research Center, Jan. 25-26, 1983, NASA CP-2319.

[140] Newman, P.A.; and Klunker, E.B. 1975: Numerical Modelling of Tunnel-Wall and Body-Shape Effects on Transonic Flow over Finite Lifting Wings. NASA SP-347, Part II, pp. 1189-1212.

[141] Newman, P.A.; Anderson, E.C.; Peterson, J.B., Jr. 1984: Aerodynamic Design of the Contoured Wind-Tunnel Liner for the NASA Supercritical Laminar-Flow Control, Swept-Wing Experiment. NASA TP 2335.

[142] Newman, P.A.; Kemp, W.B., Jr; and Garriz, J.A. 1988: Emerging Technology for Transonic Wind-Tunnel Wall Interference Assessment and Corrections. SAE Technical Paper No. 881454.

[143] Newman, P.A.; Kemp, W.B.; and Garriz, J.A. 1989: Wall Interference Assessment and Corrections. NASA CP-3020, Vol. 1, Part 2, pp. 817-851.

[144] Neyland, V.M.; and Neyland V. Ya. 1994: Special Features of Transonic Flows Over Models RI-1 and RI-2 in a Wind Tunnel and Infinite Flow. Final Report for Rockwell Science Center, Contract B4563029.

[145] Obayashi, S.; and Kuwahara, K. 1987: Navier-Stokes Simulation of Side Wall Effect of Two-Dimensional Transonic Wind Tunnel. AIAA Paper 87-37.

[146] Osborne, J. 1973: A Selection of Measured Transonic Flow Pressure Distributions for the NACA 0012 Aerofoil: Provisional Data From Our NPL Transonic Tunnel. Received at the NASA Langley Library, Aug. 29.

[147] Oswatitsch, K.; and Kuene, F. 1955: Ein Aquivalensatz fur Nichangestellte Fluge Kleiner Spannweite in Schallnaher Stromung. Zietschrift fur Flugwissenshaften, Vol. 3, No. 2, S.Ê29-46.

[148] Pearcy, H.H.; Sinnott, C.S.; and, Osborne, J. 1959: Some Effects of Wind Tunnel Interference Observed in Tests on Two-Dimensional Aerofoils at High Subsonic And Transonic Speeds. AGARD Rep. 296.

[149] Phillips, Pamela S.; and Waggoner, Edgar G. 1988: A Transonic Wind Tunnel Wall Interference Prediction Code. AIAA Paper 88-2538 presented at the 6th Applied Aerodynamics Conference, Williamsburg, VA.

[150] Phillips, Pamela S.; and Waggoner, Edgar G. 1990: Transonic Wind-Tunnel Wall Interference Prediction Code. AIAA J. Aircraft, Vol. 27, No. 11, pp. 915-916.

[151] Pindzola, M.; and, Lo, C.F. 1969: Boundary Interference at Subsonic Speeds in Wind Tunnels with Ventilated Walls. AEDC TR-69-47.

[152] Pope, A. 1954: Wind-Tunnel Testing. Wiley & Sons, pp. 268-344.

[153] Radespiel, R. 1989: Calculation of Wind Tunnel Sidewall Interference Using a Three Dimensional Multigrid Navier-Stokes Code. AIAA Paper 89-1790.

[154] Ramaswamy, M.A.; and, Cornette, E.S. 1982: Supersonic Flow Development in Slotted Wind Tunnels. AIAA J., Vol. 20, No. 6, pp. 805-811.

[155] Rizk, M. H. 1986: Improvements in Code TUNCOR for Calculating Wall Interference Corrections in the Transonic Regime. AEDC–TR-86–6.

[156] Rizk, M. H.; and Smithmeyer, M. G. 1982: Wind Tunnel Wall Interference Corrections for Three-Dimensional Flows. J. of Aircraft, Vol. 19, pp. 465–472.

[157] Rizk, M. H.; Hafez, M.; Murman, E. M.; and Lovell, D. 1982: Transonic Wind Tunnel Wall Interference Corrections for Three-Dimensional Models. AIAA Paper 82–0588.

[158] Rizk, M. H.; Smithmeyer, M. G.; and Murman, E. M. 1984: Wind Tunnel Wall Interference Corrections for Aircraft Models, pp. 301–322 in Newman & Barnwell (1984).

[159] Rizk, M.H.; and Murman, E.M. 1984: Wind Tunnel Wall Interference Corrections for Aircraft Models in the Transonic Regime. AIAA J. of Aircraft, Vol. 21, No. 1, Jan., pp. 54-61

[160] Rueger, M.; and Crites, R. 1992: Wind Tunnel Boundary Interference Prediction and Correction. AIAA 92-0036.

[161] Rueger, M.L.; Crites, R.C.; Weirich, R.F.; Creasman, F.; Agarwal, R.K.; and Deese, J.E. 1993: Transonic Wind Tunnel Boundary Interference Correction. Wall Interference, Support Interference and Flow Field Measurements, AGARD CP-535, pp. 21-1 to 21-14.

[162] Sears, W. R. 1974: Self Correcting Wind Tunnels. The Aeronautical Journal, Vol. 78, No. 758/759, pp. 80-89.

[163] Sedin, Y.C.-J.; Agrell, N.; and, Zhang, N. 1985: Computation of Transonic Wall-Interference in Slotted-Wall Test Sections of Wind Tunnels. Paper presented at the International Symposium on Computational Fluid Dynamics Tokyo, Japan.

[164] Sedin, Y.C.-J.; and, Karlsson, K.R. 1982: Some Theoretical Wall-Interference Calculations in Slotted Transonic Test-Sections, Three-Dimensional Flows. Proceedings of the 13th Congress of the International Council of the Aeronautical Sciences/AIAA Aircraft Systems and Technology Conference. ICAS Paper No. 82-6.3.2.

[165] Sedin, Y.C.-J.; and, Karlsson, K.R. 1986: Computed and Measured Wall Interference in a Slotted Transonic Test Section. AIAA J., Vol. 24, No. 3, pp. 444-450.

[166] Sewall, W.G. 1982: The Effects of Sidewall Boundary Layer in Two-Dimensional Subsonic and Transonic Wind Tunnels. AIAA J. vol 20, no 9, pp 1253-1256.

[167] Sickles, W.L.; and Erickson, J.C., Jr. 1988: Evaluation of Wall Interference Assessment and Correction Techniques. AEDC-TR-87-45 AD-A195873, June.

[168] Sickles, W.L.; and Erickson, J.C., Jr. 1990: Wall Interference Correction for Three-Dimensional Transonic Flows. AIAA Paper No. 90-1408, presented at the AIAA 16th Aerodynamics Ground Testing Conference, Seattle, WA, June 18-20.

[169] Sickles, W.L.; and Sinclair, D.W. 1998: Transonic Wind Tunnel Data Correlation on the Transonic Technology Wing Demonstrator TST in AEDC Tunnel 4T, 16T and the NASA National Transonic Facility NTF. To be published as an AEDC technical report.

[170] Sickles, W.L.; and Steinle, Frank W., Jr. 1996: NWTC Slotted Wall Design Effort: Computational Task. Letter report dated May 21 to National Wind Tunnel Program Office Distribution, NASA/LeRC.

[171] Small, R.D. 1978: Studies in Transonic Flow VI, Calculation of a Transonic Lifting Line Theory. UCLA Report UCLA-ENG-7836,

[172] South, J.C., Jr.; and Keller, J.D. 1975: Axisymmetric Transonic Flow Including Wind-Tunnel Wall Effects. NASA SP-347, Part II, pp. 1233-1268.

[173] Stanewsky, E. and Thibert, J.A. 1979; Airfoil SKF 1.1 with Maneuver Flap. AGARD Report No. AR-138, Experimental Database for Computer Program Assessment. May.

[174] Steinle, F. W. Jr. 1991: Unpublished Work, Feb..

[175] Steinle, Frank W., Jr. 1996: Personal communication.

[176] Steinle, Frank W., Jr.; and Pejack, Edwin R. 1980: Toward an Improved Transonic Wind-Tunnel-Wall Geometry — A Numerical Study. AIAA Paper 80-0442 presented at the 11th Aerodynamic Testing Conference, Colorado Springs, Co.

[177] Swanson, R. C.; Radespiel, R.; and McCormick, V.E. 1989: Comparison of Two- and Three-Dimensional Navier-Stokes Solutions With NASA Experimental Data for CAST 10 Airfoil. NASA CP-3052, pp. 238-258.

[178] Tuttle, M.H.; and Cole, K.L. 1988: Wind Tunnel Wall Interference Jan. 1980-May 1988 — A Selected, Annotated Bibliography. NASA TM-4061.

[179] Vandromme, D.; and Haminh, H. 1988: Turbulence Modelling for Compressible Flows, pp 139-158 in Kordulla (1988).

[180] Vatsa, V.N.; and Wedan, B. W. 1988: Navier-Stokes Solutions for Transonic Flow over a Wing Mounted in a Tunnel. AIAA Paper 88-1002.

[181] Wang, K.C. 1968: A New Approach to Not-So-Slender-Wing Theory. Studies in Applied Math, Vol. 4, pp. 391-406.

[182] Whitfield, D.L. 1976: Analytical, Numerical, and Experimental Results on Turbulent Boundary Layers. AEDC-TR-76-62 AD-A027588, July.

[183] Whoric, J.M.; and Hobbs, R.W. 1987: Hierarchy of Uncertainty Sources in Transonic Wind Tunnel Testing. AGARD-CP-429, September-October.

[184] Wilcox, D.C. 1993: Turbulence Modelling for CFD. DCW Industries, Inc., La Canada, CA

[185] Wood, W.W. 1964: Tunnel Interference from Slotted Walls. The Quarterly Journal of Mechanics and Applied Mathematics, Vol. 17, pp. 125-140.

[186] Wu, C.C. 1989: Shock wave location on slender bodies," unpublished E-mail communication to N. Malmuth.

[187] Wu, J.M.; Collins, F.G.; and, Bhat, M.K. 1982: Three-Dimensional Flow Studies on a Slotted Transonic Wind Tunnel Wall. AIAA Paper 82-0230 presented at 20th Aerospace Sciences Meeting, Orlando, Fl.